Functional Maturation of Sensory Coding in Developing Mouse Barrel Cortex

Dissertation

zur

Erlangung der naturwissenschaftlichen Doktorwürde
(Dr. sc. nat.)

vorgelegt der

Mathematisch-naturwissenschaftlichen Fakultät

der

Universität Zürich

von

Alexander-Leopold Berthold van der Bourg

von/aus

Chur-Tamins, GR

Promotionskomitee

Prof. Dr. Fritjof Helmchen (Vorsitz)
Prof. Dr. Jean-Marc Fritschy
Prof. Dr. Sebastian Jessberger

Zürich, 2016

Doktorvater: Professor Fritjof Helmchen A-L. Berthold van der Bourg

Funktionelle Reifung der sensorischen Reizverarbeitung im sich entwickelnden Barrel-Cortex der Maus

Zusammenfassung

Die Wahrnehmung von Berührungen ist eine essentielle sensorische Modalität, die es Organismen erlaubt mit ihrer Umgebung zu interagieren. Die Erforschung von sensorischer Integration und Wahrnehmung ist essentiell für das Verständnis von neuronalen Netzwerken. Die Wahrnehmung von Berührungen werden im Neocortex von Säugetieren in hoch organisierten neuronalen Netzwerken verarbeitet. Das Schnurrhaarsystem (auch Whisker-System genannt) von Nagern ist ein ausserordenlich elegantes Modell um sensorische Reizverarbeitung und ihre neuronale Repräsentation im Neocortex zu sudieren. Obwohl über viele Aspekte der neuronalen Verarbeitung im erwachsenen Whisker-System vieles bekannt ist, ist über die funktionelle Entwicklung in den ersten Wochen nach der Geburt wenig bekannt im jungen Tier. In dieser Doktorarbeit habe ich die Repräsentation von sensorisch-evozierter Aktivität im sich entwicklenden Barrel-Cortex untersucht. Ich habe die neurophysiologischen Eigenschaften der Antwortdynamiken von Neuronen charakterisiert, welche sich in einem begrenztem Zeitfenster entwickeln. Diese Entwicklung verläuft zeitgleich mit dem Beginn von aktivem Erkundungsverhalten von jungen Mäusen. Weiterhin konnte ich zeigen, dass die neuronale Repräsentation von Whisker-evozierten Stimuli sich in einer kortikalen schicht-spezifischen Art entwickeln. Zudem konnte ich zeigen, dass die sensorische Codierung von diesen Reizen sich gleichzeitig mit dem aktiven Schnupperverhalten entwickelt. Des weiteren konnte ich zeigen, dass die Reizverarbeitung bei Reizen mehrerer Whisker sich im gleichen Zeitfenster entwickelt. Diese Befunde liefern einen fundamentalen Einblick in die Entwicklung neuronaler Netwerke im primären somatosensorischen Cortex (Barrel-Cortex) von Nagern.

Kapitel 1 gibt einen generellen Überblick über die neuronale Verarbeitung von Whisker-induzierten Berührungen im Nager. Zudem wird die Entwicklung von neokortikalen Strukturen und deren biologischen Grundlagen für die Bildung von neuronalen Netzwerken eingeführt. Im zweiten Teil von Kapitel 1 führe ich die technischen Werkzeuge ein, welche es erlauben neuronale Aktivität zu messen. Im letzten Teil von Kapitel 2 werde ich die experimentellen Vorgehensweisen und spezifischen Ziele der Doktorarbeit vorstellen.

Kapitel 2 enthält Resultate meines Hauptprojektes welches ich während meines Doktorats durchgeführt habe. Die Resultate werden in Form eines wissenschaftlichen Aufsatzes präsentiert, welcher in der wissenschaftlichen Fachzeitschrift *Cerebral Cortex* veröffentlich wurde. In dieser Studie habe ich ein neuartiges Stimulationssystem entwickelt, welches es erlaubt neuronale Antwortdynamiken verschiedener Biegungen des Whisker zu messen (laterale Ablenkungen und axiale Antipper der Schnurrhaare). Das System wird im **Anhang A** ausführlich dokumentiert. Die Daten, welche in diesem wissenschaftlichen Aufsatz präsentiert werden, liefern eine detaillierte Beschreibung der Entwicklung von sensorisch-evozierter Aktivität im Barrel-Cortex der Maus im Zeitfenster zwischen postnatalem Tag (P) 10 und P28, insbesondere im kurzen Zeitfenster um P13, wenn Tiere ihre Augen öffnen und beginnen aktiv ihre Umgebung mit ihren Whiskers zu erkunden. Wir konnten zeigen, dass sensorisch-evozierte Aktivität sich in Schicht (L) 2/3 und L4 mit heranwachsendem Alter verringert, wobei diese sich in L5 und L6 erhöht. Oberflächliche und tiefe kortikale Schichten zeigten zudem unterschiedliche Antwortdynamiken in Bezug auf neuronale Anpassung während der Entwicklung. Die Analyse einzelner Neurone ergab insbesondere, dass diese ihre Antwortselektivität gegenüber axialen oder lateralen Stimuli um den Entwicklungstag P14 herum erhöhen. Diese grundlegenden Befunde zeigen, dass die Entwicklung von sensorischer Verarbeitung schicht-spezifische Änderungen in einem kurzen und definierten Zeitfenster erfolgt, welches eng an die Entwicklung von aktivem Erkundungsverhalten koppelt.

Kapitel 3 enthält einen zweiten wissenschaftlichen Aufsatz, welcher für eine Publikation vorbereitet wird. Die hier vorgestellten Befunde enthalten Resultate meines zweiten Hauptprojektes, welches sich mit neuronalen Aktivitätsmuster von Einzel- oder Doppelstimulation von Whiskers während der Entwicklung befasst. Da wir in Kapitel 2 zeigen konnten, dass neuronale Antworten in einem kurzen Entwicklungszeitfenster reifen, haben wir uns in diesem Projekt darauf fokussiert, wie sich die Verarbeitung gleichzeitiger Reizung benachbarter Schnurrhaare entwickelt. Wir konnten schicht-spezifische Änderingen der neuronaler Antworten feststellen, welche eine erhöhte zeitliche und räumliche Präzision aufwiesen, erhöhte Modulation mit stärker werdenden Stimuli aufzeigten, sowie erhöhte Kommunikation zwischen Barrels erzeugten. Diese Änderungen äusserten sich am stärksten in den Schichten L2/3 und L4, welche zeitlich mit dem Beginn aktiven Erkundens einhergingen. Weitere Änderungen betreffen die differentielle Aktivierung während sequentieller Stimulation zweier Whisker, was auf die Reifung rezeptiver Felder hinweist. Zusammenfassend charakterisieren diese Befunde räumlich-zeitlich begrenzte Antwortdynamiken von multi-sensorischen Stimuli während dem Beginn von aktivem Tastverhalten.

In **Kapitel 4** werden die Resultate, welche in den Kapiteln 2 und 3 behandelt wurden, disku-

tiert. Dieses Kapitel behandelt im Detail, wie sich die hier präsentierten Forschungsergebnisse in die jetzige Literatur einbinden und welche Fortschritte sie im Bezug auf unser Verständnis über neuronale Entwicklung des Tastsinnes bedeuten.

Thesis advisor: Professor Fritjof Helmchen A-L. Berthold van der Bourg

Functional Maturation of Sensory Coding in Developing Mouse Barrel Cortex

Abstract

Touch perception is an essential sensory modality enabling organisms to interact with their world. The study of sensory integration and perception are essential for the understanding of neural circuit function. In the mammalian neocortex, sensory information is represented as coordinated activity in highly organized neuronal populations. The rodent whisker system has been an exceptionally useful model to study sensory-evoked neural representations in neocortex. Although many aspects of neuronal computation in the adult rodent whisker system are well understood, little is known about its functional maturation. In this doctoral thesis, I investigated sensory-evoked activity in developing mouse barrel cortex and characterized the neurophysiological properties of response dynamics in a critical developmental time period when mice start to actively explore their environment. I found that the neural representation of distinct whisker-evoked stimuli mature in a layer-specific manner and that sensory coding develop at the onset of active whisking behaviors. Furthermore, sensory integration of multi-whisker evoked activity matured in the same developmental time period. These findings provide insights into the maturation of neural circuit function of rodent barrel cortex.

Chapter 1 will provide a general overview of rodent whiser-evoked touch perception, the development of neocortical structures and the biological basis for neural circuit construction. Furthermore, I will introduce the technical tools used to measure neural circuit dynamics. The last part of Chapter 1 will introduce the experimental approaches and specific aims of the doctoral thesis.

Chapter 2 contains results of my main project conducted during my doctoral thesis work in form of a research article which has been published in the journal *Cerebral Cortex*. In this study, I used a novel whisker stimulation system to reveal neural responses evoked by different types of whisker deflections (lateral deflections and axial tapping of the whisker) in the developing mouse barrel cortex. The stimulator is presented in detail in **Appendix A**. The data presented in this research article provide a characterization of the developmental temporal profile of sensory-evoked activity in barrel cortex of mice between postnatal day (P) 10 and P28, including in

particular the short time window around P13 when animals open their eyes and start actively exploring the environment with their whiskers. Sensory-evoked activity decreased in L2/3 and L4 with age, whereas it increased in L5 and L6. Superficial and deep layers also differed with respect to neuronal adaptation and developmental profile. Most notably, analysis of single neuron responses revealed emerging response selectivity for axial or lateral stimuli around P14 in L2/3, L5 and L6. Together, these findings demonstrate that maturation of sensory processing involves substantial, layer-specific changes in a short time-window at the onset of active whisking behavior.

Chapter 3 is a second manuscript that is currently in preparation for publication. The presented findings of my second thesis project focus on the neuronal dynamics evoked by single- or multi-whisker stimulation in developing mouse barrel cortex. Sensory-evoked activity matures in a critical developmental time period at the onset of active whisking in a layer-specific fashion. In this work I investigated in further detail how processing of temporally distinct single-whisker stimuli is processed and how spatially distinct dual-whisker stimuli are encoded in and across barrel columns at the onset of active whisking behavior. We could show that whisker-specific responses included an increased layer-specific response precision, increased modulation by stimulus intensity and enhanced cross-columnar communication. These changes were most profound for L2/3 and L4 and occured at the onset of active whisking behavior.The differential activation profiles upon sequential dual-whisker stimulation indicates whisker-specific maturation of receptive field properties. In conclusion, these findings characterize how spatiotemporal response dynamics evoked by single- or multi-whisker stimuli develops at the onset of active whisking behaviors.

Chapter 4 discusses how the findings presented in Chapters 2 and 3 integrate into the current literature and expand the current knowledge in the field of barrel cortex development and sensory coding in general.

Contents

List of figures

List of tables

Dedicated to my parents.

For man, the sense which is most discriminating is that of touch. With respect to the other senses, man is far inferior to the other animals; but with respect to the sense of touch he excels by far in discrimination over the other animals

From Aristotle's *De anima*

1

General Introduction

The perception of an object through touch, the ability to play an instrument or to write down thoughts with a pen on paper all rely on the interplay of sensory modalities and the transmission and processing of information in the brain. Somatosensation - the perception through touch - plays an essential role in interacting with the world for nearly all living organisms. Without touch perception, control of fine coordinated movements such as grasping a small object would not be possible. Somatosensation also plays a key role in social and reproductive behaviors, survival and intricate interaction with the surrounding environment. Therefore it is not surprising that somatosensation is one of the most well studied sensory modalities in neuroscience. The study of somatosensation plays an essential role in understanding the fundamentals of sensory integration in the brain.

My doctoral thesis focuses on understanding the cortical representation of tactile sensory information in developing mouse somatosensory cortex. Here, I will provide an overview of the fundamental background on the development of cortical structures involved in touch perception and outline why rodent barrel cortex is an excellent model to study somatosensation. I will also provide a short overview of *in vivo* electrophysiology and two-photon calcium imaging as the key techniques used in this study to measure neural network dynamics.

1.1 Rodent barrel cortex as a model system to study the neural processing of touch

The study of sensory integration in neocortex has been a fundamental field of neuroscientific research for many decades. How sensory information is transmitted and encoded in the brain is an essential question in the field. The rodent barrel cortex is an exceptionally elegant and useful model to study sensory integration in the brain. One of the main reasons for its immense popularity in neuroscience was the discovery of its highly organized anatomical organization in the mouse barrel cortex by Van der Loos and Woolsey in the early 1970's, who coined the definition of *barrel cortex* based on its morphology (Van der Loos and Woolsey, 1973). Vernin Mountcastle introduced the idea of a cortical column already in 1957 through recordings in cat visual cortex (Mountcastle, 1957), where neurons processing information of the same sensory modality are organized in a column-like structure in cortex. The discovery of the barrel field and its organization by Van der Loos and Woolsey further strengthened this concept and helped greatly in understanding how peripheral information shapes the development of cortical sensory areas (Van der Loos and Woolsey, 1973). These aspects made barrel cortex an attractive model for neuroscience research.

The barrel cortex is part of the primary somatosensory cortex and processes tactile information from whiskers facial hairs on the contralateral snout of the animal. Information of each whisker is transmitted to the neocortex in a somatotopic fashion through the trigeminal nerve, the trigeminal ganglion and through the thalamus, projecting to a highly organized structure

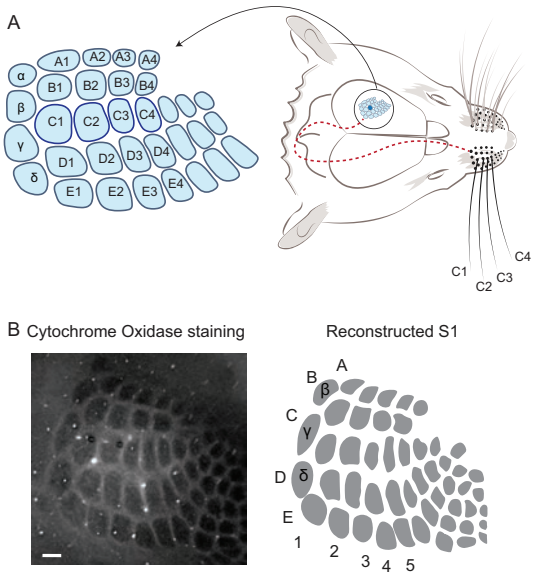

Figure 1.1: Anatomy of the rodent whisker system: **A:** Rodent primary somatosensory cotex is a somatotopic representation of the whisker on the whisker pad on the contralateral side. Information of each whisker is processed and represented in a cortical column. Each column is identified by a row number and column letter. Before peripheral inputs reach barrel cortex, they are relayed through multiple brain areas, including the trigeminal nerve bundle, the brain stem and thalamus (in red a schematic projection pathway is indicated, see **Figure 1.4** for a detailed representation of the pathways and projections). Based on this highly organized structure, rodent somatosensory cortex is also referred to as barrel cortex, as each cortical column representing one whisker has the shape of a barrel-like structure in L4. **B:** Barrels can be visualized by histological staining techniques through cytochrome oxidase immunohistochemistry (COX), revealing the granule cell aggregates of L4 neurons. In this example, tangential sections were cut from a P27 animal after such staining (see Methods of Chapter 2 for details). Scalebar 200 µm. The right panel shows a reconstructed barrel map based on the COX staining as seen on the left. Example is taken from data presented in Chapter 2

that is represented in the cortex as near-circular structures called *barrels* that correspond to each whisker along the antero-posterior and medio-lateral axis (**Figure 1.1A**). Thalamic afferents innervate cortical layer (L) 4 in barrel cortex in a highly organized fashion, which can be revealed by tangential sectioning of brains treated with cytochrome oxidase immunohistochemistry (COX, see **Figure 1.1B**). Based in its highly organized cytoarchitecture and accessibility revealed through pioneering COX staining experiments, the whisker system has emerged as a model to study many aspects of sensory perception, such as whisker-based decision making (Guo et al., 2014), multi-sensory integration during locomotion (Sofroniew et al., 2015), sensory adaptation and frequency discrimination (Musall et al., 2014).

The ability to modify and perturb the maturation of the cortical representation of a single or multiple whiskers is what makes barrel cortex an accessible system to study cortical development (Van der Loos and Woolsey, 1973). The ability to modify in a very precise way individual peripheral inputs and observe the impact on the development of the barrel cortex is what distinguishes this system from other sensory modalities. Studies on the visual system rely on the

deprivation of visual input through monocular or binocular eye closure, or the exposure to a confined stimulus set, usually leaving the system intact (Hubel and Wiesel, 1963). In barrel cortex, however, the system can be partially modified by only removing a subset of whiskers, opening up the possibility to study the impact of sensory deprivation and the reorganization of the network with the remaining intact input. Furthermore, easy implementation of physical movements in various directions of the whisker into sensory-evoked activity makes the system accessible for well-controlled stimulation experiments. However, the physical variables underlying whisker-evoked perception are manyfold and pose an extra challenge (Gopal and Hartmann, 2007; Quist et al., 2014). In recent years, the understanding of the physical variables underlying touch perception such as reporting the distance to an object (Pammer et al., 2013) or aspects of multi-sensory receptive field properties (Ramirez et al., 2014) have significantly increased. Not only are whisker forces essential for a rodent to perceive and report object shape and location, but it also requires input from many whiskers to discriminate surface structure and other object properties, which are represented in complex multi-whisker receptive fields. A better understanding of whisker-evoked signal transmission has lead researchers to use this information for decision making experiments, bridging the gap between sensory input, cell-type specific computations and higher-order communication between brain areas, which ultimately lead to a behavioral outcome (Chen et al., 2013; Sachidhanandam et al., 2013; Chen et al., 2016; Sachidhanandam et al., 2016).

1.2 Development of rodent somatosensory cortex

The development of barrel cortex is a multi-step process relying on the interaction of appropriate maturation of thalamocortical afferents and the formation of cortical layers. Most of the neurons in barrel cortex are already produced before birth. They are generated around embryonic day (E) 10.5 and E11, while the neocortical architecture of barrel cortex is fully developed around postnatal day (P) 7 and reaches adult levels of connectivity around P16 (Erzurumlu and Gaspar, 2012).

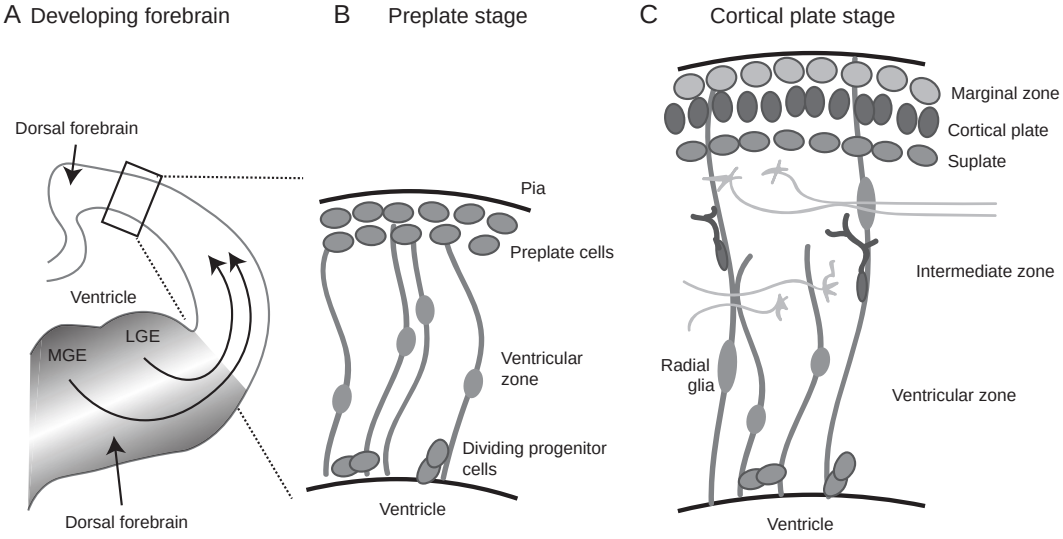

Figure 1.2: Formation of neocortex: Neocortex is formed by two sources of cells and pathways. **A:** During development of the forebrain, the medial and lateral ganglionic eminences (MGE nd LGE) give rise to neurons which migrate toward the cortex. They arrive tangentially to the radially oriented ventricular migration route. The MGE gives rise to interneurons of neocortex. **B:** During the pre-plate stage, neurons are born in the ventricular zone and migrate inside-out to form preplate cells. These cells subsequently differentiate into the marginal zone and the subplate. **C:** The cortical plate is formed where neurons continue to be born from the ventricular zone. These neurons migrate along radial glia cells through the intermediate zone originating from the cortical plate where they then form layer 6 to 2 of neocortex (and barrel cortex) in an inside-out fashion. Adapted and modified from (Nadarajah and Parnavelas, 2002)

Neurons in neocortex (and barrel cortex) are derived from two pools of *progenitor cells* in the ventricular and subventricular zone (**Figure 1.2**) which migrate along radial glia cells to find their targets. The progenitor cell pool remains constant after mitotic division, so that one of the two cells can give rise to more cells while the other can be part of the formation of cortex. In neocortex, progenitor cells consist of radial glia cells located in the marginal zone (see **Figure 1.2C**). Radial glial cells give rise to neurons by asymmetric division in the ventricular zone (Noctor et al., 2004). Generated cells then migrate along the radial glia cells into the intermediate zone (**Figure 1.2C**). However, progenitor cells can also produce a cell that is itself a progenitor which migrates along radial glia cells to the subventricular zone where it performs a symmetric division to create two postmitotic neurons (Noctor et al., 2004; Fox, 2008). There is increasing evidence that cells produced from the same progenitor have the tendency to integrate in the same cortical column. Therefore, cortical neurons in a barrel column might be derived from the same progenitor (Fox, 2008). Although all dorsal progenitors give rise to glutamatergic

neurons, their exact cellular identity is specified by the origin from which progenitor cells arise. As depicted in **Figure 1.2A**, not only local radial glia cells can give rise to cortical neurons but also two sources of progenitor cells in the ventral forebrain: the medial and lateral ganglionic emineces (MGE and LGE respectively). However, progenitor cells from LGE and MGE give rise to GABAergic interneurons, which only later integrate into the cortical network during development after completing their tangential migration. Cajal-Retzius cells play an important role in the formation of the pre-plate and sub-plate structures during early development and also originate from the dorsal forebrain (Lavdas et al., 1999). Neurons derived from radial glia cells in the ventricular zone are exclusively excitatory.

The development of cortical layers from the progenitor cell pool follows an inside-out process

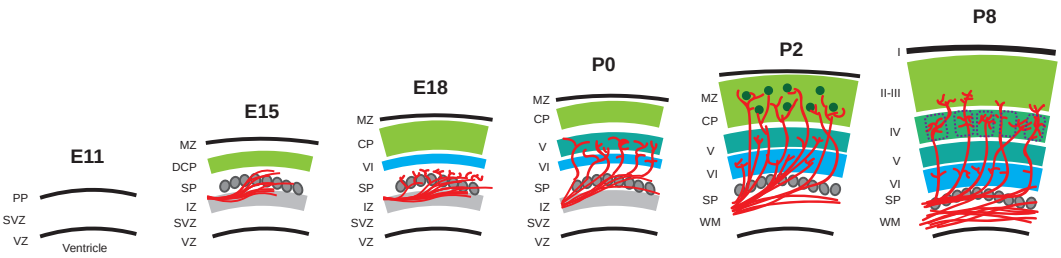

Figure 1.3: Development of cortical layers and maturation of thalamo-cortical inputs: In this schematic illustration the maturation of cortical layers and the developmental time points are shown (E: embryonic day; P: postnatal day). At E11, the ventricular and subventricular zones (VZ, SVZ) as well as the preplate (PP) are formed (**Figure 1.2**). Around E15 the subplate (SP) post-mitotic cells migrate to the outer edge of the cerebral wall. They form the marginal zone (MZ) and the deep cortical plate (DCP). Thalamocortical afferents start to penetrate through the sub-plate into early cortex. At E18, layer(L) 6 is formed first (inside-out maturation of neocortex). Branches of thalamocortical afferents migrate towards L6. At P0 L5 is formed. Approximately at P2 the cortical plate is innervated by thalamocortical fibers. The afferents start to segregate in their target regions and barrels subsequently until P8. At P8 maturation of L2/3 is complete and barrels as cellular aggregates are clearly visible. Adapted and modified from (Piñon et al., 2009)

as they migrate along radial glia cells. An important landmark of neocortical maturation is the formation of the pre-plate around E11. It is the substrate for further maturation of early cortical structures around E15 such as the deep cortical plate (**Figure 1.3**). As depicted in **Figure 1.2C**, the sub-plate and cortical plate neurons arrange below the marginal zone to form early structures of neocortex. At around P0, cortical layer 5 is formed from the radial glia cell pool. At the same time-point thalamocortical afferents start to innervate these structures. This innervation is important for the appropriate formation of cortical columns in barrel cortex (see

section 1.2.2 for further details). Around P2, progenitor cells give rise to most of the neurons of layer 5. At the same time thalamocortical afferents migrate into the cortical plate (CP). P8 marks the time, at which cortical layer formation in terms of neuronal migration and cell proliferation is finished. In parallel, thalamocortical afferents form synaptic connections with their target neurons in layer 4, creating a dense mesh of synaptic connections (**Figure 1.3**).

1.2.1 Development of anatomical pathways involved in active whisking and whisker information processing

The appropriate formation of barrel cortex relies on the timely maturation of sub-cortical areas that are essential to mediate whisker-evoked sensation. As depicted in **Figure 1.3** thalamocortical afferents start to innervate the deep cortical plate and sub-ventricular zone around E15 to E16. However, before these neurons project to their target regions, they receive innervation from trigeminal ganglion neurons around E12 (**Figure 1.4**). The trigeminal ganglion is the gatekeeper between the mechanoreceptors in the whisker pad and the sub-cortical structures in the thalamus. The infraorbital nerve (ION) - a division of the trigeminal nerve bundle - innervates the whisker follicles already around E11. Axons of the trigeminal ganglion also innervate the whisker pad and together with the ION form the trigeminal nerve bundle. These neurons convey information to the trigeminal brainstem nuclei and find their targets around E12 (**Figure 1.4A**). The principal sensory nucleus of the trigeminal nerve (PrV) is the main relay station to transmit information to the ventral posterior medial thalamic nucleus (VPm). Note that the axonal projections to VPm form around E17 while the thalamocortical inputs from VPm and the posterior medial thalamic nucleus (POm) start to innervate cortex around P0 (also see **Figure 1.4**).

An important aspect of the maturation of barrel cortex is the correct formation of somatotopy along the thalamocortical pathways during development. In barrel cortex, somatotopy is conserved in thalamic structures. The barrel-field map is already discernible in the PrV and the VPm. The barrel-like patterns in the PrV have been termed *barrelettes* (Van Der Loos, 1976)

and *barreloids* in the VPm (Durham and Woolsey, 1984), respectively. These structures were discovered by sensory deprivation experiments by Van der Loos & Woolsey in the 1970's and 1980's, as these structures are malformed if the formation of axonal connectivity through lesions is disturbed (**Figure 1.5**).

Although neurons find their thalamic targets along the transmission pathway through the trigeminal nerve and the brainstem early in development, the patterning of barreloids and barrelettes is only seen at a later developmental age. Barrelettes in PrV form around P0, while barreloids form around P2-3 in VPm (**Figure 1.4B**, (Van Der Loos, 1976; Durham and Woolsey, 1984)). Note that the patterning of these structures differs between species. In rat cortex these structures form around E12-19 while they only start to form around P0 in mice (Chiaia et al., 1994; Waite et al., 2000; Ma, 1993). The formation of the subcortical areas and the transmission of whisker-evoked activity is essential for cortical maturation as described in section 1.2.2.

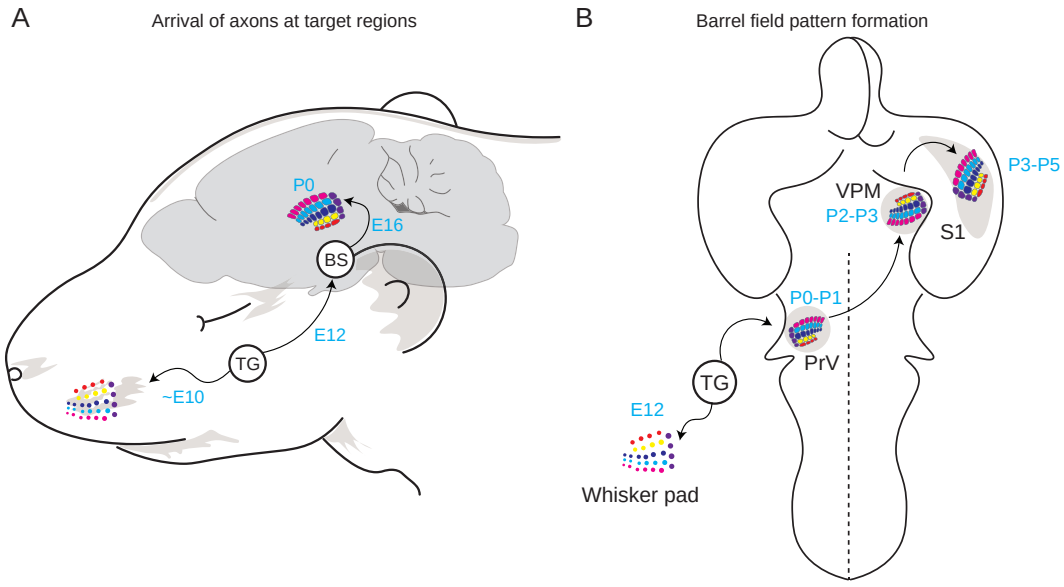

Figure 1.4: Timing and arrival of axonal afferents and pattern formation in subcortical target regions: **A:** Schematic representation of axon arrival at target regions during early embryonic development (projected onto a schematic representation of a mouse pup). TG: Trigeminal ganglion. TH: Thalamus. BS: brain stem. Note that barrel cortex is not shown on the contralateral side for visualization purposes. **B:** Formation of barrel field related structures in the thalamus and neocortex. PrV: principal sensory nucleus of the trigeminal nerve, VPM: ventroposteriormedial nucleus of the thalamus. S1: primary somatosensory cortex. Adapted and modified from (Erzurumlu and Gaspar, 2012)

1.2.2 Critical period plasticity during barrel cortex maturation

Developing sensory systems show high susceptibility to alterations of peripheral inputs in a critical developmental time period of sensory experience that shapes the morphological and functional organization of their circuits. Therefore the *critical period* defines a time window when the formation of the cortical circuitry, the balancing of the inhibitory and excitatory network and the formation of extracellular matrix structures all rely on sensory-experience (Hensch, 2005; Cabungcal et al., 2013; Erzurumlu and Gaspar, 2012). One of the most famous studies on critical period plasticity and sensory-experience-dependent maturation was performed by Hubel and Wiesel in the 1960's where deprivation of sensory input would lead to impaired development of the visual system in young kittens (Hubel and Wiesel, 1963). Van der Loos and Woolsey extended this concept to barrel cortex and showed that if whiskers were trimmed during early development, their cortical representation in barrel cortex is impaired (Van der Loos and Woolsey, 1973). Consequently, the concept of a *critical period* defining a time where sensory input is required for the correct formation of cortical structures such as barrel cortex was put forward (**Figure 1.5** for examples). The concept of critical period plasticity does not only apply to the formation of barrels but also to many other aspects of barrel cortex (and sensory cortex) development in general. Many critical periods have been defined for the maturation of barrel cortex since the pioneering experiments by Van der Loos and Woolsey, including critical period plasticity for local connectivity inside a barrel column (Stern et al., 2001; Wen and Barth, 2011). Plasticity is not only confined to early cortical development but reaches beyond early maturation into adulthood (Fox, 2002).

In terms of barrel cortex maturation, alterations of connectivity before P4 lead to complete disruption of the formation of cortical column organization as depicted in **Figure 1.5**. These alterations are mainly a result of the disruption in the intricate timing of the axonal pathfinding of thalamocortical afferents in their target regions as they are crucial for the formation of dense connectivity in L4. How these connectivity motifs are formed and how they impact neural computation and sensory coding, is not well understood.

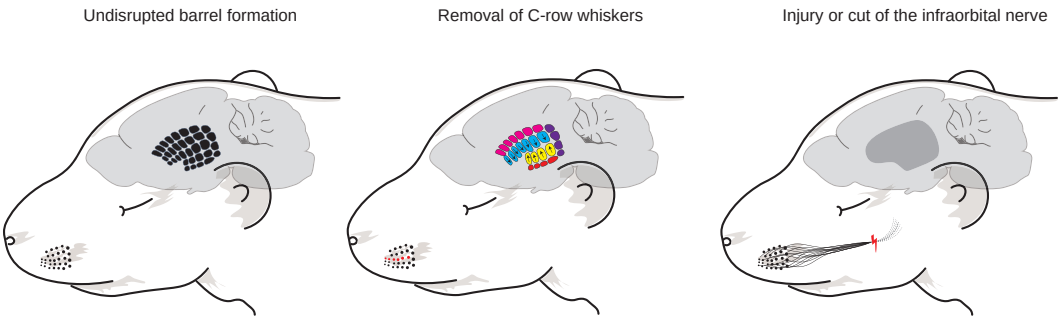

Figure 1.5: Structural plasticity of barrel cortex formation: During early development, removal (plucking or cutting) of whiskers leads to a modified maturation of the cytoarchitecture of barrel cortex and increase in the size of neighboring barrel columns. Lesion of the infraorbital nerve bundle leads to a complete absence of the barrel cortex architecture. Adapted and modified from (Erzurumlu and Gaspar, 2012)

1.2.3 Development of functional local connectivity in barrel cortex

Critical period plasticity is not only confined to the development of cortical structures but also to local intra- and inter-columnar connectivity. As I have introduced in section 1.2, the formation of cortical layers in mouse cortex is complete around P8 but most of the local connectivity has not yet fully matured. As thalamocortical afferents strengthen their synaptic connectivity with neurons in L4 around P8, the connectivity to other cortical more superficial areas like L2/3 has not yet fully matured. Only around P10-P14, connectivity between neuron of L4 and L2/3 is fully established (Stern et al., 2001; Maravall et al., 2004; Shoykhet, 2005). Deprivation of whisker input at this age leads to alterations in the spiking properties of cells in these layers (Maravall et al., 2004). Furthermore, local connectivity between neurons in L2/3 also undergoes major reorganization in a short developmental time-period between P13-P16, right after the critical period of L4 to L2/3 connectivity (Wen and Barth, 2011). This critical period is essential for the formation of horizontal synaptic connections between neurons in L2/3, evident in the increase in synaptic density at that stage (Chandrasekaran et al., 2015). In the same time-period, the response properties of populations of neurons in L2/3 change drastically, from highly synchronized to non-synchronized activity patterns (Golshani et al., 2009). This change in activity is believed to be internally mediated and does not depend on sensory input, as

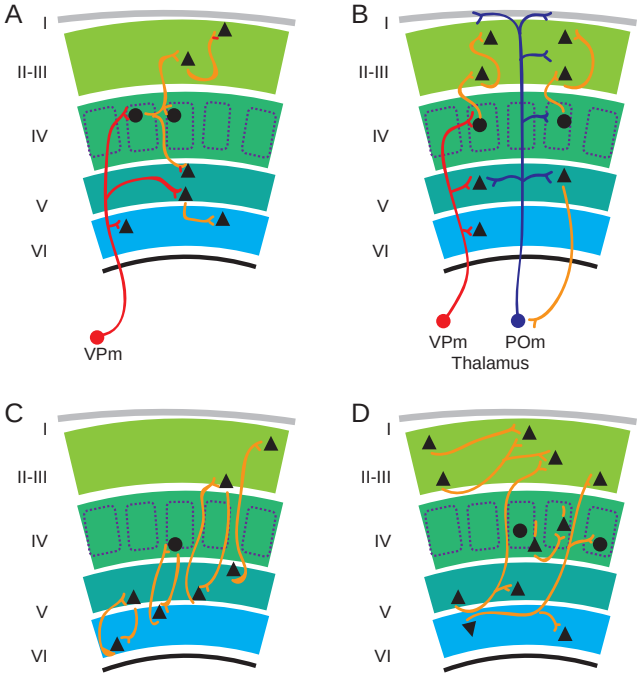

Figure 1.6: Thalamo-cortical and cortico-cortical excitatory pathways in barrel cortex: A: The ventral posterior medial thalamic nucleus (VPm) sends serial feedforward information to targets in L6, 5 and 4. Activated L4 neurons themselves activate further downstream targets in L4 and L2/3 and the excitatory subpopulation activates neurons in L6. **B:** The second feedforward excitatory pathway from the thalamus originates in the posterior medial thalamic nucleus (POm) which targets different subsets and regions of barrel cortex than the VPm pathway. **C:** Neurons in different layers are connected through recurrent excitatory circuitry and build a complex mesh of loops inside and across cortical columns. **D:** The horizontal connectivity between barrel columns occurs across all layers. The network between L4 neurons is sparser compared to horizontal connectivity in other layers. Adapted and modified from (Fox, 2008)

deprivation does not alter its maturation (Golshani et al., 2009). However, feedforward inputs from thalamo-cortical afferents during early development are the key initiators for the creation of local barrel cortex connectivity (Van der Loos and Woolsey, 1973; Van Der Loos, 1976).

The thalamo-cortical and cortico-cortical feedforward inputs in adult barrel cortex have been well studied (**Figure 1.6**). Whisker-evoked information is transmitted to barrel cortex by two feedforward thalamo-cortical input streams: the ventral-posterior medial thalamic (VPm, **Figure 1.6A**) and the posterior medial thalamic (POm, **Figure 1.6A**) pathways. The VPm afferents preferably connect with neurons in L4, 5 and L6, while thalamo-cortical afferents from the POm target neurons in L5, L4 and L2/3. As depicted in **Figure 1.6B-C**, the local circuitry shows complex connectivity motifs, of which following are the most predominant:

- Local columnar projections are made between L4 and L2/3 cells.
- L2/3 and 5 cells connect reciprocally inside a cortical column (and barrel column).
- Reciprocal connections between L4 and L6 cells
- Horizontal connections between L4 neurons (sparse)

How the maturation of such local cortical connectivity defines the computational power of these circuits is unclear. Furthermore, these connectivity motifs only refer to direct inputs from thalamo-cortical input streams. How local connectivity aids in shaping a precise percept and how these networks are modulated by inhibition during the critical developmental time-period remains elusive. The development of further connectivity between higher sensory areas like secondary somatosensory cortex or motor cortex and pre-frontal cortex is also an important aspects, that needs to be further explored. In my doctoral thesis I focused on a confined developmental time window between P10 to P28 when mice start to actively explore their environment. These behavioral changes happen at the same time when the local connectivity of L 2/3 neurons is undergoing major changes. The thesis work presented in Chapter 2 will provide a descriptive overview of the response properties of neurons in barrel cortex in this important developmental time window, which will aid in better understanding changes in local computation that are most probably reflected by changes in local connectivity. These findings provide first evidence on how sensory coding matures in parallel with active whisking behavior. In Chapter 3 I present further evidence that intra- and inter-columnar whisker-specific response properties undergo major changes at the onset of whisking behavior.

1.3 Measuring neural network activity in vivo

The combined usage of the light microscope and the Golgi staining technique through the extensive work by Ramon y Cajal (1852-1934) on fundamentals of neuronal morphology mark an important step forward for modern neuroscience. Ramon y Cajal was one of the first scientists to link morphology in the brain tissue to function: when contemplating upon his masterful drawings, one can appreciate little arrows on some of them (**Figure 1.7**), indicating that he was contemplating how information is transferred between cells based on neuronal morphology, structure and connectivity. Since the work by Cajal, modern recording techniques have emerged to study not only single neurons but large ensembles in intact neuronal tissue. Electrophysiology was the first technique enabling scientists to characterize single cell responsiveness, not only *ex vivo* but also *in vivo*, i.e. in the living brain. Its usage lead to important findings of cortical organization principles and single neuron encoding capabilities such as the characterization of receptive field properties of neurons in the visual cortex of the cat (Hubel and Wiesel, 1962). *In vivo* patch clamp electrophysiology is an established technique in the field as it allows to directly assess intracellular membrane potential fluctuation with excellent temporal resolution (several kHz) and high signal-to-noise ratio (Erwin Neher and Sakmann, 1992). An elegant usage of this technique is the combination of intracelluar measurements of a cell and filling it with a fluorescent marker to study the link between morphology and function (**Figure 1.8**). Electrophysiological recording techniques have a rich history in neuroscience, as

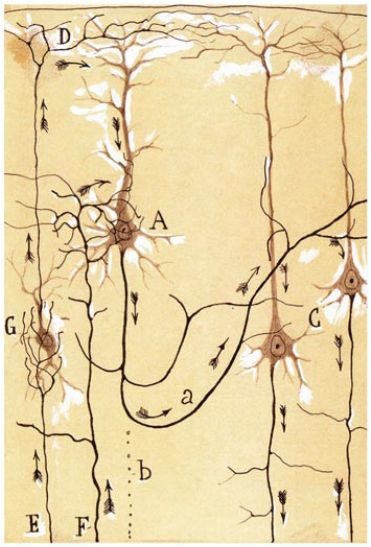

Figure 1.7: Illustration of signal flow in pyramidal cells: Illustration from Ramon y Cajal showing the morphological organization of cells in neocortex. Little arrows indicate the flow of information through the network. Adapted from (Cajal and May, 1991)

techniques shifted from electroencephalography (EEG) recordings in the late 1920's to *in vivo* whole cell electrophysiology and later to extracellular recording techniques using electrodes embedded in neural tissue. The development of the tetrode approach (**Figure 1.8B**), and later the development of large silicon probe recording arrays (**Figure 1.8C**) enabled researchers to measure spiking activity of extended areas of neuronal tissue. The silicon-probe approach will be explained in more detail in subsection 1.3.1 as it was a core technique used in this doctoral thesis. In addition to the development of modern electrophysiology recording techniques, the field of two-photon calcium imaging has experienced an immense increase in popularity enabling researchers to image large populations of neurons and label specific subsets of neuronal tissue. A short overview of its usage will be presented in subsection 1.3.2.

In my doctoral thesis, I aimed to utilize silicon probe recordings and two-photon calcium imaging to study the neurophysiological maturation of barrel cortex function.

1.3.1 Principles of silicon-probe electrophysiology

Methods capable of isolating, identifying and manipulating large populations of neurons of the investigated circuits at a single- and multi-neuronal level are essential for studying brain function (Buzsáki et al., 2015). Before the introduction of advanced recording techniques capable of measuring activity from large ensembles of neurons, other more simple but robust techniques were used to measure neural activity. One such technique is single-cell intracellular electrophysiology, which has been one of the most revealing and established recording techniques in neuroscience (Adrian and Moruzzi, 1939). The investigation of neuronal circuit dynamics such as spiking activity of ensembles of neurons can be measured with tetrodes (McNaughton et al., 1983; Wilson and McNaughton, 1993). Tetrodes - as their name suggests - consist of four extracellular recording wires bundled in a tight array, enabing researchers to record from of a dozensneurons simultaneously (**Figure 1.8** (Buzsáki et al., 2015)). Their particular arrangement allows one to isolate the activity of single cells with high fidelity by comparing relative signal strength across recording sites (**Figure 1.8B**). However, tetrodes can only capture activity from neurons in the vicinity of the recording tip. To be able to record from many neurons and pre-

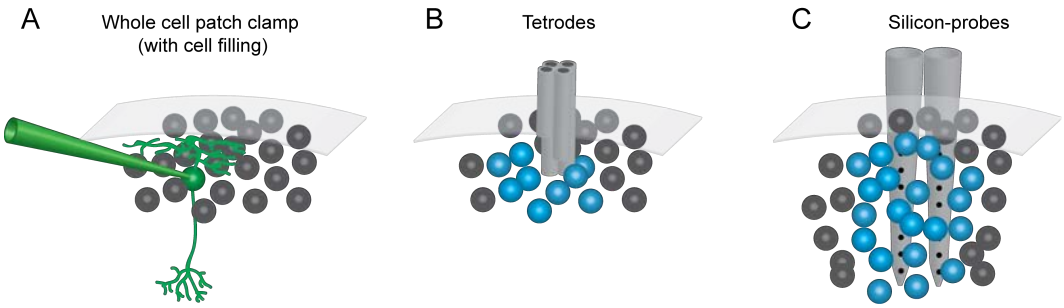

Figure 1.8: Measuring neural activity with electrophysiological techniques: **A:** Whole-cell recordings can reveal intracellular response properties of single cells with unprecedented fidelity. In combination with filling of a marker, the morphology can be linked to these response properties.**B:** Exctracellular recordings with tetrodes can capture activity of dozens of neurons in its vicinity. **C:** Modern fabrication approaches allowed to implement silicon-based probes consisting of high density arrays of recording sites. These silicon-probes are capable of capturing neural activity of hundreds of neurons across multiple cortical layers.

ferrably layers simultaneously, several technical challenges had to be overcome. These challenges included the design of compact high density arrays that maintain small dimensions, the embedding of these arrays in a stable carrier material and a massive reduction in electrical wiring for signal transmission and processing. The development of semi-conductor-based recording arrays embedded in a silicon carrier (*silicon-probes*) by Kensall D. Wise (Wise et al., 1970) elegantly overcame these callenges (**Figure 1.8C**). The silicon based fabrication process allowed engineers to design and construct high-density arrays with very small dimensions while increasing the number of recording sites and therefore the area of neural tissue that can be recorded from. The small size of modern silicon probes also relies on the development of miniaturized signal processors and data acquisition hardware. The increased usability and availability of these tools enabled companies such as *NeuroNexus* to develop and distribute affordable and reliable silicon-probes for the recording of neural activity from large neural populations, up to the size of multiple cortical columns (Buzsáki et al., 2015). Although extracellular recordings cannot reveal neuronal properties such as spiking thresholds or extra- and intracellular post-synaptic potentials, they have the advantage that multiple aspects of extracellular electrical currents can be recorded and studied. These include the measurement of local field potentials (LFPs) which represent changes in local electrical transmembrane current flow of ensembles of neurons in the extracellular space of neural tissue. These responses can either consist of inward currents (depolarizing, excitatory)

or outward currents (hyperpolarizing, mostly inhibitory). These changes in current flow originate from contributions of multiple current sources and depend on various properties of the studied brain tissue (Einevoll et al., 2013). The second spatial derivative of the LFP signal - the current-source density (CSD, also see Chapter 2) - can aid in identifying layer-specific input and output streams present in the recorded tissue (Cuevas, 2014). Technically more challenging is the isolation of single-unit spiking from the recorded ensemble activity. Modern computational approaches comparable to triangulation algorithms in information technology allow to isolate the spiking waveform from a single neuron, given the signal is recorded from multiple recording sites (**Figure 1.9C**). These approaches apply cluster algorithms by analyzing the waveform shape and intensity of neural spiking across multiple recording sites and sort them by applying principal component analysis on these waveform parameters (Lehky et al., 2014). The isolation of single units therefore relies heavily on the distribution of the recording sites on the silicon probe. Multiple laboratories and companies have worked on improving the arrangement and density of these sites as well as optimized spike sorting algorithms (and their distribution through open-source software packages) to increase the amount of single units that can be isolated (Berényi et al., 2014; Buzsáki et al., 2015; Rossant et al., 2015). All these technical advances made it more feasible to investigate the maturation of neural circuit function with silicon-probes in this thesis.

The investigation of neural activity in developing tissue is challenging because of its small dimensions compared to adult cortex. Therefore it is crucial that the utilized silicon-probe consists of arrays with appropriate distances between recording sites. Most silicon-probes are designed with on-shank recording-site distances of more than 100 µm. This is a critical factor for successful isolation of single units and for capturing neural dynamics of a single layer reliably. The presented design in **Figure 1.9** is a custom-built silicon-probes with recording site distances of 50 µm, manufactured by *NeuroNexus*. This custom design, in combination with a novel whisker stimulatior, enabled us to study the functional maturation of neural tissue in mouse barrel cortex with high fidelity as presented in Chapters 2 and 3.

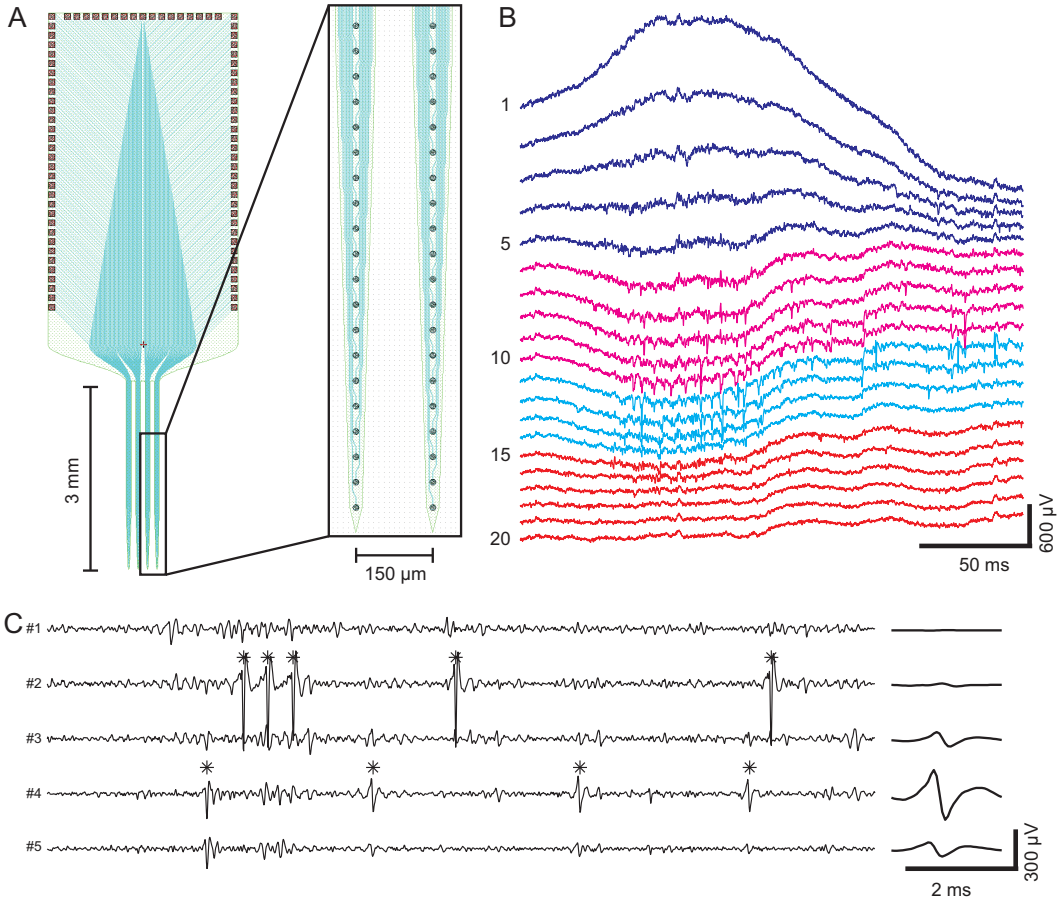

Figure 1.9: Recording neural activity with silicon-probes: **A:** Design schematic of a silicon-probe used to perform high-density electrophysiology. Probe designs vary in number of recording shanks and sites. The presented design consists of four shanks (3mm in length, spaced 150 µm apart). Each shank consists of a linear array of 20 recording sites, spaced 50 µm. Careful insertion of these probes into neural tissue allows to record from all cortical layers in vivo. The small spacing between recording sites also allows for spike sorting in juvenile mouse tissue (also see Chapter 2 for details). Courtesy of NeuroNexus. **B:** Raw example data of spontaneous neural activity obtained from one recording shank from adult mouse barrel cortex. Spontaneous spikes can be identified by short positive and negative peak waveforms in the activity profile. **C:** Example recording of spontaneous activity in a P30 mouse from 5 out of the 80 recording sites presented in B. Spikes are indicated by asterisk. The right traces show the average response amplitude of an isolated single-unit (channel 4). The closer the unit to a recording site, the higher the response amplitude (for detailed explanation see Methods in Chapter 2).

1.3.2 Principles of two-photon microscopy

In vivo two-photon laser scanning microscopy has become a powerful technique to measure neuronal activity in scattering tissue. The concept of two-photon microscopy has been introduced by Wilson and Sheppard in the 1980's (Wilson and Sheppard, 1984) and is based on fundamental physical properties that had already been postulated by Maria Göppert-Mayer in the early 1930's (Göppert-Mayer, 1931). The first implementation of a two-photon laser scanning microscope was presented by Winfried Denk and colleagues in1990 (Denk et al., 1990). A few years later, David Tank and colleagues demonstrated the application of a two-photon microscope to measure neuronal signals in living tissue using calcium indicators (Svoboda et al., 1997). The development of myriads of synthetic fluorescent molecules as well as the targeted genetic expression of fluorescent proteins in confined regions of tissue and cell types further widened the range of its applications for neuroscience research (Svoboda and Yasuda, 2006).

Principles of two-photon excitation

Laser-scanning fluorescence microscopy relies on the interaction of the absorption of photons through fluorophores and the subsequent emission and detection of fluorescent signal. Two-photon microscopy relies on the absorption of two photons within a very short time window (less than 10^{-15} s) that leads to a transition equal to a single photon absorption of twice the energy (**Figure 1.10**). If a fluorophore is excited through single photon absorption, it changes its energy state from a ground state E_{ground} to an excited state $E_{excited}$ (where $E_{excited} > E_{ground}$). After cascading through various vibrational levels in the excited electronic state and shedding energy as heat, the molecule arrives in the lowest excited state (**Figure 1.10A**). The energy absorbed by the molecule ΔE corresponds to the energy of a single photon for single-photon absorption ($E = \hbar\nu$, where $\hbar$ is the Planck constant, and ν corresponds to the light frequency). As the excited state is short-lived with a lifetime of a few nanoseconds, the fluorophore will transition back to its ground state. The energy difference after transition to the ground state will be released by the emission of a single photon. Because the fluorophore undergoes multi-

ple electronic vibrational transitions when falling back to its ground state E_{ground}, the emitted fluorescence emission has a smaller energy and longer wavelength than the absorbed photon (**Figure 1.10A**). This phenomenon is called Stoke's shift and occurs for nearly all fluorescent molecules. The fluorescence excitation and emission can lead to the destruction of a fluorophore due to photobleaching. Additionally, high doses of light excitation can lead to phototoxicity. These aspects are limiting the use of single-photon excitation microscopy in living organisms as high excitation energy is needed to detect fluorescent signals in the focus point (Svoboda and Yasuda, 2006). With two-photon microscopy, these effects remain highly localized as the probability of a fluorophore to absorb two photons depends on the square of the excitation intensity I^2. Two-photon excitation is therefore a non-linear process, making it very improbable to drive multi-photon excitation above or below the focus point. The physical fundamentals of two-photon excitation were postulated by Maria Göppert-Mayer in the early 1930's (Göppert-Mayer, 1931), but could only be experimentally confirmed after the invention lasers in the 1960's (Kaiser and Garrett, 1961). Göppert-Mayer (1931) postulated that a single-photon transition can be excited by the absorption via an intermediate virtual state in energy level $E_{virtual}$ (**Figure 1.10B**). Because each of the required photons' energy is only half the energy of the corresponding single-photon absorption, photodamage is greatly reduced as the near-infrared excitation light is less damaging. As most fluorescent dyes used in microscopy are excited in the visible range, near-infrared light sources are commonly used for two-photon imaging. Two-photon absorption spectra of commonly used fluorophores are rather broad (Svoboda and Yasuda, 2006) and therefore multiple fluorophores with different absorption spectra can be excited. Compared to single-photon excitation, two-photon excitation is a very improbable process. To render this modality useful for microscopy in living brain tissue, the excitation light needs to be both temporally and spatially confined, which is achieved through pulsed excitation and focusing. To achieve successful two-photon excitation, two photons need to be absorbed in a femtosecond time window. The probability of a successful absorption event depends on the two-photon absorption cross-section of a fluorophore, which is measured in units of Göppert-Mayer (GM;

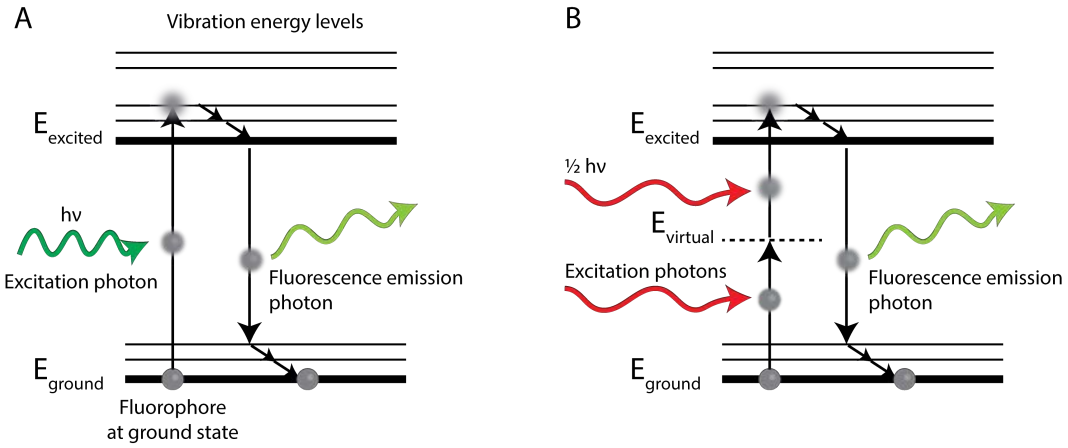

Figure 1.10: Jacobi-diagram of single- and two-photon excitation.: **A:** In single-photon excitation a fluorophore reaches a higher energy level through one photon excitation. This energy is released through a photon of the energy that is the difference between the excited and elevated ground energy levels. Intermediate levels display vibration energy levels that are reached withouth the emission of a photon. **B:** Two-photon excitation induces fluorescence through absorption of two photons. An intermediate virtual energy level is reached between the ground and the excited state.

$1GM = 10^{-50} cm^4 s/photon/molecule$). In the case of a pulsed laser, the average two-photon fluorescence emission efficiency is increased either by decreasing the pulsed laser repetition rate or decreasing its pulse width (given if the average intensity is the same). Many two-photon laser scanning microscopes utilize a tunable pulsed Titanium:Sapphire laser to achieve efficient two-photon cross-sections with a pulse repetition rate of 80 MHz (∼12 ns inter-pulse intervals) and pulse widths of ∼100 fs.

Principal components of a two-photon laser scanning microscope

Two-photon laser scanning systems create images from fluorescent signal with high fidelity using pulsed near-infrared light sources (**Figure 1.12**). The basic components of such a system consist of a pulsed near-infrared light source that can be tuned overa a wide wavelength range. Usually, the light source consists of a pulsed Titanium:Sapphire laser with 80 MHz repetition frequency. These mode-locked lasers are usually tunable in the range between 700 and 1050 nm and can therefore excite most fluorescent molecules efficiently. The emitted laser beam is then modulated in intensity by a Pockel's cell. To obtain an image, the laser beam is deflected through a pair of galvo-mirrors and focused through an objective to scan the specimen. A tele-

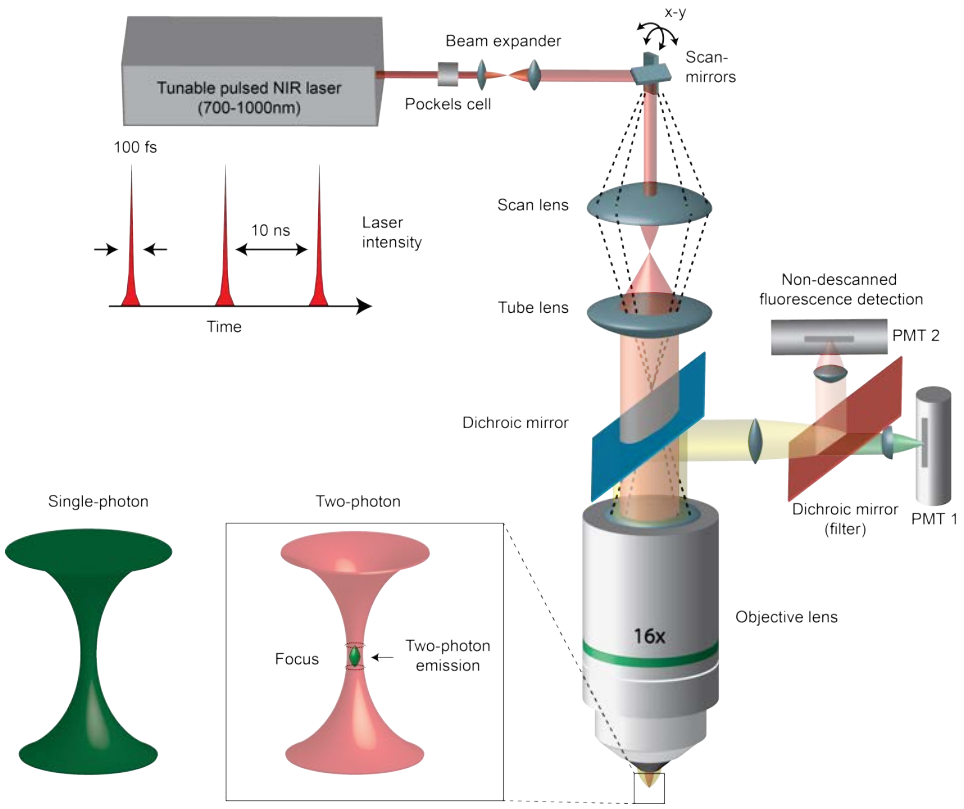

Figure 1.11: Schematic of a galvo-based two-photon laser scanning microscope: A tunable pulsed near-infrared laser is coupled into a Pockel's cell. The Pockel's cell modulates the laser power of the beam. To fully illuminate the galvo-mirror, a beam expander telescope is used. The combination of a scan lens and a tube lens projects the trajectories of the scan movement through the objective into the sample. Unlike single-photon excitation, the emission of fluorescence can only occur in the focus (see left schematics). Emission photons which are collected by the objective are then reflected by a dichroic mirror into the detection system. Photomultiplier-units (PMTs) then convert the photons into an electric signal, which is then amplified and digitized by an ADC. To detect multiple colors, arrays of dichroic mirrors and PMTs are used.

scope composed of a scan- and tube-lens relays the scanning motion of the collimated beam onto the back aperture of the objective. An image is created by scanning a sample and collecting the fluorescent signal for each focus point. To detect the weak fluorescent signal, photo-multipliers are used. The signal is then amplified and sampled by an analog-digital-converter (ADC). To achieve a tight focus, two-photon microscopes usually use high numerical aperture (NA) objectives (**Figure 1.11**, lower left). Due to the non-linear excitation process, the excitation of fluorescence is confined to the focal plane which results in an optically sectioned image. As a result fluorescent light that is detected from a focus point exclusively originates from a small region in the sample. The focused near-infrared laser beam can penetrate through living tissue

multiple hundred micrometers and create an optical section, enabling to visualize fluorescent signals excited deep in neural tissue (Helmchen and Denk, 2005).

Imaging modes in two-photon microscopy

Emitted photons in living tissue are highly scattered. During scanning, the highly focused laser beam is confined to a very small region and therefore excites a small-tissue volume (femto-liter). Even though emission photons are highly scattered, all the emitted light can be correctly assigned to the corresponding pixel in an image. Multiple approaches have been implemented to create an image with two-photon microscopes (**Figure 1.11**). A commonly used mode to

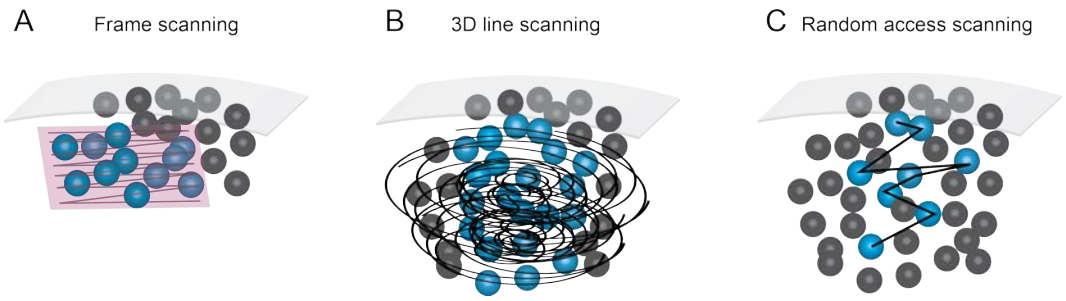

Figure 1.12: Techniques for measuring fluorescent signal with two-photon excitation: **A:** The saw-tooth raster scanning mode is commonly used in two-photon imaging. **B-C:** Microscopes can also be equipped with acousto-optic deflectors or tunable lenses or piezo-elements to perform fast 3D-spiral scans or random-access scanning of large neuronal volumes (Göbel and Helmchen, 2007; Göbel et al., 2007; Grewe et al., 2010). Parts of this illustration adapted and modified from (Göbel and Helmchen, 2007)

create an image of the specimen is the frame-scanning mode to image a field-of-view in the specimen (**Figure 1.12A**). To create such an image frame, the collimated laser beam is deflected through a saw-tooth scanning pattern. The movement of the galvo-mirrors to create such saw-tooth patterns limits the frame rate that can be achieved. In recent years, resonant scanning systems have been developed to increase imaging frame rates significantly to 30-90 Hz. These scanning systems consist of a pair of galvos, of which one resonates in a fixed frequency (Nguyen et al., 2001). At very high frame rates only very few photons reach the specimen and therefore it is crucial to reach a balance between high enough photon count per excited volume and imaging speed. The frame scanning mode is not the only possibility to create an image from a specimen. To obtain a signal from 3D volumes of tissue, 3D line scans can be applied. These scanning

patterns are achieved by incorporating a piezoelectric focusing device or a tunable lens (Göbel et al., 2007; Grewe et al., 2011).This scan method allows to obtain fluorescent signal from a large volume (**Figure 1.12B**, (Göbel et al., 2007)). Another possiblity consists of spatially deflecting the collimated laser beam using acousto-optic deflectors (Grewe et al., 2010). Acousto-optic deflectors are particularly well suited to perform random access scanning as hopping between arbitrary points in the field of view can be achieved with very short time intervals (microseconds, (**Figure 1.12C**, (Grewe et al., 2010)). All these techniques allow to study fluorescent signal dynamics with high spatial and temporal resolution in living organisms.

Measuring neural response dynamics with synthetic fluorescent calcium indicators

Two-photon laser scanning microsopy allows to visualize neural response dynamics at cellular and subcellular resolution *in vivo* as nonlinear excitation is capable of resolving fine somatic and dendritic processes deep in scattering tissue (Helmchen and Denk, 2005). The development of synthetic and genetically encoded fluorescent indicators allow to capture neural activity of confined areas of brain tissue (Svoboda and Yasuda, 2006). An indirect measure of neural activity can be obtained by visualizing changes of ion concentration after action potential firing, especially by visualizing changes in intracellular Ca^{2+} concentration with fluorescent indicators (Grienberger and Konnerth, 2012). Fluorescent calcium indicators report changes in Ca^{2+} concentration by binding free calcium ions. Upon binding of a calcium ion, conformational changes in the fluorescent molecule lead to changes in its absorption and emission properties can can be measured with laser-scanning microscopes. One such fluorescent synthetic dye is 1,2-bis(*o*-aminophenoxy)ethane-$N-N,-N',N'$-tetraacetic acid (BAPTA) (Tsien, 1980) conjugated with Oregon-Green in ester form (Oregon-green BAPTA-1 AM Ester, OGB-1 AM, (Stosiek et al., 2003; Thomas et al., 2000)). OGB-1 AM can be applied to neural tissue through pressure injection with a glass pipette in the extracellular space (**Figure 1.13A**). The ester form is cell-permeant and taken up by the cells. Esterases cleave the ester-domain rendering OGB-1 all-impermeant restricting it to the intracellular space of a neuron (including the nucleus). The

uptake of the ester form usually takes around one hour until physiologically relevant signals can be measured (**Figure 1.13B**). OGB-1 and many other small molecule synthetic dyes have been applied to measure neural activity with two-photon laser scanning microscopes as they exhibit high photo-stability, reasonable baseline fluorescence and high signal-to-noise ratios (Svoboda and Yasuda, 2006). As depicted in **Figure 1.13B**, bulk loading of a local neural population labels most neurons and glia in the vicinity of the injection site. One major limitation of this technique is the rather unspecific labeling of subpopulations of cells. For labeling and studying specific subsets of neurons, modern intersectional transgenic approaches combine the expression of a genetically encoded calcium indicator with cell type specificity enabling to study specific subsets of the neural population (Madisen et al., 2015). These transgenic tools, however, are not yet fully established for the study of developing neural tissue. One of the main reasons for not using genetically encoded indicators in young mice is that the induction of the expression of the indicators usually takes longer than the developmental time period investigated. Embryonic electroporation approaches are also not as feasible, as it is not clear which neural lineages can be targeted in a most efficient way. Based on these disadvantages, we focused our efforts on establishing two-photon calcium imaging in young mouse barrel cortex with the introduced bolus-loading technique.

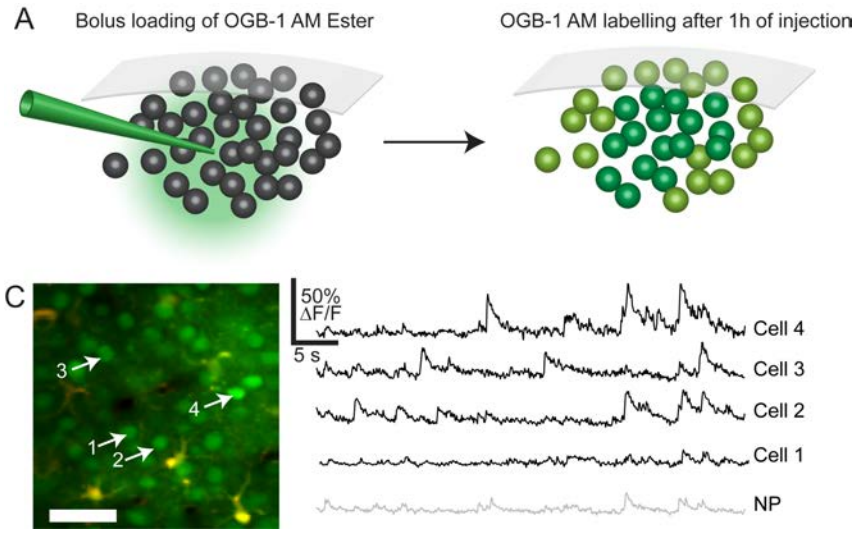

Figure 1.13: Bolus loading of synthetic calcium indicators in vivo: **A:** Bolus loading of synthetic calcium indicators is a well established way to label localized neural networks. A glass pipette is filled with the indicator (usually in calcium-free buffer solution) and slowly inserted into the tissue until it reached the target region. The indicator is then pressure-injected into the extracellular space. Neurons then take up the inactive ester-form of the indicator through diffusion. **B:** After approximely one hour, the ester form of the calcium-indicator is taken up by the cells and fluorescence signal can be measured. Depending on the quality of the pressure injection of the dye, some cells in the vicinity of the injection site might not be sufficiently loaded and only show faint fluorescence. Usually a target region of several hundred micrometers can be labelled with this technique. **C:** Maximum intensity projection of two-photon images from labeled neurons in L2/3 of mouse barrel cortex with Oregon-Green BAPTA-1 (OGB-1, green). Astrocytes are labeled with Sulforhodamine-101 (orange, (Nimmerjahn et al., 2004)). Scalebar: 30 µm. On the right of panel C, example calcium transients of four cells are shown. If a neuron exhibits an action potential, calcium concentration inside the cell increases, leading to a change in fluorescence as the synthetic indicator emits more photons when it binds calcium. These calcium transients are an indirect measure of neural activity. Transients with peak responses of around 50% correspond to strong bursts of action potential firing (see cell 4, one action-potential corresponds to around 8%). Fine dendridic and axonal processes make up the so called neuropil. The signal of the surrounding neuropil (NP) is indicated at the bottom.

1.4 Experimental approaches and specific aims of the doctoral thesis

The main focus of this thesis was to probe neural activity of sensory-evoked activity in mouse barrel cortex in a short and confined developmental time period coinciding with important changes, such as the development of active whisking and exploratory behavior. We defined a specific set of questions focusing on studying the response properties of sensory-evoked activity in anesthetized rodent somatosensory cortex between the second and fourth postnatal week. The questions in 1.4.1 are described in Chapter 2 whereas the questions raised in 1.4.2 are

addressed in Chapter 3.

1.4.1 How and when does functional sensory-evoked neuronal activity develop in mouse barrel cortex neurons?

Studies on the development of sensory coding have mostly focused on the rodent visual system as it is more feasible to present a set of stimuli to study neural coding. In addition, the time-point of eye opening and the physiological properties of adult neurons have been studied in much more detail in the rodent visual compared to the whisker somatosensory system. However, it is important to know if properties of sensory coding show similar developmental profiles in other sensory modalities like somatosensory cortex. This is relevant not only because similarities between sensory modalities can tell us something about principal sensory coding motifs, but also because the whisker system plays an important role in rodent perception, as rodents are usually nocturnal animals and rely less on visual cues. A main goal of the thesis was to characterize the changes in sensory-evoked activity at the onset of active whisking behavior which occurs around thirteen days after birth (Erzurumlu and Gaspar, 2012; Grant et al., 2012). As I have introduced in section 1.2.3, L2/3 undergoes major reorganization, including pruning of synaptic connectivity and changes in response properties during that time (Golshani et al., 2009; Wen and Barth, 2011). However, little is known about how the processing of differential whisker-evoked activity changes in this developmental time-window. A recent study found evidence for the late development of pin-wheel like tuning structures for different angular lateral deflections of a whisker in rat barrel cortex (Kremer et al., 2011). It is unclear how whisker-evoked responses induced through different touch events are encoded in barrel cortex neurons during development. We therefore asked how different whisker forces are encoded in young and adult mouse barrel cortex. Most studies focus on classical whisker deflections in the anterio-posterior direction of the animal. Nevertheless, a physiologically relevant component is also induced in the orthogonal direction through so called axial tapping which has received very little attention (Stüttgen et al., 2008). We therefore wanted to study how lateral deflections and

axial stimuli are encoded in barrel cortex, and if so, if there are neurons preferably responding to either type of stimulation. To answer this questions we performed *in vivo* silicon-probe electrophysiology in anesthetized mice to characterize response profiles across an entire cortical column of the C2 whisker. Additionally, we performed *in vivo* two-photon calcium imaging to capture the changes in response profiles of local populations of neurons in L2/3 during development. To employ the different directional stimuli, we developed a custom-built whisker stimulator capable of deflecting a single or multiple whiskers with high spatial and temporal precision (see Appendix A for a detailed documentation of the hardware and software implementation).

1.4.2 How are whisker-specific sequences of single- and multi-whisker stimuli encoded in developing barrel cortex?

Rodents rely on multi-sensory integration from ensembles of whiskers to extract features about their environment such as object texture and position (Chen et al., 2013; Pammer et al., 2013). Only in recent years encoding of multi-whisker responses have been studied, mainly in adult rat barrel cortex (Jacob et al., 2010; Ramirez et al., 2014). It seems apparent from recent work that single L2/3 neurons and L5-thick tufted neurons receive inputs from multiple whiskers showing broad receptive field properties (Ramirez et al., 2014; Clancy et al., 2015). Based on these findings we wanted to better understand how neural responses for principal and neighboring whisker stimulation are represented and integrated during development. We therefore aimed to dissect the relationship between stimulus intensity and whisker-specific detectability to characterize the neurophysiological response dynamics during development for a single barrel. Furthermore, we aimed to better understand the cross-columnar coupling of sensory-evoked activity by stimulating two neighboring whiskers with varying temporal separation. To address these questions we performed acute *in vivo* silicon probe electrophysiology in anesthetized mice while stimulating the C1 and C2 whiskers separately or simultaneously. We employed single-whisker stimuli with increasing stimulus intensity to study the whisker-specific detectability across cortical layers. We also delivered two well-timed stimuli to further

investigate the changes in temporal response integration in a barrel column as previous studies reported clear facilitation of such sensory-evoked responses in the second postnatal week (Borgdorff et al., 2007). Additionally, we performed sequential stimulation of two neighboring whiskers to study the changes in receptive field properties and cross-columnar activity during development. Specifically concerning whisker stimulation of two neighboring whiskers, multiple studies have been conducted in adult barrel cortex and found conflicting results. One set of experiments indicated that these sequential stimuli lead to clear facilitation (Erchova et al., 2003; Ghazanfar et al., 2000; Shimegi et al., 1999), while the other set reported clear surround suppression (Brumberg and Simons, 1996; Carvell and Simons, 1988; Mirabella et al., 2001). Despite these discrepancies, no study so far investigated the developmental profile of such whisker-specific receptive field properties at the onset of whisking. Therefore we aimed to investigate the responses for such stimuli during the critical developmental period of active whisking behavior, as it is a likely for receptive field maturation.

Any man could, if he were so inclined, be the sculptor of his own brain.

Santiago Ramón y Cajal

2

Layer-specific refinement of sensory coding in developing mouse barrel cortex

Alexander van der Bourg[1], Jenq-Wei Yang[1], Vicente Reyes-Puerta, Balazs Laurenczy, Martin Wieckhorst, Maik C. Stüttgen, Heiko L. Luhmann[2] and Fritjof Helmchen[2]

Cerebral Cortex, in press; [1]co-first authors, [2]co-senior authors

My contributions to this study were the following: I was responsible for and involved in conceptualization and experimental design of the study. I performed silicon probe electrophysiology as a one month collaboration project in the laboratory of Prof. Heiko Luhmann together with postdoctoral researcher Jenq-Wei Yang. I established and performed *in vivo* two-photon calcium imaging in juvenile, anesthetized mice. I wrote the first draft of the manuscript, prepared all figures and was strongly involved in data analysis.

Rodent rhythmic whisking behavior matures during a critical period around two weeks after birth. The functional adaptations of neocortical circuitry during this developmental period remain poorly understood. Here, we characterized stimulus-evoked neuronal activity across all layers of mouse barrel cortex before, during, and after the onset of whisking behavior. Employing multi-electrode recordings and two-photon calcium imaging in anesthetized mice, we tested responses to rostro-caudal whisker deflections, axial 'tapping' stimuli, and their combination from postnatal day 10 (P10) to P28. Within this period, whisker-evoked activity of neurons displayed a general decrease in layer 2/3 (L2/3) and L4, but increased in L5 and L6. Distinct alterations in neuronal response adaptation during the 2-s period of stimulation at 5 Hz accompanied these changes. Moreover, single-unit analysis revealed that response selectivity in favour of either lateral deflection or axial tapping emerges in deeper layers within the critical period around P14. For superficial layers we confirmed this finding using calcium imaging of L2/3 neurons, which also exhibited emergence of response selectivity as well as progressive sparsification and decorrelation of evoked responses around P14. Our results demonstrate layer-specific development of sensory responsiveness and response selectivity in mouse somatosensory cortex coinciding with the onset of exploratory behavior.

2.1 Introduction

Neurons in the 'barrel' subfield of rodent primary somatosensory cortex (S1) encode information about whisker movement and touch. Neurons in layer 4 (L4) of barrel cortex form cellular aggregates (the 'barrels'), which define cortical columns that are topographically related to individual whiskers on the contralateral side of the snout (Woolsey and van der Loos, 1970). Although the formation and anatomical refinement of barrel cortex organization during development has been extensively studied (Erzurumlu and Gaspar, 2012; Feldmeyer et al., 2013; Van der Loos and Woolsey, 1973), little is known about the corresponding functional changes,

especially how cortical processing of whisker-evoked activity develops at the onset of active whisking behavior.

In rodents, active whisking behavior matures during the first three postnatal weeks. More specifically, vibrissa movements transition from spontaneous unilateral muscle twitches of the whisker pad, as they occur in the first week, to regular and bilateral rhythmic whisking at the end of the third postnatal week (Arakawa and Erzurumlu, 2015; Grant et al., 2012). At around postnatal day (P) 13, cortical connectivity and excitability undergo major re-organization. Potentiation of excitatory synapses between L4 to L2/3 is followed by strengthening of local connectivity between neurons in L2/3 (Clem and Barth, 2006; Clem et al., 2008; Itami and Kimura, 2012; Wen and Barth, 2011). In rat barrel cortex, potentiation of excitatory whisker-evoked synaptic activation is detectable around P12 in L4, but only at P14 in L2/3 suggesting a critical period for L4 to L2/3 connectivity (Stern et al., 2001). In parallel to these changes in synaptic drive, intrinsic excitability of pyramidal neurons in superficial L2/3 markedly decreases (Borgdorff et al., 2007; Maravall et al., 2004), while synapse density increases (Chandrasekaran et al., 2015) around P13. These changes in intrinsic excitability and synaptic connectivity are also reflected by a switch of spontaneous activity from highly correlated bursts of action potential firing (Khazipov and Luhmann, 2006; Yang et al., 2009) to desynchronized and sparse activity (Golshani et al., 2009). Similar results have been described for postnatal development of other sensory cortices like mouse visual cortex where direction selectivity does not require visual experience and is present before eye opening (Hagihara et al., 2015; Rochefort et al., 2009, 2011). However, it is largely unknown how processing of tactile stimuli with different directional forces develops across the neocortical layers in the maturing barrel cortex during this critical period.

Whisker forces and kinematics convey important information for rodent perception (Chen et al., 2013; Gopal and Hartmann, 2007). Most studies on barrel cortex use controlled lateral deflections of single or multiple whiskers. Such lateral deflections for example occur when animals have to discriminate the width of an aperture (Krupa et al., 2001). The development

of direction selectivity to lateral whisker deflections with varying stimulation angles has been reported to develop in the fourth postnatal week in rat barrel cortex (Kremer et al., 2011). However, a major behaviorally relevant whisker force component is induced by whisker bending, which exerts an axial force on the whisker follicle. Such axial whisker movements evoke strong responses in the trigeminal ganglion (Stüttgen et al., 2008) and are important for perception of object location (Pammer et al., 2013). How neurons in developing barrel cortex respond to axial or lateral whisker forces and how these response profiles relate to the development of exploratory whisking behavior have so far remain unexplored. We therefore aimed to investigate the maturation of sensory responses to distinct mechanical forces on the whisker follicle (laterally and axially, as they occur during brushing and tapping of objects; Quist et al. (2014)) before, during and after the onset of active whisking.

Using a novel whisker stimulator for both lateral and axial stimulation, we here examined how responses to these distinct stimuli of barrel cortex neurons change during the critical phase of postnatal development. We find that sensory-evoked activity matures in a layer-specific manner in a narrow time window around P13, at the onset of active locomotion and whisking. Stimulus-evoked activity in supragranular and granular layers generally decreases at this developmental stage whereas neurons in infragranular layers show increased responsiveness. We also demonstrate that during the same period neurons develop a higher selectivity for lateral or axial whisker forces, especially in L2/3. Together, these findings reveal substantial refinements of whisker-evoked activity in barrel cortex coinciding with the onset of explorative whisking behavior.

2.2 Materials and Methods

Animal experiments were approved by the Cantonal Veterinary Office Zurich and the local German ethics committee (#23177-07/G10-1-010), respectively. Experiments followed the European, German (European Communities Council Directive, 86/ 609/ECC) and Swiss national regulations.

2.2.1 Behavior Monitoring

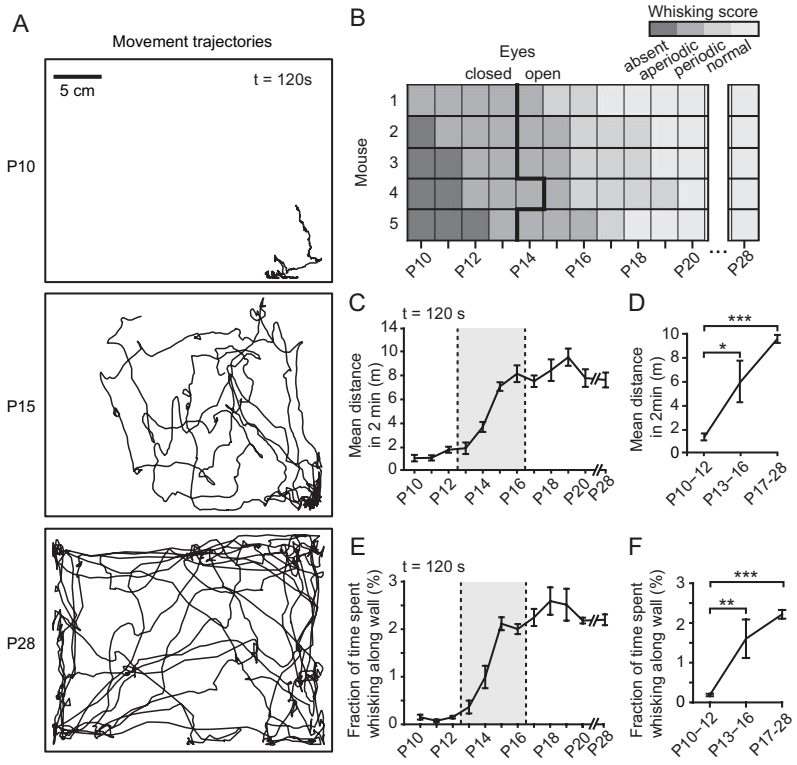

Figure 2.1: Postnatal development of explorative behavior in mice.: (A) Movement trajectories in an open field arena, measured over two minutes for one example mouse at age P10, P15 and P28. (B) Quantification of whisking behavior of a litter of five mice from P10-28. Whisking was classified as absent (no whisking), aperiodic (small, aperiodic whisker movements), periodic (low amplitude whisking at 2-5 Hz) and normal (larger amplitude whisking at 5-15 Hz). Whisking classes are depicted as different gray levels. Time of eye opening is indicated by the thick line. (C) Quantification of the mean distance travelled during a 2-min observation time across days. Largest changes occurred in the P13-16 age group (gray box). (D) Pooled analysis of the mean distance travelled for the three age groups defined in C (p=0.02 for P10-12 vs P13-16; p=0.001 for P10-12 vs. P17-28). (E) Quantification of time spent whisking along the walls of the arena during a 2-min observation time across days. (F) Pooled analysis of the fraction of time spent whisking along walls for the three age groups (p=0.0085 for P10-12 vs P13-16; p=0.0003 for P10-12 vs. P17-28). Data points are mean $\pm$ s.e.m. (n=5 mice). Statistics: Kruskal-Wallis test followed by Dunn-Sidak's post-hoc correction (* p<0.05, ** p<0.01, *** p<0.001).

Five C57BL/6 mice (3 males and 2 females of the same litter) were placed two times per day (2 min sessions) in a 75x60 cm^2 enclosed arena to assess locomotion and whisking behavior in darkness between P10 and P28 (Fig. 1 and Supplementary Movie 1). Movement trajectories were recorded at 15 frames per second (fps) at 1280x1024 pixels (LUMENERA Lw 570, Lumenera Coorp., ON, USA). The light-proof arena was illuminated by an infrared light emitting diode (LED) light source (730 nm, M730L4, Thorlabs Inc., USA). We traced move-

ment trajectories semi-automatically with custom-written routines in MATLAB. Movement was scored as 'whisking along walls' if (1) the mouse moved in close proximity to the arena wall while the whiskers touched the wall (head center distance to wall $\leqslant$ 3 cm) and (2) the animal was not at rest during wall touches. Whisking behavior was monitored for five minutes and assessed by a scoring scheme for active whisking (Landers and Philip Zeigler, 2006).

2.2.2 Animal Surgery and Preparation

We used 18 C57BL/6 mice (9 males and 9 females) at ages ranging from P10 to P28 for multi-electrode recordings, and 18 C57BL/6 mice (10 males and 8 females) for two-photon calcium imaging. Mice were sedated with chlorprothixene (0.1g/kg, intraperitoneal (i.p.); Sigma-Aldrich Chemie GmbH, Buchs, Switzerland) and lightly anesthetized with urethane (0.25–0.5g/kg, i.p.). Atropine (0.3 mg/kg; Sigma-Aldrich Chemie GmbH, Buchs, Switzerland) and dexamethasone (2 mg/kg; aniMedica GmbH, Senden-Bösensell, Germany) were administered subcutaneously (s.c.) to reduce secretion of saliva and to prevent edema (s.c. injection 30 min after induction of anesthesia). The body temperature was maintained at 37° C with a heating blanket. Hydration levels were checked regularly and maintained by s.c. injections of Ringer-lactate (Fresenius Freeflex; Fresenius Kabi AG, Oberdorf, Switzerland). The depth of anesthesia was evaluated throughout the experiment by testing the pinch reflex on the forepaw. A custom-built head plate was glued to the skull over the left brain hemisphere with dental cement (Paladur, Heraeus Kulzer GmbH Hanau, Germany; Caulk Grip Cement for electrophysiology) to secure and stabilize the animal. A small cranial window of 1.5x1.5 mm^2 was opened above the center of the mapped barrel columns with a sharp razor blade and superfused with Ringer's solution (in mM: 145 NaCl, 5.4 KCl, 10 HEPES, 1 $MgCl_2$, 1.8 $CaCl_2$; pH 7.2 adjusted with NaOH). Care was taken not to damage the dura or surface blood vessels in young animals (P10-P20). In animals older than P20, we removed the dura to prevent blockage of the glass pipette tip during insertion into the cortex for two-photon guided calcium indicator loading. For multi-electrode recordings, the dura was penetrated and the cranial window sealed with agarose (type III-A, 1% in Ringer; Sigma).

2.2.3 Intrinsic optical imaging

The principal whisker-related barrel column was identified using optical imaging of intrinsic signals. The cortical surface was visualized through the intact bone by surface application of normal Ringer's solution and a glass coverslip placed on top. The skull surface above the barrel cortex was left intact for animals younger than P20, but thinned in older animals. Reference images of the cortical blood vessel pattern were visualized by a 546-nm LED to enhance contrast. Functional maps of the target barrel columns C1 and C2 were obtained by shining red light (630 nm LED) on the cortical surface while stimulating the C1 or C2 whisker with a piezoelectric element (10 Hz at 2° amplitude in rostrocaudal direction). Reflectance images were collected through a 4x objective with a CCD camera (Toshiba TELI CS3960DCL; 12-bit; 3-pixel binning, 427x347 binned pixels, 8.6 μm pixel size, 10 fps). Functional intrinsic signal images were computed as fractional reflectance changes relative to the pre-stimulus average (average of 30 trials). The intrinsic signal images obtained for the C1 or C2 barrel columns were then mapped to the blood vessel reference image and used to guide the location of the craniotomy.

2.2.4 Histology

After each experiment, the animal was deeply anesthetized with ketamine (120 mg/kg, ketamine, 50 mg/mL, Hameln Pharma, Hameln Germany) and xylazine (5 mg/kg, Rompun 2%, Bayer, Leverkusen, Germany) and perfused through the aorta with 0.2M phosphate-buffered saline (PBS) for washing. The brain was carefully removed from the skull and kept in 4% paraformaldehyde for 24 hours at 4°C. After 24 hours, the brain was washed with 0.1 M PBS and stored in 30% sucrose (in PBS) overnight. After washing with PBS, brains were sectioned in 200-μm thick tangential sections and prepared for cytochrome-oxidase (COX) immunohistochemistry. Sections were rinsed in PBS and incubated at 39ºC in a solution of 0.6 mg cytochrome c, 0.5 mg DAB, and 44 mg sucrose per ml, with 0.3% catalase included. Sufficient staining of barrels was achieved after 2-7 h of reaction. After COX immunohistochemistry, sec-

tions were intensified with 0.5% copper(II)sulfate (Sigma) for 2-3 min, air dried, and mounted. All chemicals were obtained from Sigma (Deissenhofen, Germany).

2.2.5 Galvanometer-driven whisker stimulator

We applied whisker stimulation with a novel galvanometer -driven stimulation system, consisting of two thin (200-µm diameter) optical fibers attached to the whisker, one for each stimulation axis (**Figure 2.2** and **Supplementary Movie 2**). Both fibers were glued together near their tips with 3M Scotch Weld repositionable glue and the whisker was attached in its resting position to one optical fiber tip with a droplet of glue. Stimulation fibers were visually guided towards the whisker's resting position under a stereoscope with a micromanipulator. We kept the attachment position relative to the snout constant for all experiments (1 cm from follicle for both axial and lateral stimulation fiber). For each fiber, translation was controlled by a galvanometer (SpaceLas ILDA30kpps galvanomet-

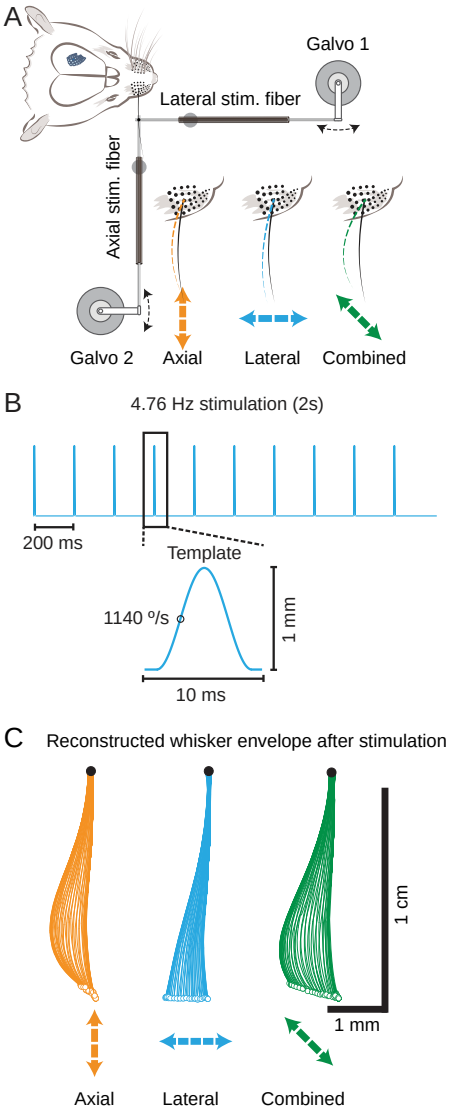

Figure 2.2: Galvanometer-driven whisker stimulation: (A) Axial and lateral whisker stimulation using a pair of optical fibers, each controlled by a galvanometric unit. The fiber tips were attached to the whisker at 1cm distance from the skin with repositionable glue. Fibers were attached in orthogonal directions to induce axial, lateral or combined movement of the whiskers. All other whiskers were trimmed to avoid contact with the stimulation fibers. (B) For stimulation, we used a phase-shifted 100 Hz cosine template waveform presented at 4.76 Hz repetition rate with 200 ms inter-stimulus intervals. (C) Stimulus-induced whisker trajectory after one axial, lateral or combined stimulation pulse reconstructed from high-speed videography in vivo. Note that the horizontal and vertical axes are scaled 2:1 for visualization of the stimulus-induced whisker envelopes.

ric system kit, Topic Light Co., Ltd, Guangdong, China). The rotational movement of the galvanometer was transformed into a translational movement by attaching the backend of the optical fiber to a small pole arm fixed on the galvanometer axis. Each optical fiber was embedded in a low friction heat resistant capillary tube (Polymicro, inner diameter: 251 µm, outer diameter: 355 µm Molex, USA). A mounting point for each axis close to the stimulation site suppressed movement and vibrations of the outer fibers. We used this two-axis stimulator to mechanically deflect a single whisker in the rostrocaudal and mediolateral direction, respectively, thereby inducing whisker forces laterally and/or axially to the follicle base. Axial and lateral whisker movements were induced simultaneously or independently at high temporal and spatial resolution. The stimulation pulse consisted of a phase-shifted 100 Hz cosine, which was presented at a repetition rate of 4.76 Hz for two seconds (pulse amplitude: 1 mm; pulse duration 10 ms, inter-stimulus interval: 200 ms, resulting in $1140°/s$ maximum speed). Galvanometers were driven by generating analog output signals (5000 samples per second) through a NI PCIE-6323 card and controlled by custom-written LabVIEW software. During the experiment, we monitored consistent stimulation output from live feedback of the galvanometer positioning. Each stimulus type was presented 20 times, as random sequence of blocks of five stimuli, with each stimulus separated by an 8-s blank time (no stimulation). Stimulator performance was evaluated by imaging fiber-tip movements at high speed (5000 fps, Basler A504k, Basler Vision Technologies, Ahrensburg, Germany) and analyzing the fiber-tip trajectory horizontally and vertically. Custom-written software was used to semi-automatically measure the translational movement of each fiber for a given trial. Deviation of the translational movement from the template stimulus for each measured data point was below 100 µm. Movement trajectories of the C2 whisker were tracked with the Whisk tracking software (Clack et al., 2012) from high-speed image sequences (3000 fps). The extracted whisker envelope was low-pass filtered (5-point sliding average).

2.2.6 In Vivo High-Density Multi-electrode Recordings

Neural activity was recorded with an 80-channel *silicon-probe* inserted perpendicularly into barrel cortex (NeuroNexus Technologies, Ann Arbor, MI, USA). Each of the four shanks (3 mm long) contained 20 recording sites (413 μm^2 surface area per recording site) spaced 50 µm apart. Distance between shanks was 150 µm. Insertion of the probe was guided by intrinsic optical imaging. For each animal, the probe insertion points were marked by impregnating the probes with DiI (1, 1-dioctadecyl-3, 3, 33-tetramethyl indocarbocyanine, Molecular Probes, Eugene, OR, USA) before insertion. A silver wire placed over the cerebellum served as a ground electrode. All data were continuously digitized at 20 kHz and stored for offline analysis using a 256-channel extracellular recording system and MC_RACK software (Multi Channel Systems, Reutlingen, Germany). The total duration of multi-electrode recordings varied between 3 and 5 hours.

2.2.7 In Vivo Two-Photon Calcium Imaging

Neuronal ensembles in superficial layers of the principal whisker barrel field mapped by intrinsic signal imaging were bolus-loaded with the AM ester form of Oregon Green BAPTA-1 by pressure injection (OGB-1; 1 mM solution in calcium-free Ringer's solution; 2-min injection at 150-200 µm depth) as described previously (Stosiek et al., 2003). Astrocytes were labeled by surface application of 100 µM Sulforhodamine-101 (5 min incubation time followed by washing of surface area with Ringer's solution (Nimmerjahn et al., 2004). The craniotomy was then filled with agarose (type III-A, 1% in Ringer's solution; Sigma) and covered with an immobilized glass plate. Two-photon calcium imaging was performed with a custom-built two-photon laser-scanning microscope one hour after bolus loading. In vivo imaging was performed with a Ti:sapphire laser system at 840 nm excitation (Mai Tai Deep See; approx. 120 femtosecond laser pulses). Fluorescence images of 100x100 pixels at 10 Hz were collected with a 16x water-immersion objective lens (Nikon, NA 0.8). Data acquisition was controlled by HelioScan (Langer et al., 2013). Duration of calcium imaging recordings varied between 3 to 4 hours.

2.2.8 Electrophsiology Analysis

Analysis of Local Field Potential Adaptation by Discrete Fourier Transformation

Local field potential (LFP) traces were first corrected for variations in baseline voltage levels by applying a detrending polynomial fit after low-pass filtering (1-300 Hz) of the continuously digitized recorded data. Next, the LFP response after the first stimulation pulse was used to generate a simulated LFP trace consisting of 10 subsequent whisker-evoked LFP signals. A discrete fast Fourier transform was applied to the simulated and measured LFP data. Ratios of the peaks at the stimulation frequency were calculated as adaptation ratio indices as a measure of response adaptation (Katz et al., 2006).

Current-Source Density Maps

We assessed the cortical depth of individual multi-electrode recordings from stereotaxically estimated depth of insertion as well as vertical current-source density maps (CSD) computed from LFP profiles. The early CSD sinks present after sensory stimulation at the thalamo-recipient L4 and the border between L5 and L6 were used to assign individual channels to specific cortical layers (Mitzdorf, 1985). To this end, CSD maps were computed by using the average LFPs of up to 20 trials as described previously (Nicholson and Freeman, 1975; Reyes-Puerta et al., 2015b). The computed data where then interpolated and visualized as pseudocolor images, with current sources and sinks represented by red (positive) and blue (negative) colors, respectively.

Spike Detection and Sorting

Multi-channel based spike detection and sorting was performed as described previously (Reyes-Puerta et al., 2015b). After high-pass filtering (0.8-5 kHz) of the continuously digitized recorded data, non-overlapping groups of two to four recording sites were defined as "virtual tetrodes" and processed separately (Harris et al., 2000; Einevoll et al., 2012). Spike detection was performed in each group independently and separately using amplitude-thresholding in the negative range (-7.5 times the standard deviation of the signal; (Gray et al., 1995)). Upon threshold cross-

ing on either of the cannels within a group, all sampled amplitude values for all channels in a time range of -0.5 to +0.5 ms relative to the waveform negative peak were extracted. These spike waveforms were then used to compute feature vectors, each containing the negative peak amplitude and two first principal components derived from the waveforms. The feature vectors were then used to perform spike sorting (Harris et al., 2000; Hazan et al., 2006). We established several criteria in order to ensure the isolation quality of the sorted neurons, accounting for (1) a clear refractory period existing in the overall activity of the isolated units, (2) a stable spontaneous firing rate during the whole recording period, and (3) a valid *isolation distance* obtained in the spike sorting procedure (for further details see Reyes-Puerta et al. (2015b)). Cells were subsequently classified as putative excitatory (EXC) pyramidal neurons and putative inhibitory (INH) interneurons based on their mean spike waveform. For each neuron two parameters were calculated, which have been shown to reliably separate between the two identified neuronal populations in adult rodents in vivo (Guo et al., 2014; Reyes-Puerta et al., 2015b): (1) the onset to (late) peak latency, and (2) the asymmetry index. This procedure was successful in separating between two neuronal classes in the P17–P28 age group. However, no separation could be obtained in any of the younger age groups (P10–P12 and P13–P16), in which no INH neuron clusters could be reliably separated. These data are in agreement with the finding that different types of fast spiking INH neurons show only fully matured spike waveform profiles from P15 onwards (Doischer et al., 2008). Spike trains were represented as spike rasters and peristimulus time histograms (PSTHs) using 1-ms time bins for MUA data and 10-ms time bins for SUA data. For each pulse during the 2-s stimulation, sensory-evoked responses were evaluated by quantifying spike counts within the first 50 ms after pulse onset ('early' time window) and within a 50-150 ms time window ('late' response). Average firing rates were represented by mean ± s.e.m. of 20 trials. Baseline activity was calculated as the average spike rate 100 ms before presenting the 10 successive pulses. The slope of the decay of the mean sensory-evoked MUA responses 100-200 ms after each stimulation pulse was obtained by a linear regression fit. Data analysis of spike trains was performed in MATLAB.

Detection of Sensory-Evoked Response Latencies

Response latencies after whisker stimulation were computed for different layers from smoothed MUA recordings from a specific recording site closest to the identified layer (convolution of a Gaussian window filter, 5 ms). First, the peak MUA response was identified in a 50 ms window after stimulation. Second, the mean base response 100 ms before stimulation was calculated. Response onset was identified if (1) the response was bigger or equal to the mean base response and smaller than 3 standard deviations of the peak response. Onset detection was also performed on spike-sorted data by detection of the first spike occurring in each of the 20 trials in a 50 ms window after stimulation. Both, the detected MUA and SU response latencies showed similar response latencies.

Assignment of Recording Sites to Cortical Layers

Differences in cortical thickness across developmental age groups were normalized by choosing a fixed number of recording sites per cortical layer (not exceeding layer thickness in the P10-12 age group). Recording sites fully embedded in the corresponding layers, as revealed by the CSD maps, were used as reference points to annotate additional recording sites. The number of recording sites per animal was kept constant for all layers and age groups (L2/3: 1; L4: 2; L5: 2; L6:2).

2.2.9 Analysis of Calcium Imaging Data

Calcium imaging data were imported and analyzed using routines custom-written in NIH ImageJ and MATLAB. First, fluorescence image time-series for a given region were concatenated. The concatenated imaging data was then aligned using TurboReg to correct for small x-y drift (alignment on SR-101 channel, transferred to OGB-1 images, NIH ImageJ; Thévenaz et al. (1998)). As a next step, background was subtracted as the bottom 1st percentile fluorescence signal of the entire image. Average intensity projections of the imaging data were used as reference images to manually annotate regions of interest (ROIs) corresponding to individual neurons. Neurons with somata partly out-of-focus were not included. Calcium signals were

expressed as the mean pixel value of the relative fluorescence change $\Delta F/F = (F - F_0)/F_0$ in a given ROI. F_0 was calculated as the bottom 10th percentile of the fluorescence trace. The neuropil signal was defined by all pixels not assigned to a neuronal soma or astrocyte of the overall ROI annotation. Active neurons were identified by two-way ANOVA of the evoked neuropil and neuronal signal (significance value p<0.05). Stimulus-responsive neurons were identified by two-way ANOVA of pre- and post-stimulus time periods (significance value p<0.05). For each stimulus the evoked responses of 20 trials were analyzed and the response magnitude expressed as the mean of the evoked $\Delta F/F$ integral ($\% \cdot s$; integral of response for the 2-s stimulation window). This metric compensates for possible differences in calcium transient dynamics and cellular calcium buffering in different age groups and animals. Pearson's correlation coefficients of spontaneous and sensory-evoked responses for two neurons at zero lag were calculated between pairs of somatic calcium traces (60 s spontaneous data; mean of 20 x 2 seconds evoked data). Regression lines fitted to scatter distributions of different age groups were compared for statistical difference by performing a two-tailed t-test. Two regression lines were considered to be significantly different if the student's t-distribution functions of the underlying scatter distribution pairs were significantly different.

2.2.10 Analysis of Response Selectivity

For each single unit, the response selectivity index was defined as the area under the Receiver-Operator Characteristics curve (auROC) based on the average firing rate during the initial 50 ms after each stimulation pulse for 20 trials per stimulus type. Differences in response selectivity distributions were analyzed using the non-parametric Kolmogorov-Smirnov test where each empirical function was represented as the cumulative distribution of auROC across age groups. For the in vivo two-photon calcium imaging data, auROC was calculated for each ROI using the means of the evoked $\Delta F/F$ integral (in $\% \cdot s$ units) for preferred (μ_p) or non-preferred (μ_{np}) stimulus with the preferred stimulus defined by the larger mean $\Delta F/F$ integral for either axial or lateral stimulation ($\mu_p > \mu_{np}$). This approach results in auROC values ranging from 0.5 (no selectivity) to 1.0 (perfect selectivity for preferred stimulus).

2.2.11 Statistical Analysis

Data are represented as mean ± s.e.m. unless stated otherwise. One- or two-way ANOVA was used to test for significance for normally distributed data, followed by post-hoc Tukey's test. The Kruskal-Wallis test was used for non-normally distributed data, followed by Dunn-Sidak's post-hoc test. Significance threshold was set to $p<0.05$; in the figures, different degrees of evidence against the null hypothesis are indicated by asterisks ($p<0.05$: *; $p<0.01$: **; $p<0.001$: ***).

2.3 Results

2.3.1 Onset of Locomotion and Whisking Behavior in the Third Postnatal Week

We first identified the developmental period during which mice show prominent behavioral changes related to processing of whisker information. We analyzed explorative behavior in an open field test between P10 and P28 (**Figure 2.1A** and **Supplementary Movie 1**). Before P13, mice were rather immobile and showed minimal active whisking. Around P14, shortly after eye opening, mice began to exhibit rhythmic active whisking and displayed a significant increase in travel distance **Figure 2.1B-D**. In parallel, the fraction of time spent actively whisking against the wall increased (**Figure 2.1E, F**). This marked behavioral change occurred within a short time window between P13 and P16, coinciding with the critical developmental period of L2/3 in barrel cortex (Stern et al., 2001), with little changes thereafter. Similar results have been previously reported for both rats (Landers and Philip Zeigler, 2006; Grant et al., 2012) and mice (Arakawa and Erzurumlu, 2015). Importantly, enhanced whisking activity and a higher incidence of touches will result in a net increase of both lateral and axial forces impinging on the whisker follicle and, thus, the tactile receptors (Ebara et al., 2002). These changes in experience likely are associated with changes in cortical processing of whisker stimuli. We therefore aimed to analyze sensory-evoked activity in barrel cortex using controlled whisker stimulation across

three age groups: before eye opening and whisking onset (P10-P12), during the critical period (P13-P16), and afterwards (P17-P28).

2.3.2 A Novel Galvanometer-Driven Stimulator for Precise Whisker Control

To apply axial and lateral forces independently or in combination to an individual whisker, we developed a galvanometer-driven stimulator. The stimulator consists of two optical fibers orthogonally glued together near their tips, attaching them to a single whisker (**Figure 2.2A**; see also Materials and Methods, Supplementary Data and **Supplementary Figure 2.11**). Our stimulation protocol consisted of 10 successive single-whisker stimuli delivered at 4.76 Hz (**Figure 2.2B**; 10-ms stimulus waveform plus 200-ms inter-stimulus interval, 1 mm amplitude at 10 mm distance from the snout; deflections applied axially, laterally, or in combination). Axial forces pushed the whisker into the follicle whereas lateral forces deflected the whisker in the anterior-posterior direction (**Figure 2.2C**), similar to standard whisker deflection experiments using piezoelectric devices (Simons, 1983). Induced whisker movements displayed high spatial and temporal precision with little deviation from the desired waveform across all age groups and negligible after-oscillations (**Supplementary Figure 2.11** and **Supplementary Movie 2**). This stimulator enabled us to study the developmental profile of sensory-evoked neuronal responses as well as their selectivity for axial or lateral stimulation, using in vivo multi-electrode recordings and two-photon calcium imaging in lightly urethane-anesthetized mice.

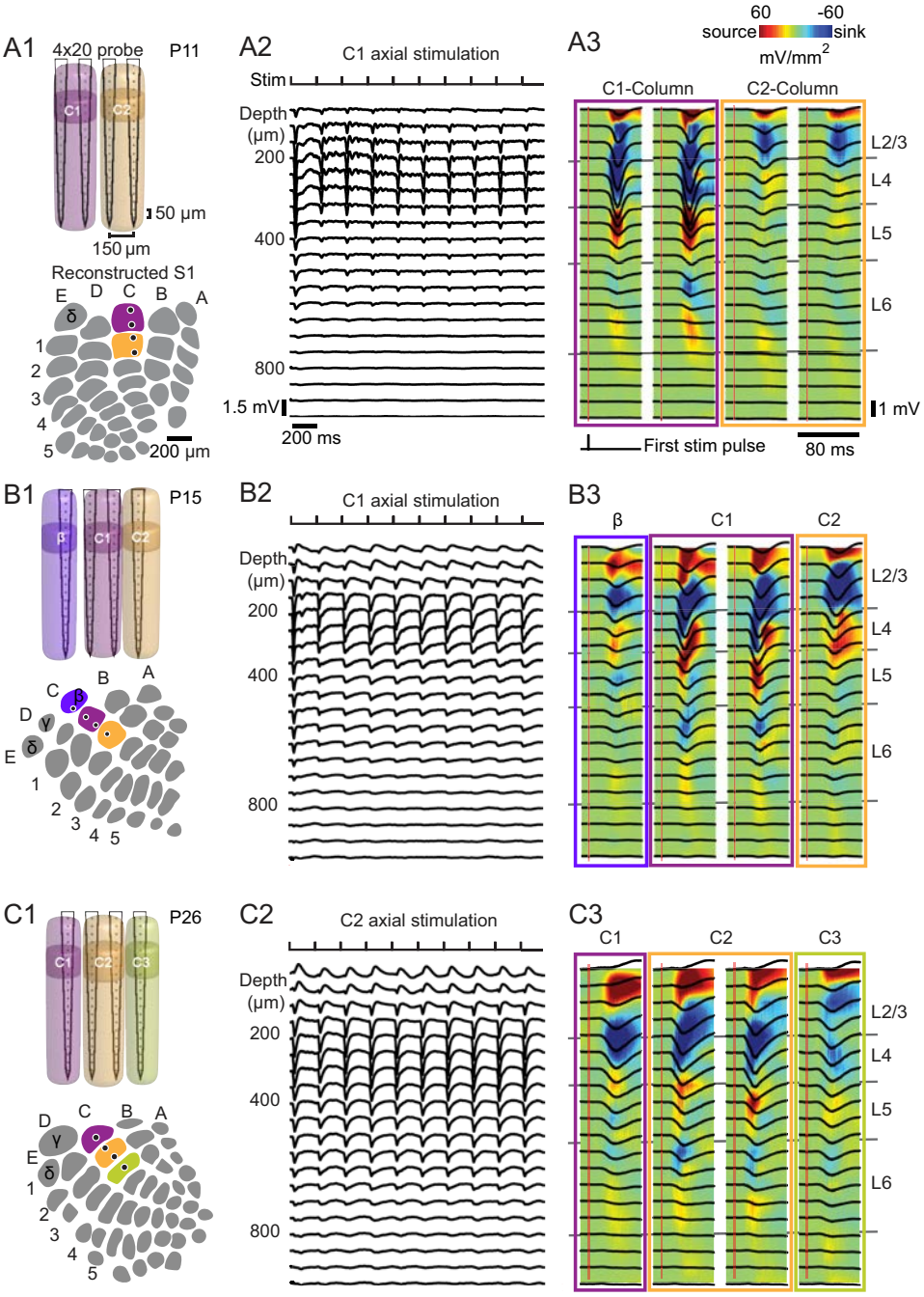

Figure 2.3: Multi-electrode array recordings of single-whisker evoked cortical activity: (A) Example recording of a P11 mouse. (A1) Schematic of multi-electrode array placement. For all animals, the array was inserted perpendicular to the C1 and C2 barrel columns (with small variations in relation to the barrel field). (A2) LFPs evoked by axial whisker stimulation (average of 20 trials). (A3) CSD maps computed from the first stimulation pulse of the 4.76 Hz stimulation (average of 20 trials). Sinks are indicated by blue and sources by red colors. Borders of cortical layers were identified from the CSD maps and stimulus onset times, indicated as gray traces in the background. Vertical red lines indicate stimulus onset. (B) and (C) Examples of multi-electrode array position, LFPs and CSD maps in a P15 and P26 mouse, respectively (same conventions as in A).

2.3.3 Layer-Specific Intra-Columnar Development of Whisker-Evoked Activity

We first asked whether the representation of whisker stimuli changes across cortical layers in the three defined age groups. We used 80-channel multi-electrode arrays (4 shanks spaced 150 µm apart; 20 linearly arranged electrodes per shank, 50 µm inter-electrode distance) and measured local field potentials (LFPs), multi-unit activity (MUA) and single-unit activity (SUA) in identified barrel columns across all cortical layers (**Figure 2.3**). Electrodes were covered with DiI and for each experiment we identified the exact electrode position by visualizing the DiI traces of the shank insertion points (see also **Supplementary Figure 2.10**). We calculated current-source density (CSD) maps from the LFPs to assign recording electrodes to individual barrel-related columns and cortical layers (**Figure 2.3**). At all ages, L4 could be identified by the prominent current sinks occurring shortly after whisker stimulation (response onset latency for P10-12: 20.3 ± 0.3 ms; P13-16: 17.1 ± 0.3 ms; P17-28: 15.3 ± 0.4 ms; mean ± s.e.m., n = 6 mice per age group). In agreement with previous work (Mitzdorf, 1985; Reyes-Puerta et al., 2015b), activity subsequently propagated towards L2/3 as indicated by slightly longer onset latencies in L2/3 (P10-12: 22.2 ± 0.3 ms; P13-16: 19.0 ± 0.3 ms; P17-28: 16.5 ± 0.3 ms; n = 6 mice per age group). We could thus reliably identify cortical layers in the recorded barrel columns at different developmental time points. In animals younger than P12, sensory-evoked LFP responses were mainly confined to L2/3 and L4 of the barrel column corresponding to the stimulated whisker (**Figure 2.3A**, typical example of a P11 animal). Only small-amplitude LFP responses were apparent in L5 and L6 (with an early CSD sink in upper L6), which strongly adapted following the first stimulus. In contrast, older animals displayed larger-amplitude LFP responses with little adaptation also in deeper layers (**Figure 2.3C**; representative example of a P26 animal from the P17-28 age group). These changes in adaptation of LFP responses were significant across age groups (**Supplementary Figure 2.12**).

We further examined layer-specific developmental changes of sensory-evoked responses by analyzing MUA across cortical layers (**Figure 2.4**). Mean evoked spike rates significantly de-

creased with age in L2/3 and L4 but increased in L5 and L6 (**Figure 2.4A,B**). Interestingly, spontaneous spiking activity showed a similar developmental increase in the deeper layers (**Supplementary Figure 2.13**). To quantify changes in response adaptation across development, we compared the ratio of response integrals for the last versus the first stimulation pulse. In addition, we subdivided the MUA profiles into an early (0-50 ms) and a late (50-150 ms) response window after the respective stimulation pulses. In L2/3 and L4, early MUA response ratios were above 100% in young animals (indicating facilitation) and then significantly decreased with age (**Figure 2.4C**). In contrast, neurons in L5 displayed response ratios below 100% in the youngest age group (indicating adaptation), which then increased with age. Thus, at a stimulation frequency of $\sim$5 Hz early-evoked spiking activity in lightly anesthetized mice effectively converges in all layers towards little adaptation in the postnatal development period investigated here. Distinct developmental profiles for superficial vs. deeper layers were also observed for the response ratios of spiking integrals in the late temporal window (50-150 ms), which relate to evoked circuit reverberations. Whereas late response ratios significantly decreased in L2/3 and L4 during postnatal development, they increased in L5 and L6 (**Figure 2.4D**). We obtained similar results for lateral whisker stimulation (**Supplementary Figure 2.14**). We further analyzed the kinetics of the sensory-evoked late response component by fitting a line to it. The slope of this line became significantly more negative in all layers except L6 between P10-12 vs. P17-28 age groups (L2/3: -71.8 $\pm$ 43.5 vs -300.1 $\pm$51.1, p=0.008; L4: -63.9$\pm$91 vs -487.4$\pm$106.6, p=0.012; L5: -148.8 $\pm$ 35.5 vs -424.1 $\pm$ 82.4, p=0.004; L6: -132.8 $\pm$ 23.3 vs -285.5 $\pm$ 50.5, p=0.08; units of spikes/s^2). In general, axial or lateral whisker stimulation showed similar response profiles at the MUA level. Together, these findings demonstrate that both sensory-driven cortical activation patterns and the resulting spiking activity undergo in parallel prominent and layer-specific changes at the onset of explorative locomotion behavior during the third postnatal week.

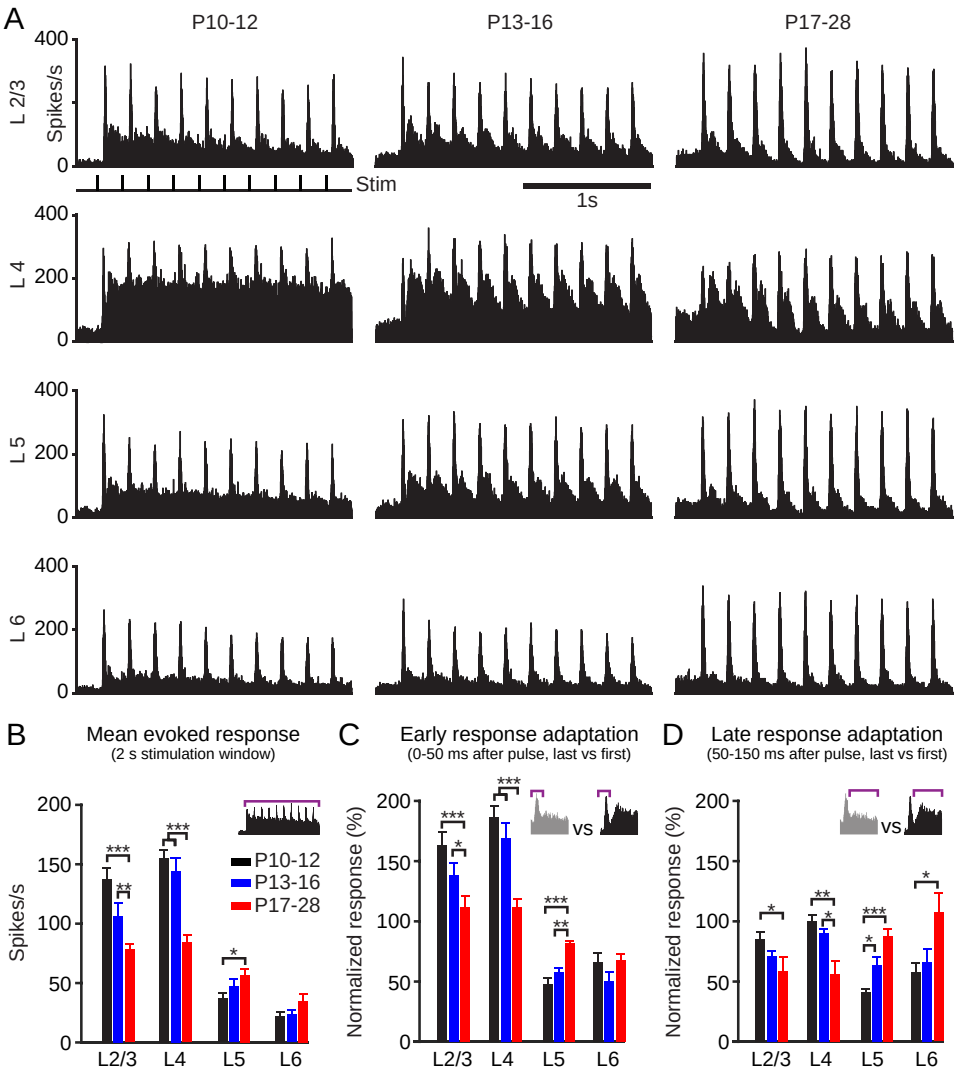

Figure 2.4: Intra-columnar development of sensory-evoked activity: (A) Pooled average MUA across cortical layers and age groups (examples show responses to axial stimulation, see also **Supplementary Figure 2.14** for lateral responses). For each animal, we selected four representative electrodes corresponding to superficial L2/3 and the centers of L4, L5 and L6 for the analysis. (B) Pooled analysis of the mean evoked response (2 s) for all cortical layers and age groups. (C) Quantification of early response adaptation (spike counts 0-50 ms after stimulation pulse). Normalized responses indicate the ratio for the last vs. first stimulation pulse. (D) Quantification of late response adaptation (normalized spike count in 50-150 ms window for last vs. first stimulation pulse). Data points are mean $\pm$ s.e.m. (n = 18 mice, 6 mice per age group). Statistics: Kruskal-Wallis test followed by Dunn-Sidak's post-hoc correction (* $p<0.05$, ** $p<0.01$, *** $p<0.001$).

2.3.4 Layer-Specific Cross-Columnar Development of Whisker-Evoked Activity

We further studied the development of lateral spread of activity across neighboring barrel columns. We compared sensory-evoked MUA in the principal whisker-column with its neighboring column (**Figure 2.5A**). Mean spike rates in L2/3 and L4 of the neighboring column, when normalized to the principal column, significantly increased with age for both axial (**Figure 2.5B**) and lateral (**Figure 2.5C**) stimuli. No clear change was found in L5 and L6, although a non-significant similar trend was visible. We conclude that during postnatal maturation, in addition to an intra-columnar layer-specific refinement, cross-columnar spread of whisker-evoked activity becomes larger, especially in L2/3 and L4.

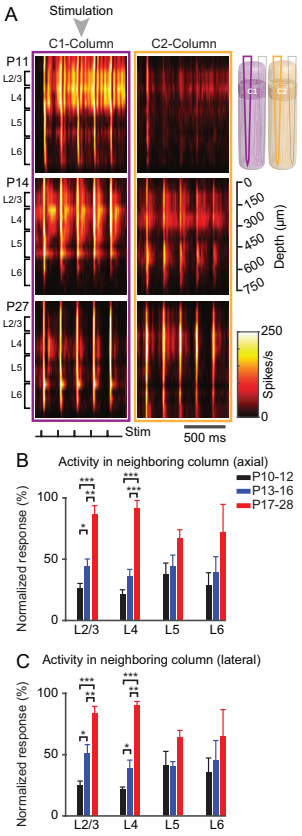

Figure 2.5: Cross-columnar development of sensory-evoked activity. : (A) Heatmap showing MUA in the principal (C1) and neighboring (C2) barrel column after axial stimulation of the C1 whisker. Examples from a P11, P14 and P27 mouse. Responses to the first five stimulation pulses are shown (colorbar, black: 0 spikes/s; white: 250 spikes/s). (B) Quantification of the sensory-evoked activity in the neighboring barrel column normalized to the principal barrel column firing rate for axial stimulation. (C) Quantification of cross-columnar activity for lateral stimulation. Same conventions as in (B). Data points are mean $\pm$ s.e.m. (n = 18 mice, 6 mice per age group). Statistics: Kruskal-Wallis test followed by Dunn-Sidak's post-hoc correction (* p<0.05, ** p<0.01, *** p<0.001).

2.3.5 Emerging stimulus selectivity for axial and lateral whisker stimuli

Next, we addressed the question whether exertion of axial or lateral whisker forces elicits distinctive responses in single neurons. To analyze selectivity of neuronal responses at the single-

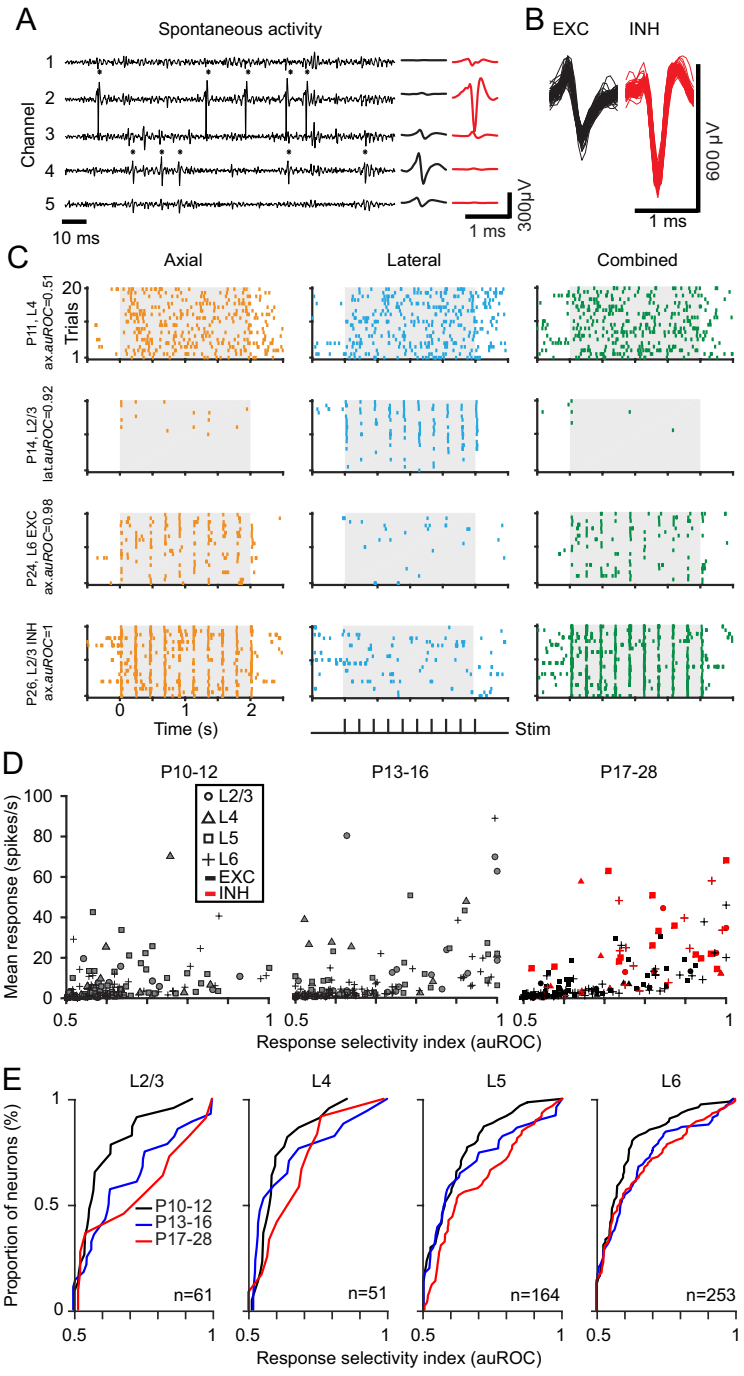

Figure 2.6: Development of single-unit response selectivity: (A) Left: High-pass filtered signals (0.8-5kHz) from five contiguous channels containing 90 ms of spontaneous activity. Black stars indicate time points at which spikes were detected and sorted (see also **Supplementary Figure 2.14**). Right: Average spike profiles of two isolated SUs. (B) Spike waveforms extracted from the channel with the highest negative peak as shown in (A) for a putative excitatory (EXC) and a fast-spiking, putative inhibitory (INH) cell. (C) Spike-raster plots of sensory-evoked activity for all stimuli in a P11, P14, P24 and P26 mouse. Gray boxes indicate whisker stimulation. Examples show non-selective (P11) and selective (P14, P24, P26) examples. (D) Pooled analysis of response selectivity index (auROC) of SUs located in the barrel column of the stimulated whisker. Data points indicate auROC for single SUs and layer identity. In the P17-28 age group, SUs are labelled as EXC (black) or INH (red) based on waveform clustering (as seen in B). (E) Cumulative distribution analysis of the response selectivity index (auROC) across cortical layers and age groups (n=5 animals per age group). Kolmogorov-Smirnov test; p-values for P10-12 vs. P13-16: [0.15, 0.18, 0.61, 0.03] for L2/3, L4, L5, L6, respectively; for P10-12 vs. P17-28: [0.06, 0.12, 0.02, 0.04]; for P13-16 vs. P17-28 [0.59, 0.18, 0.13, 0.87]; number of analyzed cells for P10-12: [23,22,57,72] for L2/3, L4, L5, and L6, respectively; P13-16: [27,17,48,85]; P17-28: [11,12,59,96].

unit (SU) level we performed multi-channel spike sorting and isolated a total of 737 SUs in 15 animals (n=5 animals per age group; P10-12: 236 SUs, P13-16: 254 SUs, P17-28: 247 SUs; see **Methods** and **Supplementary Figure 2.15**). We assigned the isolated SUs to the recording site (and the corresponding cortical layer), for which the waveform amplitude was maximal (**Figure 2.6A**). Furthermore, in the P17-28 age group we could discriminate putative excitatory (EXC) from putative inhibitory (INH) SUs based on their waveform asymmetry and spike width (**Figure 2.6B**). We identified a proportion of 22.7% putative INH SUs (56 out of 247 units) consistent with previous studies (Reyes-Puerta et al., 2015b; Sakata and Harris, 2009). For the younger age groups, discrimination of EXC and INH SUs was not feasible because waveform features were not sufficiently distinct (**Methods** and **Supplementary Figure 2.15**). We quantified the response selectivity for axial or lateral stimulation using the area under the Receiver Operator Characteristics (*auROC*; see **Methods**). We based the calculation of auROC on spike count distributions for axial and lateral stimulus-evoked responses obtained within the first 50-ms window following each stimulation pulse. SUs showed diverse response selectivity to the presented stimuli (**Figure 2.6C,D**). In the P10-12 age group, SUs generally responded with low selectivity (auROC < 0.8) whereas in the older age groups, we observed an up to 3-fold increase from pre- to post-critical period in the fraction of SUs with auROC > 0.8: (P10-12: 8%, P13-16: 18%, P17-28: 24% of SUs across all layers). Based on the cumulative distributions of auROC indices, this increase in selectivity reached significance for SUs in both L5 and in L6 (**Figure 2.6E**). INH SUs displayed high diversity in response selectivity and response strength, comprising highly responsive and selective as well as low responsive and unselective INH SUs (indicated in red in **Figure 2.6D**). Scatter distribution analysis of axial and lateral responses showed an increase in preference to axial stimulation for L5 and L6 (**Supplementary Figure 2.16**). For the combined stimulus, responsive SUs typically showed a similar response pattern as for the preferred stimulus, although some neurons responded little to combined stimulation (**Figure 2.6C**, SU example in P14 animal). These findings present evidence for emerging response selectivity in the developing barrel cortex circuitry in L5 and L6 during the same period

when active whisking and explorative behavior mature.

2.3.6 Refinement of Sensory-Evoked Activity in L2/3

To corroborate these findings for the L2/3 critical period and in order to examine developmental changes in the L2/3 cortical representation of whisker-evoked activity more comprehensively, we performed in vivo two-photon calcium imaging across the same three age groups. Following bulk loading of L2/3 with the synthetic calcium indicator Oregon Green BAPTA-1 (OGB-1; see **Methods**) we imaged a large number of L2/3 neurons with high spatial resolution (**Figure 2.7A**; 2709 cells in n=18 mice; compared to 74 SUs in n=15 mice isolated in L2/3 of which 61 were used for response selectivity analysis). Both spontaneous and evoked population activity transitioned from highly synchronized and large calcium transients before P13 to decorrelated and sparser calcium transients at older ages (**Figure 2.7B, C**). This sparsification and decorrelation was most obvious in the pooled analysis of evoked $\Delta F/F$ integrals and of pairwise neuronal correlations for the P13-16 age group for both spontaneous and evoked activity (**Figure 2.7D, E**). The proportion of neurons responding to a given stimulus decreased more than two-fold between the P10-12 and P17-28 groups indicating sparsification of overall responsiveness in L2/3 (**Figure 2.7F**). Thus, consistent with our results from MUA analysis, we conclude that responsiveness decreases in superficial L2/3, paralleled by decorrelation of spontaneous and sensory-evoked network activity in the critical period.

2.3.7 Emerging Response Selectivity in L2/3

We also analyzed whether populations of L2/3 neurons increase their response selectivity for axial or lateral whisker stimulation across development, as indicated by the SU responses. Indeed, while overall decreasing their responsiveness, neurons displayed increasing response selectivity for either axial (**Figure 2.8A**) or lateral stimulation (**Figure 2.8D**). Populations of neurons preferably responding to axial stimulation showed a significantly higher fraction of axial-selective neurons for the P13-16 and P17-28 age group compared to the P10-12 age group (**Figure 2.8B, C**). This increase in response selectivity across development was also significant

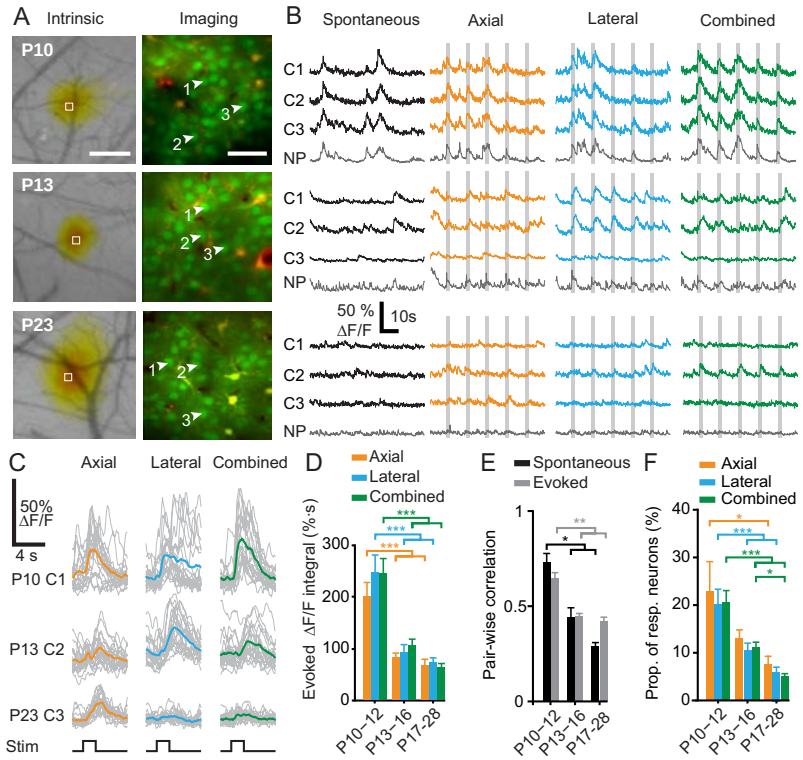

Figure 2.7: . Stimulus-evoked calcium dynamics in layer 2/3 neurons: (A) Identification of the C2 barrel using intrinsic optical imaging (left) in a P10, P13 and P23 mouse. Squares indicate imaging regions depicted on the right; Scale bar 250 µm. Right: maximum intensity projections of calcium imaging regions after cell bolus loading of OGB-1 AM (green). Sulforhodamine-101 staining of astrocytes in red; Scale bar 30 µm. (B) Raw $\Delta F/F$ traces of spontaneous (black) and sensory-evoked activity (color-coded, C1, C2, C3). Bottom gray traces show neuropil signal (NP; see **Methods**). (C) Single trial (gray) and mean (color coded) evoked calcium transients (n=20 trials per stimulus) for neurons as shown in (B) (P10: neuron 1 (C1), P13: neuron 2 (C2), P23: neuron 3 (C3)). (D) Pooled analysis of the evoked response integral for all stimuli in L2/3 (axial, lateral, combined). (E) Pooled analysis of pair-wise correlations of spontaneous (black) and sensory-evoked (gray) neuronal activity (n=3 animals, 320 cells). (F) Pooled analysis of proportion of responsive cells for a given stimulus type. Data show means $\pm$ s.e.m. (n=6 animals per age group, 2709 cells). Statistics: Kruskal-Wallis test followed by Dunn-Sidak's post-hoc correction ($*p < 0.05, **p < 0.01, ***p < 0.001$).

for neurons selective to lateral stimulation (**Figure 2.8E,F**). Neurons selective for either axial or lateral stimulation were detectable simultaneously in local populations of L2/3 networks around P14 (**Supplementary Figure 2.17**). These results provide further evidence for specific changes in whisker-evoked L2/3 neuronal dynamics in developing barrel cortex, with a reduction in response amplitude, along with an increase in response selectivity for axial and lateral whisker forces following the onset of active explorative behavior.

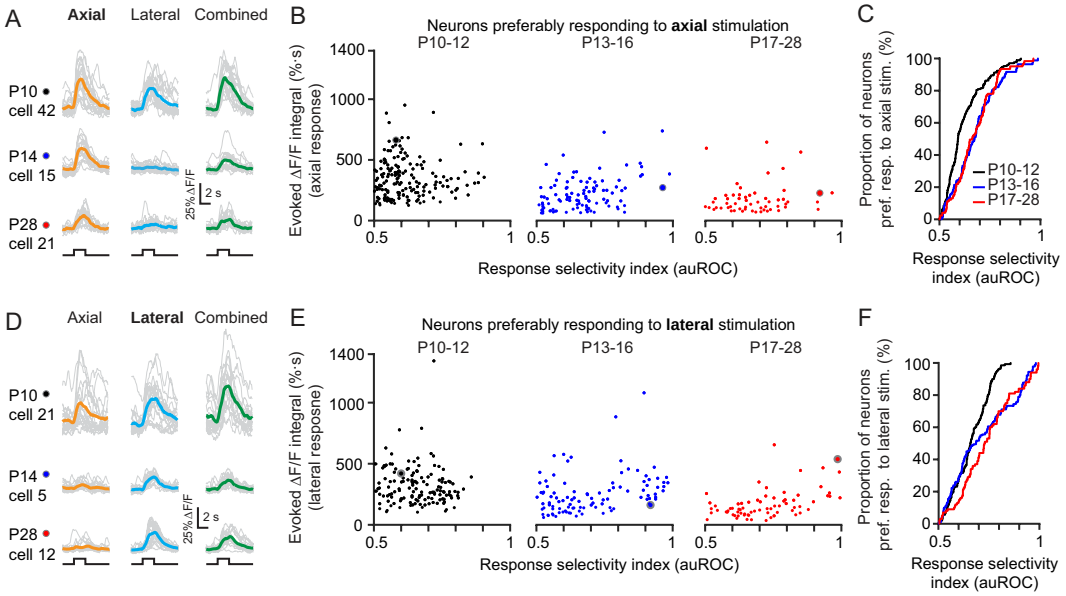

Figure 2.8: Development of single neuron response selectivity in L2/3 to either axial or lateral whisker stimulation.: (A) Single trial (gray) and mean (color-coded) evoked calcium transients (n=20 trials per stimulus) of neurons preferably responding to axial whisker stimulation. (B) Scatter-distributions of the response amplitude [expressed as the evoked $\Delta F/F$ integral ($\% \cdot s$)] and corresponding response selectivity index auROC (see **Methods**) for neurons preferably responding to axial whisker stimulation. Position of example neurons of panel (A) are indicated. (C) Cumulative distribution analysis of response selectivity (auROC) across age groups. The distributions of selectivity to axial stimulation for animals older than P13 were significantly different from young animals ($\leqslant$ P12), since their distributions contained more stimulus-selective cells with higher auROC values. Kolmogorov-Smirnov test; P10-12 vs. P13-16: $p=1.1 \cdot 10^{-10}$; P10-12 vs. P17-28: $p=3.4 \cdot 10^{-11}$; P13-16 vs. P17-28: p=0.59; 192, 86, and 54 cells for P10-12, P13-16, and P17-28, respectively; n=6 animals per age group. (D) Example evoked calcium transients of neurons preferably responding to lateral whisker stimulation. Same conventions as in (A). (E) Scatter-distributions of the response amplitude and auROC for neurons preferably responding to lateral whisker stimulation. (F) Cumulative distribution analysis of response selectivity (auROC) across age groups. Kolmogorov-Smirnov test; P10-12 vs. P13-16: $p=7.4 \cdot 10^{-9}$; P10-12 vs. P17-28: $p=2.7 \cdot 10^{-7}$; P13-16 vs. P17-28: p=0.006; 148, 95, and 69 cells for P10-12, P13-16, and P17-28, respectively; n=6 animals per age group). Note that auROC are confined to 0.5-1 (see **Methods**)

Finally, we evaluated how L2/3 neuronal responses to combined axial-lateral stimulation related to the individual component responses across development. Albeit individual neurons showed heterogeneous summation of axial/lateral responses (with a few neurons showing supralinear responses), L2/3 populations on average responded to combined stimulation in a sublinear manner. This effect was significantly more pronounced in the older age groups (**Figure 2.9**; scatter distributions from 6 animals per age group; P10-12 vs. P13-16, p = 0.00001; P10-12 vs. P17-28, p = 0.012; analysis of regressions slopes, see **Methods**). This result was corroborated by analyzing only the subsets of neurons showing highest selectivity for either

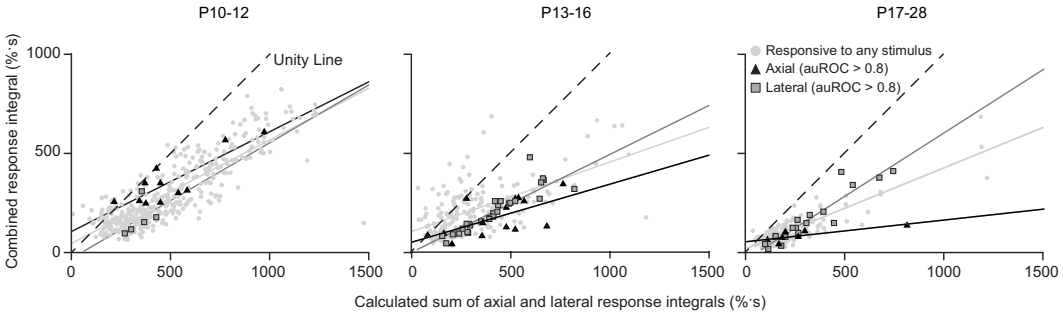

Figure 2.9: Sublinear responses of L2/3 neurons to combined axial-lateral whisker stimulation. : Scatter distribution of responses to the combined stimulus vs. the calculated linear sum of responses to axial and lateral stimulation across age groups (left: P10-12; middle: P13-16; right: P17-28). Gray dots indicate responsive neurons, black triangles and gray squares indicate highly selective (auROC > 0.8) axial-preferring and lateral-preferring neurons, respectively. Solid lines indicate regression lines, dashed line indicates the unity line. Distributions are shown for responsive neurons of 6 animals (number of neurons: P10-12: 340; P13-16: 181; P17-28: 123). Number of highly selective neurons: Axial, P10-12: 11, P13-16: 14, P7-28: 7; Lateral, P10-12: 5, P13-16: 26, P17-28: 17.

axial or lateral stimulation. Sub-linear regression distributions for both the axial- and lateral-selective neuronal subsets showed similar distributions as the grand population average (**Figure 2.9**). With increasing age, especially axial-selective neurons exhibited a significant reduction in response summation for the combined whisker stimulus (P10-12 vs. P17-28, $p = 0.0027$). Together, these findings suggest that when mice start explorative behavior, activation of cortical neurons by axial and lateral whisker force components experiences enhanced competition, possibly because of increased cortical inhibition, which could contribute to the emerging response selectivity.

2.4 Discussion

In summary, we have characterized the developmental profile of sensory-evoked activity in barrel cortex of mice between P10 and P28, including in particular the short time window around P13 when animals open their eyes and start actively exploring the environment with their whiskers. We found several layer-specific changes in response profiles at the onset of active whisking behavior. First, on the MUA and LFP level, sensory-evoked responses consistently decreased in L2/3 and L4 with age, whereas they increased in L5 and L6, irrespective of the type of stimulation (axial or lateral). Second, superficial and deep layers also differed with respect to

neuronal adaptation and its developmental profile: whereas superficial layers showed facilitation before the critical period, which then turned into slight depression, deep layers showed the opposite trend with pronounced adaptation at early age, which then became less prominent in older animals. In addition, analysis of single neuron responses revealed emerging response selectivity for axial or lateral stimuli around P14 for L2/3, L5 and L6. Together, these findings demonstrate that maturation of sensory processing in mouse barrel cortex involves substantial layer-specific changes in a short time-window at the onset of active whisking behavior.

Our results confirm previous findings demonstrating rapid functional changes of barrel cortex activity within only two to three days in the critical period around P13. These findings include sparsification and decorrelation of spontaneous L2/3 population activity (Golshani et al., 2009), sharpening of evoked temporal spiking profiles (Ikezoe et al., 2012), and changes of signal flow across large portions of the cerebral hemispheres (Quairiaux et al., 2011). The aging-related sparsification of spontaneous activity (and of sensory-evoked activity as shown here) can be explained at least in part by changes in intrinsic neuronal properties, especially a pronounced progressive decrease in input resistance (Maravall et al., 2004). Further likely causes are layer-specific changes of synapse density (Chandrasekaran et al., 2015), plasticity-induced changes of L4-to-L2/3 and L2/3-to-L2/3 synaptic connectivity (Stern et al., 2001; Wen and Barth, 2011), maturation and pruning of thalamocortical inputs (Yu et al., 2012), and maturation of the inhibitory circuitry (Zhang et al., 2011).

A new finding of our study is the emergence of response selectivity in barrel cortex during the critical period of L2/3 network maturation. Our novel stimulation paradigm allowed us to study the development of selectivity for axial or lateral whisker stimuli across cortical layers in mouse barrel cortex. We found an increased proportion of stimulus-selective neurons in L2/3, L5 and L6 in animals older than P16 compared to animals younger than P13. Our imaging experiments also revealed locally intermixed populations of neurons in L2/3 selective for either axial or lateral stimuli, emerging in the critical period. These findings indicate that L2/3 is a major integration stage for processing of these whisker forces. Comparable changes in response selectivity have also

been observed in visual cortex (Rochefort et al., 2011) although sensory processing most likely undergoes different maturation processes in barrel cortex compared to visual cortex (Clemens et al., 2012; Hoy and Niell, 2015). The representation of axial stimuli has previously been studied in trigeminal ganglion neurons (Stüttgen et al., 2008) but not in detail throughout a neocortical column. Studies in adult mice have shown that axial and lateral whisker-forces are important features for object localization (Pammer et al., 2013; Quist et al., 2014). The emerging response selectivity for axial or lateral forces that we found during postnatal week 3 occurs in parallel to the start of active tactile exploration. Response selectivity for axial whisker forces thus might be relevant for explorative behavior, when touch-induced forces become more complex. In line with this notion, a recent study found that neurons in L2/3 of adult mice are selectively tuned for whisker distance relative to a virtual corridor wall (Sofroniew et al., 2015). We therefore speculate that enhanced neuronal selectivity to axial/lateral force components may help the young mouse to judge object parameters such as object distance and texture during exploration. Whether changes in whisker mechanics, maturation of the whisker follicle, and changes in peripheral signal transmission may contribute to this development remains unclear, but we did not observe any obvious changes in whisker stiffness or thickness in the critical period. Future studies could investigate the maturation of peripheral and thalamocortical circuit components and their contribution to whisker-related sensory processing.

Our experimental data suggest that not only axial and lateral response selectivity increases during the critical period, especially in L2/3, but that neuronal activity patterns evoked by these whisker force components also interact, evident in the sublinear summation of responses observed in the case of combined stimulation. The observed increase in sublinear processing with age hints towards competition of whisker-evoked inputs on the local neocortical circuit level, although on an MUA level these stimuli induce very similar response profiles. If and how this competition is facilitated by specific subsets of cells in the local circuitry of L2/3 networks, in particular inhibitory interneurons, or by modified transmission through the whisker and the follicle remains to be explored. The maturation of cortical circuits in barrel cortex can

be disrupted during early development if whiskers are plucked or trimmed (Van der Loos and Woolsey, 1973; Skibinska et al., 2000). Overall sparsification and decorrelation in barrel cortex is, however, believed to be intrinsically mediated in L2/3, as whisker deprivation does not alter the sparsification of spontaneous population activity (Golshani et al., 2009). It remains unclear whether emergence of response selectivity in barrel cortex is mainly driven by an intrinsic program or whether it relies on specific experience-dependent inputs during active exploratory behavior. In visual cortex, sparsification of sensory-evoked activity is delayed in dark-reared mice but selectivity emerges independent of visual input, even before eye opening (Rochefort et al., 2009, 2011). Further studies are needed to dissect intrinsic and experience-dependent mechanisms that underlie the development of response selectivity in barrel cortex. The short time window, during which most of the change happens, and the slow regrowth of whiskers will make such experiments challenging.

Our electrophysiological data also provide evidence for refined whisker-evoked adaptation and increased response selectivity in L5 and L6 after the critical period. Both EXC and INH SUs showed increased selectivity for either axial or lateral stimuli. We assume that neurons in L5, including stimulus-selective INH neurons, play an important role in processing different whisker forces for the principal whisker as L5 thick-tufted cells are major output neurons of the cortex, further conveying whisker information to downstream brain areas (De Kock et al., 2007). The exact role of specific neuronal sub-types in the developmental processes warrants further investigation.

In conclusion, we have shown that processing of sensory information in barrel cortex changes substantially within a short developmental period (between P13-16), in parallel to the onset of active whisking behavior. This maturation includes layer-specific changes in stimulus responsiveness and adaptation and the development of response selectivity. The development of new tools and techniques for longitudinal investigation of network maturation (for example expression of genetically encoded calcium indicators, or chronically implanted electrodes) might help to further dissect the underlying mechanisms and better connect the observed changes in cor-

tical processing to behavioral adaptations.

2.5 Supplementary Information

Supplementary Movies are available at http://cercor.oxfordjournals.org/lookup/suppl/doi:10.1093/cercor/bhw280/-/DC1

Supplementary Movie 1: Real-time videos of movement trajectories in an open field arena of one mouse at ages P10, P15 and P28. The tracking of the mouse movement trajectory in the 2-min observation time are depicted in the bottom white boxes (the snout of the mouse was used as a tracking reference point). Scale bars: 5 cm.

Supplementary Movie 2: High-speed videography of axial, lateral and combined stimulation of the C2 whisker in vivo. One stimulation pulse of the 10 successive stimuli is shown (10 ms). Scale bar: 1 cm.

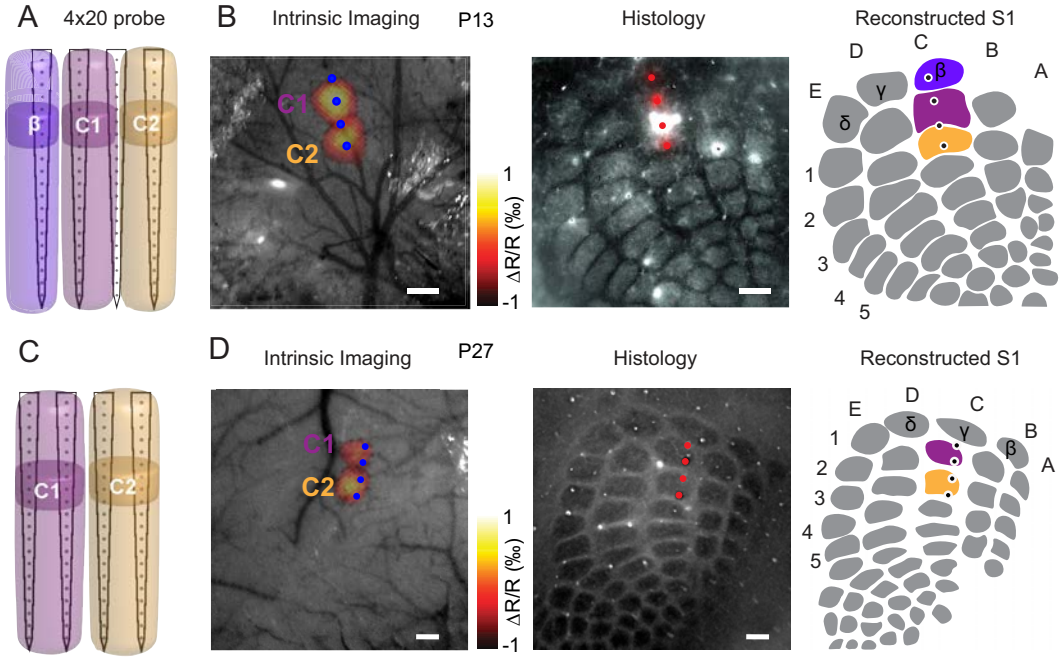

Supplementary Figure 2.10: Insertion of multi-electrode arrays guided by intrinsic optical imaging and confirmed by histology.: (A) Schematic illustration of the 4x20 silicon probe and its relative position to the C1 and C2 whisker-related columns in barrel cortex of a P13 mouse (see **Materials and Methods** for identification of L4 and barrel columns). (B) Left, average intrinsic signals used to identify the C1 and C2 columns after repeated single-whisker deflections in a P13 mouse. Scale bar: 200 µm. Middle, image of tangential sections stained for cytochrome oxidase (COX) post-mortem. Right, reconstructed barrel map based on COX staining as seen in the middle with electrode positions. The insertion points were identified by DiI-labeled shank penetrations on the COX staining. (C) Relative position of the 4x20 multi-electrode in C1 and C2 of a P27 animal. (D) Left, intrinsic signal of C1 and C2 columns in P27 mouse. Scale bar: 200 µm. Middle, COX staining revealing the position of the shanks. Scale bar: 200 µm. Right, reconstructed barrel map based on COX staining including parts of the anterior lateral barrel subfield.

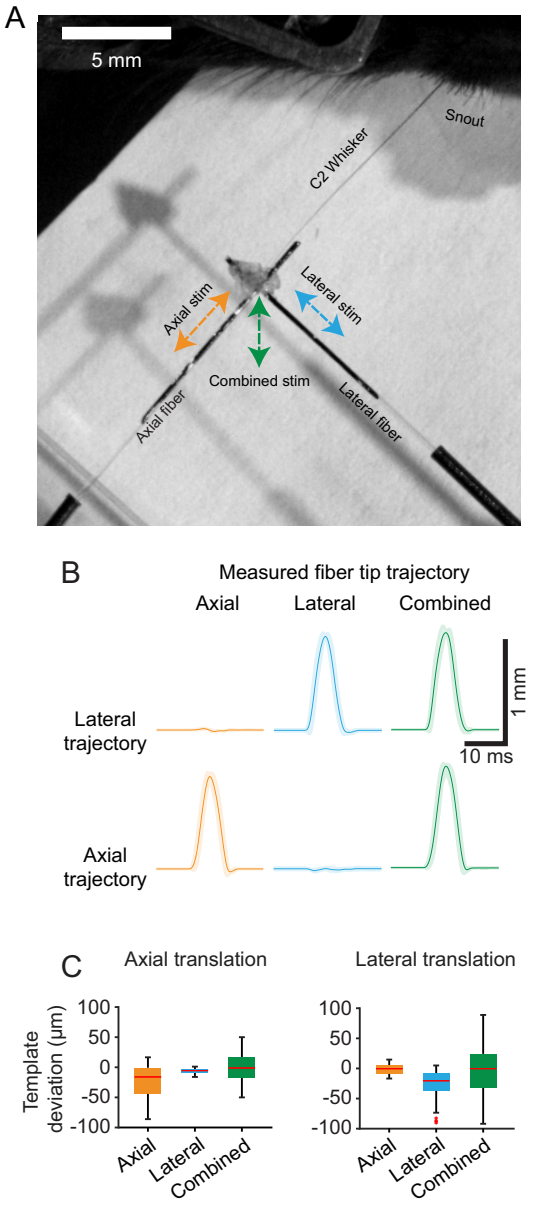

Supplementary Figure 2.11: Precise control of axial and lateral whisker movements: (A) Single frame of high-speed videography used to extract the whisker envelope as seen in **Figure 2.2C**. Stimulation for each stimulus type is applied by translating the axial or lateral optical fiber independently (axial, lateral stimulus) or simultaneously (combined stimulus). (B) Analysis of fiber movements from high-speed video tracking of the whisker attachment point for all stimuli. Fiber tip trajectories for both lateral and axial components showed negligible cross-talk and high temporal precision (mean $\pm 2 \cdot$s.d of 10 stimulus pulses). (C) Quantification of trajectory deviations from the template waveform for stimulus types shown in (C). Box plots show the distributions of deviations across all measured time points. Even the largest deviations remained below 100 µm (combined stimulus).

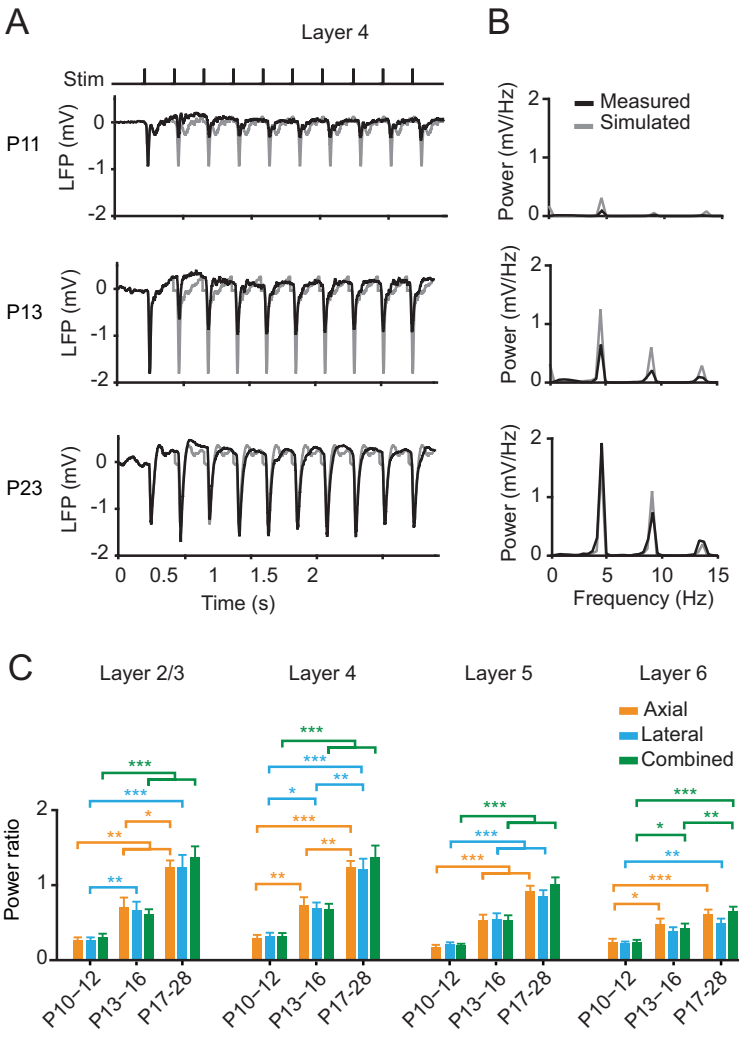

Supplementary Figure 2.12: Sensory-evoked LFP response adaptation across cortical layers: (A) Quantification of LFP adaptation by comparing the measured LFP trace (black) with a simulated trace (gray) consisting of continuous responses of the first LFP depolarization for a P11, P13 and P23 mouse in layer 4. (B) Power spectrum analysis (discrete Fourier transform) of the response frequency and power at the stimulation frequency (4.76 Hz, 10-ms pulses followed by 200-ms inter-stimulus intervals). A responsiveness index (RI) was calculated from the ratio of power between the simulated and measured LFP trace. In the P11 example (top), the responses for the consecutive stimulus presentations are smaller than the first evoked pulse. As a result, the RI is <1. In the P23 example, the power spectra for both measured and simulated LFP responses are close to 1 (for further information see (Katz et al., 2006). Note that peaks around 10 and 15 Hz indicate higher harmonics of the frequency dependent RI.(C) Statistical analysis of RI across age groups and layers. RIs increase significantly with age and therefore response adaptation decreases. High response adaptation can be observed in animals younger than P12 (also see sensory-evoked responses in **Figure 2.3A**, n=6 animals per age group). Note that response profiles and RI's were not biased for any stimulation type. Statistics: Kruskal-Wallis test followed by Dunn-Sidak's post-hoc correction (* p<0.05, ** p<0.01, *** p<0.001).

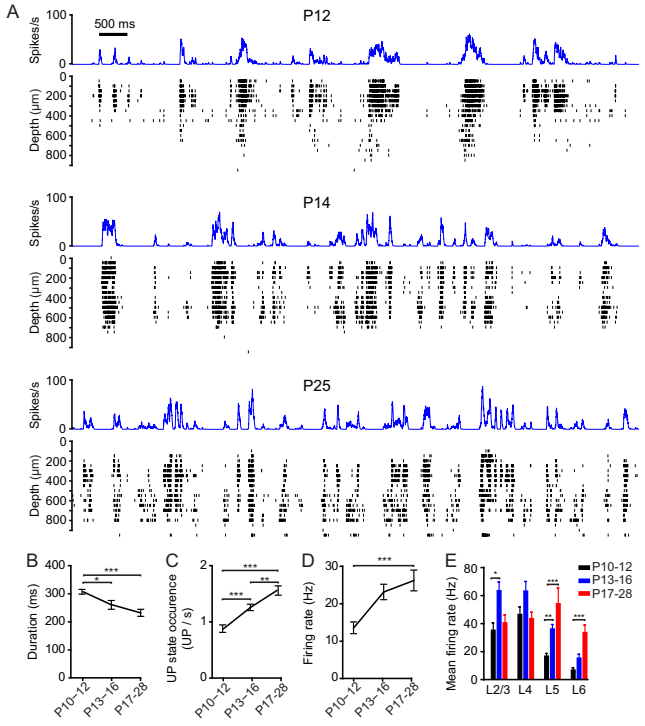

Supplementary Figure 2.13: Quantification of spontaneous up-state synchrony across a cortical column: **(A)** $10s$ of spontaneous activity for three example mice at age P12, P14 and P25. Top traces indicate smoothed averaged multi-unit activity across all cortical layers. Data represents activity for one barrel column (and recording shank). Multi-unit raster plots indicated in black. **(B)** Quantification of the duration of up states across age for $600s$ of spontaneous activity ($n = 6$ animals per age group). Up-states were identified by following criteria: (1) the smoothed MUA exceeded a specific up-state threshold (see Experimental Procedures), (2) the mean MUA in a $100ms$ window before the onset candidate was below the up-state threshold, and (3) the duration of the up-state event was longer than $50ms$. UP-state duration significantly decreased with age (in agreement with Sakata and Harris (2009)). **(C)** Quantification of up-state occurrence (UP /s, $n = 6$ animals per age group). The occurrence of up-states significantly increased with age. **(D)** Mean firing rate during up-states (mean $\pm$ s.e.m. of 20 recording sites, $n = 6$ animals per age group) significantly increase with age. **(E)** Mean firing rate across layers and age groups (mean$\pm$ s.e.m., $n = 6$ animals per age group). Statistics: Kruskal-Wallis test followed by Dunn-Sidak's post-hoc correction ($*p < 0.05, **p < 0.01, ***p < 0.001$).

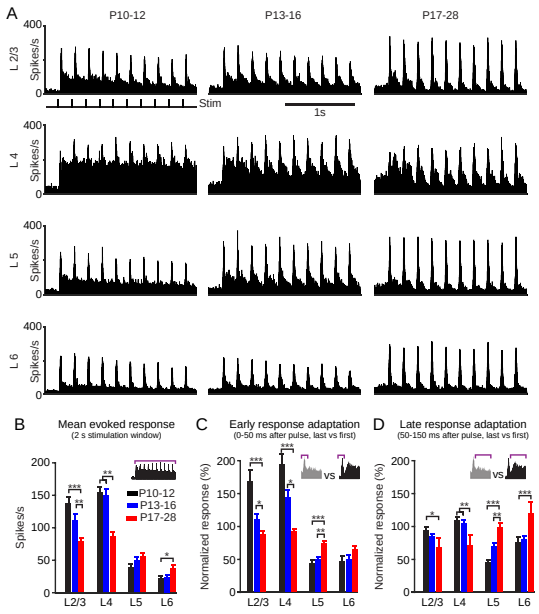

Supplementary Figure 2.14: Intra-columnar development of sensory-evoked activity for lateral whisker stimulation: (A) Pooled average multi-unit activity across cortical layers and age. (B) Pooled analysis of the mean evoked response (2 s) for all cortical layers and age groups. (C) Quantification of early response adaptation (0-50 ms after stimulation pulse). Normalized responses indicate the ratio for the last vs. first stimulation pulse. (D) Quantification of late response adaptation (50-150 ms) for the last vs. first stimulation pulse. Data points are mean $\pm$ s.e.m. (n = 18 mice, 6 mice per age group). Statistics: Kruskal-Wallis test followed by Dunn-Sidak's post-hoc correction (* p<0.05, ** p<0.01, *** p<0.001).

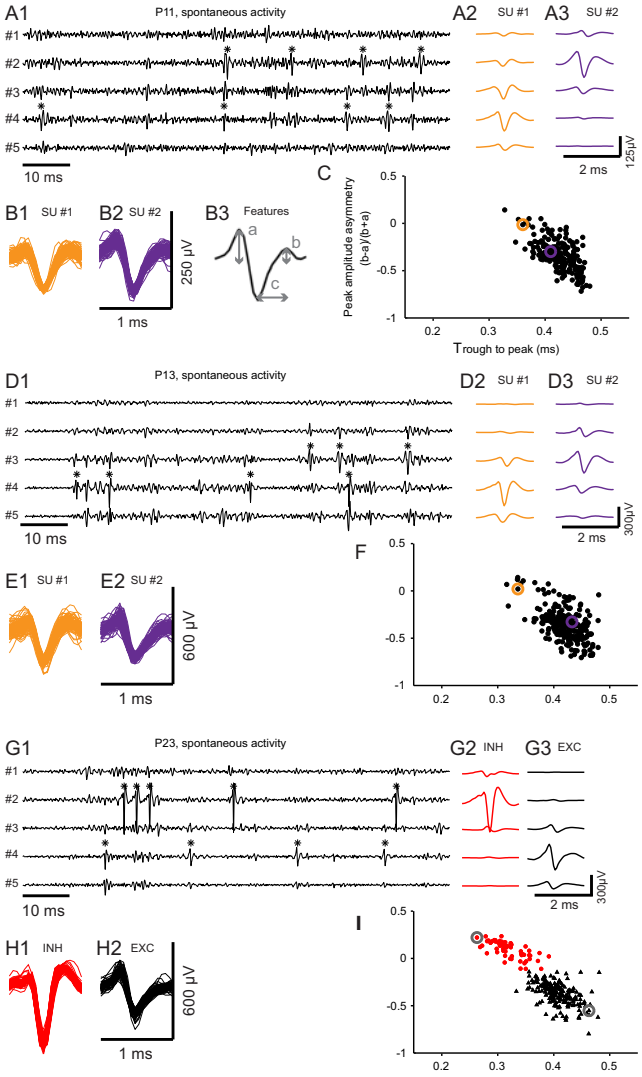

Supplementary Figure 2.15: Multi-channel spike sorting: (A1) High-pass filtered signals (0.8–5 kHz) from five contiguous channels containing 90 ms of spontaneous activity (P11 animal). Black stars mark the time points at which spikes from two single units were detected and sorted. (A2&3) Average spike profiles of the two illustrative single units across the five recording channels. (B1&2) Spike waveforms extracted from the channel with the highest negative peak, which represent the two neurons displayed in panel A. (B3) Schematic drawing illustrating the three features extracted from the spike waveforms to perform neural classification: a and b, left (early) and right (late) baseline to peak amplitudes; c, trough to peak latency. The first two features were used to calculate the peak amplitude asymmetry $[(b-a)/(b+a)]$. (C) Distribution of all neurons recorded in the P10–12 age group (n=236 neurons from 5 animals) in relation to the two parameters described in panel B3. Open circles mark the position of the exemplary waveforms from panes B1&2. Although a group of 9 cells (of 236) could be separated from the rest, their small proportion (3.8%) and low level of isolation could not be used to establish two differentiated neuronal groups. In this regard, note that the estimated proportion of GABAergic neurons in the mouse neocortex is 20%, being constant from near the start of neurogenesis to adulthood (Sahara et al., 2012; Tamamaki et al., 2003). (D–E) Same as in panel (A), displaying two exemplary neurons from a P13 mouse. (F) Distribution of all neurons recorded in the P13–16 age group (n=254 neurons from 5 animals) according to their spike waveforms. As in the previous age group, the small proportion of dissociable cells (n=14 of 254, 5.5%) could not be used to separate two physiologically characterized neuronal clusters. (G–H) Two exemplary neurons recorded from a P23 animal. (I) Distribution of all neurons recorded in the P17-28 age group (n=247 neurons from 5 animals). In this case, a clear clustering of the two neuronal groups – putative excitatory (EXC, red triangles) and inhibitory (INH, blue filled circles) neurons – could be obtained by the k-means algorithm using the two parameters described in B3. The resulting automatic separation reflected a physiological proportion of INH cells within the neocortex (n=56 out of 247, 22.7%).

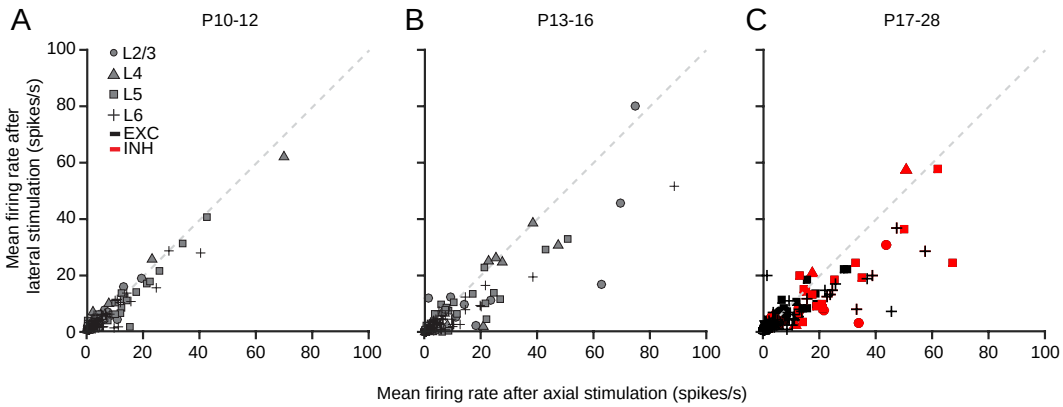

Supplementary Figure 2.16: Single unit response distribution to axial and lateral whisker stimulation.: (A) Scatter distribution of axial and lateral mean firing rate (spikes/s) for SUs in the P10-12 age group. SUs are labelled according to recording depth (L2/3: circle; L4: triangle; L5: square; L6: cross). Dashed line indicates slope one. (B) Scatter distribution with same conventions as in (A) for the P13-16 age group. Note the increased scattering towards axial or lateral stimulation indicating increased selectivity towards one stimulus. (C) Scatter distribution with same conventions as (A) and (B) for the P17-28 age group. Additionally, EXC and INH SUs are color coded (EXC: black; INH: red).

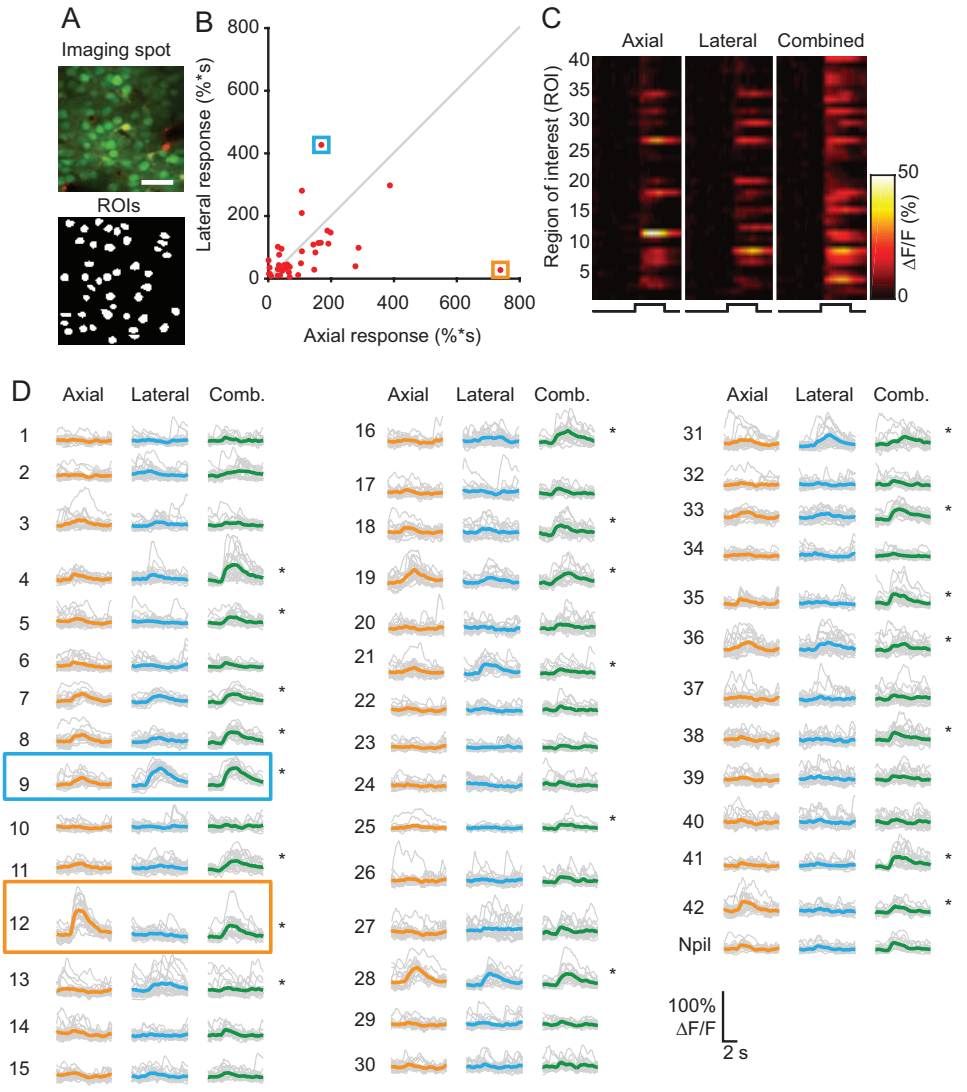

Supplementary Figure 2.17: Response heterogeneity in local populations of L2/3 neurons after multi-directional whisker stimulation .: (A) Top: Maximum intensity projection of calcium imaging region after cell bolus loading with OGB-1 AM (green) in a P14 animal. Sulforhodamine staining of astrocytes in red. Scale bar 30 µm. Bottom: Regions of interest (ROIs) extracted from the maximum intensity projection image. For this imaging spot a total of 42 ROIs could be extracted. (B) Scatter distribution of the axial and lateral response integral ($\% \cdot s$). Red dots indicate the response after axial or lateral stimulation. Blue box indicates a neuron with strong responsiveness to the lateral stimulation, orange box indicates neuron with high responsiveness to axial stimulation. (C) Heatmap representation of the responses to all stimuli (axial, lateral and combined). ROI 9 corresponds to the neuron labelled with the blue box, ROI 12 corresponds to the orange box, respectively. (D) Single trial (gray) and mean (color coded) evoked calcium transients (n=20 trials per stimulus) for all ROIs. Responsive neurons (here 50%, 21/42) are indicated by asterisks. The lateral selective (blue, ROI 9) and axial selective (orange, ROI 12) are indicated. In rare cases, neurons respond mainly to combined stimulation and little to axial or lateral stimuli (see ROI 4, 11, 41).

The qualities of number appear to lead to the apprehension of truth.

Plato, *The Republic 7*

3

Whisker-specific signal detection in developing mouse barrel cortex

Alexander van der Bourg[1], Jenq-Wei Yang[1], Vicente Reyes-Puerta, Maik C. Stüttgen, Fritjof Helmchen[2] and Heiko L. Luhmann[2]

In preparation; [1]co-first authors, [2]co-senior authors

My contributions to this study were the following: I was responsible for and involved in conceptualization and experimental design of the study. I performed silicon probe electrophysiology in a one month collaboration project in the laboratory of Prof. Heiko Luhmann together with postdoctoral researcher Jenq-Wei Yang. I wrote the first draft of the manuscript, prepared all figures and was strongly involved in data analysis.

Rodent rhythmic whisking behavior develops in a critical period two weeks after birth when animals start to increasingly use tactile sensation to explore the environment. How sensory processing of whisker-induced inputs develops in primary somatosensory cortex S1 in this period remains poorly understood. Here, we characterized neuronal dynamics evoked by single- or multi-whisker stimuli in developing mouse barrel cortex across all cortical layers. We performed multi-electrode recordings in anesthetized mice of three age groups: before (<P13), during (P13-P16) and after (P17-P30) the onset of active whisking behavior. We find layer-specific changes in multi-unit activity (MUA) for principal and neighboring whisker-related barrel columns: MUA increased with stimulus intensity of single-whisker deflections in mice younger than P13 in L2/3 and L4 and was confined to the principal barrel column. In animals older than P16, MUA significantly decreased in L2/3 and L4 for the principal column but increased for the neighboring column with increasing stimulus intensity. At the same time, MUA increased in L5 and L6 for the principal column. Paired-pulse stimulation of single whiskers with varying stimulus intervals showed facilitation in L2/3 and L4 before the critical period whereas in animals older than P16, MUA was strongly reduced after the second pulse in all layers. Sequential activation of two neighboring whiskers with varying stimulus intervals evoked distinct response profiles in the stimulated barrel columns, depending on the direction and temporal separation of the stimuli. Isolated single units showed progressively more diverse activation patterns with age, indicating refined processing of whisker-specific inputs. We conclude that neuronal activity is increasingly modulated with stimulus intensity in L2/3 and L4 for the principal and neighboring barrel-column but not for L5 and L6. At the same-time, sequential activation of two whiskers elicited distinct responses for the principal and neighboring barrel column depending on the applied sequence and temporal separation across all layers. In the future, our findings may help to understand how the processing of sensory information relates to emerging whisking behaviors of young mice.

3.1 Introduction

Rodent primary somatosensory cortex (S1) is an excellent model to study sensory integration of tactile stimuli, structural and functional plasticity, decision making and development. Many aspects of single- and multi-whisker sensory-evoked activity have been studied in adult rodent barrel cortex. However, little is known about the corresponding functional changes and processing of whisker-evoked activity during development, especially at the onset of active exploratory whisking behavior.

Mouse active whisking behavior matures during the first three postnatal weeks. In the first week after birth, vibrissa movements transition from spontaneous unilateral muscle twitches of the whisker pad to regular bilateral rhythmic whisking at the end of the third postnatal week (Arakawa and Erzurumlu, 2015; Grant et al., 2012). At the same time, cortical connectivity undergoes major re-organization, including the maturation of layer (L) 4 to L2/3 connectivity (Stern et al., 2001) and strengthening of local connectivity between neurons in L2/3 (Clem and Barth, 2006; Clem et al., 2008; Itami and Kimura, 2012; Wen and Barth, 2011). These changes in connectivity are accompanied by changes in spontaneous activity from highly correlated bursts of action potential firing (Khazipov and Luhmann, 2006; Yang et al., 2009) to desynchronized and sparse activity in the second postnatal week (Golshani et al., 2009). These changes in overall connectivity are reflected by the functional maturation of neural circuitry, as sensory-evoked activity develops in a layer-specific manner around that time (van der Bourg et al., 2016). Further evidence demonstrated, that lateral spread and communication between barrel-columns and sensory areas is increased at the onset of whisking behavior (Ackman et al., 2014; Quairiaux et al., 2011; van der Bourg et al., 2016) which is essential for sensory integration of tactile information.

A recent study demonstrated that neurons exhibit a diverse set of spatially and temporally confined multi-whisker receptive fields that are facilitated by concise surrounding whisker input in adult rat barrel cortex (Ramirez et al., 2014). Although these findings are essential for our understanding of whisker-evoked computation, little is known about the maturation of such

receptive fields.

The receptive field properties of neurons for isolated single-whisker evoked activity have been well studied (Brecht et al., 2003; Manns et al., 2004; Hemelt et al., 2010). During active tactile exploration, rodents contact objects with multiple whiskers resulting in spatiotemporally defined and diverse activation patterns. The response properties of neurons in S1 are highly sensitive to such stimuli involving many parameters such as the different force components exerted on the whisker upon touch as well as the temporal timing during active whisking (Diamond et al., 2008; Pammer et al., 2013). The receptive field and response properties of single neurons for complex stimuli have only been recently explored as it has been technically challenging to develop systems to stimulate multiple whiskers (Jacob et al., 2010; Ramirez et al., 2014). Despite these more complex receptive field properties, many labs have investigated the impact of sensory-evoked activity for two neighboring whiskers, by sequential deflections of two whiskers. These studies have reported conflicting findings. One set of reports found strong suppression of stimulation of one whisker upon the response to stimulation of another whisker, using both electrophysiological recordings (Brumberg and Simons, 1996; Carvell and Simons, 1988; Mirabella et al., 2001) and optical imaging techniques (Ego-Stengel and Souza, 2005; Goldreich et al., 1998; Kleinfeld and Delaney, 1996). The other set found facilitatory effects upon neighboring whisker stimulation (Erchova et al., 2003; Ghazanfar et al., 2000; Shimegi et al., 1999). These discrepancies could arise from differential experimental procedures, namely the range of inter-stimulus intervals (ISIs) used, and the limited type of recorded cells obtained with electrophysiology approaches (Ego-Stengel and Souza, 2005). The receptive field properties of neurons during early postnatal development (<P10) have only recently been explored and show an imprecise whisker map, as whiskers compete for the cortical target region in barrel cortex (Mitrukhina et al., 2015). How and if these receptive field properties change through facilitation or suppression at the onset of whisking behavior around P13, remains unexplored.

Using a previously introduced novel whisker stimulation system (as described in Chapter 2 and documented in Appendix A), we here examined the spatiotemporal processing of single-

and dual-whisker stimuli before, during and after the critical period of barrel cortex maturation. We find that stimuli with increasing stimulus intensity are differentially modulated in a layer-specific fashion across all layers. Delivering two well-timed whisker deflections resulted in layer-specific facilitation of sensory responses in L4 before the critical period, which was significantly reduced at the onset of whisking. Furthermore, sequential activation of the C1 and C2 whiskers with varying inter-stimulus intervals evoked distinct response profiles in the stimulated barrel columns, depending on the direction and temporal separation of the stimuli. Isolated single units showed progressively more diverse activation patterns with age, indicating refined processing of these inputs. Together, these findings reveal substantial refinements of spatiotemporal processing of whisker-evoked activity in barrel cortex at the onset of active whisking behavior.

3.2 Experimental Procedures

3.2.1 Animal Surgery and Preparation

All preparations and experiments were approved by the local German ethics committee (#23177-07/G10-1-010) and followed the European and German regulations (European Communities Council Directive, 86/ 609/ECC). Electrophysiology experiments were conducted in 18 C7BL/6 mice (9 males and 9 females) at ages ranging from P10 to P28. Mice were sedated with chlorprothixene (0.1 g/kg, intraperitoneal (i.p.); Sigma-Aldrich Chemie GmbH, Buchs, Switzerland) and lightly anesthetized with urethane (0.25-0.5 g/kg, i.p.). Atropine (0.3 mg/kg; Sigma-Aldrich Chemie GmbH, Buchs Switzerland) and dexamethasone (2 mg/kg; aniMedica GmbH, Senden-Bösensell, Germany) were administered subcutaneously (s.c.) to reduce secretion of saliva and to prevent edema (both were injected s.c. after induction of anesthesia with urethane). Body temperature of the animal was maintained at 37 ° C with a heating pad. Hydration levels were checked regularly and maintained by s.c. injections of Ringer-lactate (Fresenius Freeflex; Fresenius Kabi AG, Oberdorf, Switzerland). Depth of anesthesia was evaluated regularly by a reflex pinch test on the hind paw. A custom-built head plate was glued to

the animal with dental cement (Caulk Grip Cement) to secure and stabilize the animal during electrophysiology recordings. After identifying the mapped C1 and C2 barrel columns through intrinsic optical imaging, a small cranial window of 1.5x1.5 mm^2 was opened. Cranial windows were opened with a sharp razor blade and superfused with Ringer's solution (in mM: 145 NaCl, 4.5 KCl, 10 HEPES, 1 $mgCl_2$, 1.8 $CaCl_2$; pH 7.2 adjusted with NaOH). The exposed neocortex was then penetrated by the multi-electrode and sealed with agarose (type III-a, 1% Ringer, Sigma).

3.2.2 Intrinsic optical imaging

The C1 and C2 whisker-related barrel columns were identified using optical imaging of intrinsic signals. The cortical surface was imaged through the intact bone by surface application of Ringer's solution. Reference images of the cortical blood vessel pattern were visualized by a 546-nm LED to enhance contrast. Functional maps of the target barrel columns (C1 and C2) were obtained by shining red light (625nm LED) on the cortical surface while stimulating the C1 or C2 whiskers individually. A single whisker was deflected with a protruding device consisting of a miniature solenoid actuator which was controlled by a transistor-tranistor logic (TTL) pulse. The actuator was placed orthogonal to the base of the whisker around 2-3 mm from the snout. Whiskers were stimulated rostrocaudally by translating the actuator at 75 mm/s (2.2 °/ms) in a short 16 ms pulse. Stimuli were presented for 5 s at 5 Hz with 8 s inter-stimulus intervals. Reflectance images were collected with a MiCam ultima L high-speed camera system (Scimedia, Costa Mesa, CA, USA; 100 x 100 binned pixels, for 100 µm per pixel). Using a C-mount extension tube, the field of view was limited to 2.6 x 2.6 mm^2 to reduce vignetting (26 µm pixel size, 500 fps). Functional intrinsic signal images were computed as fractional reflectance changes relative to the pre-stimulus average (10 trials, averaged). The intrinsic signal images obtained for the C1 and C2 barrel columns were then mapped to the blood vessel pattern to guide the location of the craniotomy and insertion of the multi-electrodes.

3.2.3 Histology

After each experiment, the animal was deeply anesthetized and the brain was perfused. For a detailed description consult the histology subsection 2.2.4 in Chapter 2. Perfused brains were sectioned tangentially and treated with cytochrome-oxidase (COX) immunohistochemistry for further analysis.

3.2.4 Galvanometer-driven whisker-stimulation

Whisker stimulation was performed with a galvanometer-driven stimulation system as introduced in Chapter 2 and documented in Appendix A. One galvanometer was attached for the C1 and C2 whisker, respectively, taking into account variations in resting position angles and relative anterior-posterior location shifts. The fibers were secured with a micro-manipulator. Deflections were applied in the anterior-posterior direction with varying amplitudes and inter-stimulus intervals. Stimulation pulses consisted of a 100 Hz phase-shifted cosine.

3.2.5 In-Vivo High-Density Multi-electrode Recordings

Neural activity was recorded with an 80-channel silicon-probe inserted perpendicular into the C1 and C2 columns of barrel cortex. Each of the four shanks contained 20 recording sites (3 mm long), spaced 50 µm apart. Shank distance was 150 µm. For a detailed description, see subsection 2.2.6 in Chapter 2. All data was continuously digitized at 20 kHz and stored offline on a 256-channel extracellular recording system and software (MC_Rack, Multi Channel Systems, Reutlingen Germany).

3.2.6 Analysis of Local Field Potentials

Local field potentials (LFP) traces were obtained by low-pass filtering (1-300 Hz) of the continuously digitized recored field potential data. For analysis, LFP traces were corrected for variations in baseline voltage levels by applying a detrending polynomial fit. Response peaks were detected as the difference between response onset and local minimum of the LFP trace.

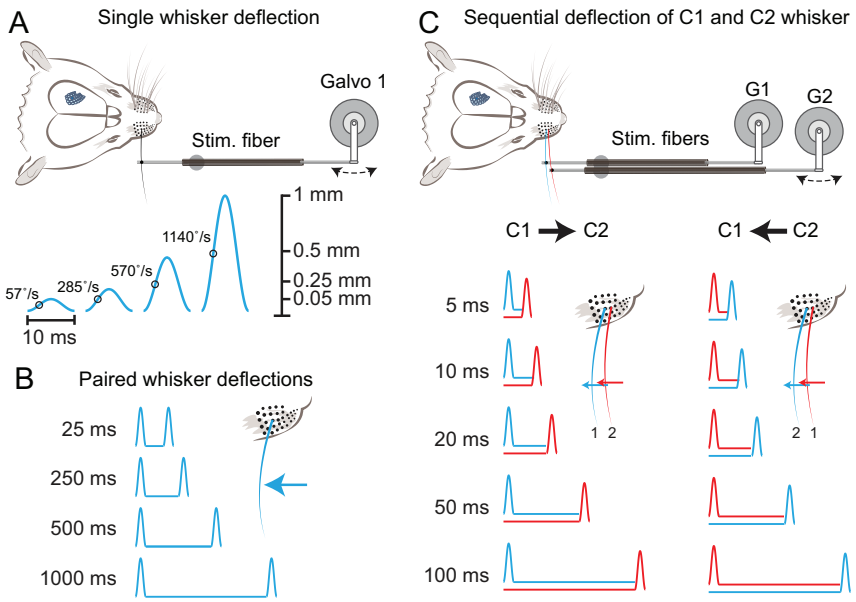

Figure 3.1: Galvanometer driven single- and multi-whisker stimulation: (A) Single whisker stimulation with varying stimulus intensity. Single whisker stimuli consisted of a 10 ms half-cosine pulse with peak velocities ranging from 57 °/s to 1140 °/s. (B) Paired whisker deflections were performed with the same 10 ms half-cosine pulse as in A. Inter-stimulus intervals between pulses ranged between 25 ms and 1 s. Stimuli were delivered with 1mm amplitude (as in strongest stimulus of A). (C) Sequential deflections of the C1 and C2 whisker were driven by two separate galvanometers. We applied antero-posterior deflections of the C1 and C2 whisker in two configurations: in the first configuration, the C1 whisker is deflected, followed by C2 whisker deflection with varying inter-stimulus intervals between 5 ms and 100 ms. The same was performed for first deflecting the C2 whisker and then deflecting the C1 whisker. Stimuli were delivered with 1mm amplitude

Paired-pulse ratios (PPRs) were calculated from the peak of two LFP traces (second divided by first peak).

3.2.7 Analysis of Current-Source Density Maps

CSD maps were computed as the second spatial derivative from the average LFPs of up to 100 trials as described previously (Mitzdorf, 1985; Nicholson and Freeman, 1975; Reyes-Puerta et al., 2015b). The computed data where then interpolated and visualized as pseudo-color images, with current sources and sinks represented by red (positive) and blue (negative) colors, respectively. CSD sinks present at the thalamo-recipient L4, L5 and L6 were used to assign recording sites to cortical layers (Reyes-Puerta et al., 2015b).

Furthermore, current sinks in L2/3, L4 and L6 were used to analyze changes in single- and dual-whisker sequential activation sequences by calculating the differences in the CSD response

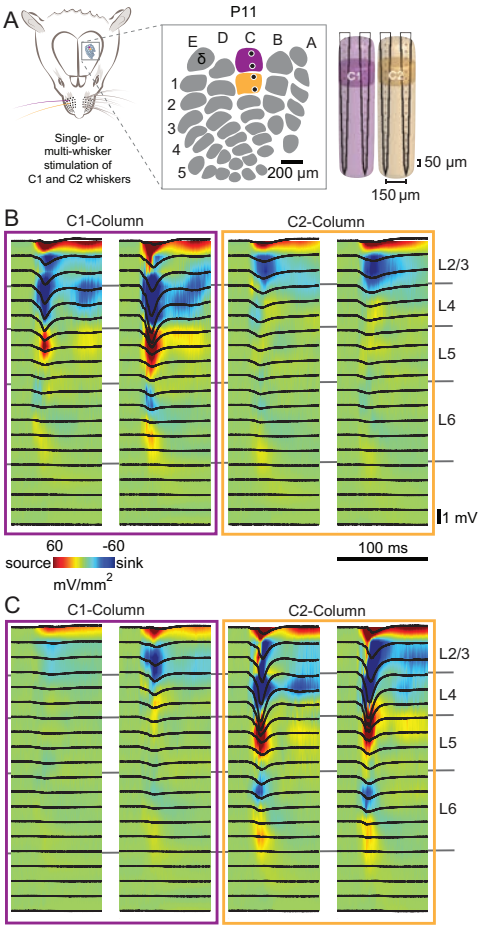

Figure 3.2: Multi-electrode array recordings of C1 or C2 whisker-evoked activity: (A) Example recording of neuronal activity in a P11 mouse. Right, schematic of multi-electrode array placement relative to the reconstructed barrel map. For all animals, the array was inserted perpendicular to the C1 and C2 barrel columns (with small variations in relation to the barrel field). (B) CSD maps computed from 100 stimulation pulses applied to the C1 whisker (10ms, 1140 °/s as seen in **Figure 3.1A**). Sinks are indicated by blue and sources by red colors. Borders of cortical layers were identified from the CSD maps and stimulus onset times, indicated as gray traces in the background. (C) Stimulation of the C2 whisker. Same conventions as in A.

integral across age groups (area under the curve, base-to-base). CSD difference maps were calculated by subtracting a single-whisker evoked response from the second response in the sequential response profile.

3.2.8 Spike Detection and Sorting

Multi-channel based spike detection and sorting was performed as described in section 2.2.8 in Chapter 2: the continuously recorded raw data signals were high-pass filtered (0.8-5kHz) and non-overlapping groups of 2-4 contiguous channels were selected as *virtual tetrodes*. For each group independently, spike detection was performed using amplitude-thresholding. The resulting extracted spikes contained the sampled amplitude values from all channels in the group in a time range from -0.5 to 0.5 ms relative to the waveform negative peak. We then computed fea-

ture vectors from these spike waveforms containing three values for each channel (negative peak amplitude plus the two first principal components derived from the waveforms). The obtained feature vectors were then sorted using *KlustaKwik* (`http://klustakwik.sourceforge.net`) and *Klusters* (`http://klusters.sourceforge.net`) (Reyes-Puerta et al., 2015b,a). To ensure high quality of the isolated single units, we accounted for clear separation of spiking by (1) a clear refractory period present in the activity of the isolated units, (2) a stable spontaneous firing rate during the whole duration of the recordings, and (3) a valid isolation distance obtained during the spike sorting procedure (Reyes-Puerta et al., 2015b). Cells were subsequently classified as putative inhibitory (INH) and excitatory (EXC) units based on their mean waveform asymmetry (Reyes-Puerta et al., 2015b). Peri-stimulus time histograms (PSTHs) of single units were computed using a 5 ms sliding time window.

Statistical Analysis

Data are represented as mean ± s.e.m. unless stated otherwise. One- or two-way ANOVA was used to test for significance for normally distributed data, followed by post-hoc Tukey's test. The Kruskal-Wallis test was used for non-normally distributed data, followed by Dunn-Sidak's post-hoc test. Significance threshold was set to $p<0.05$; in the figures, different degrees of evidence against the null hypothesis are indicated by asterisks ($p<0.05$: *; $p<0.01$: **; $p<0.001$: ***).

3.3 Results

3.3.1 Measuring cortical activity across multiple barrel-columns with silicon-probes

Rodent whisking behavior develops in a short time window two weeks after birth. The study presented in Chapter 2 revealed that sensory-evoked activity develops in a layer-specific manner around P13, including changes in responsiveness and an increase in stimulus selectivity. In this study, we characterized in further detail the response properties of developing mouse bar-

rel cortex by employing single- and multi-whisker stimuli in three defined age groups: before eye opening and whisking onset (P10-12), during the critical period (P13-16) and afterwards (P17-28).

We recorded neuronal activity by inserting silicon-probes into barrel cortex of lightly anesthetized mice between postnatal day (P)10 and P28. We could reliably measure activity from the C1 and C2 barrel columns (**Figure 3.2**) while stimulating one or two whiskers with high temporal and spatial precision with our galvanometer-driven whisker stimulation system (see Chapter 2 and Appendix A). Our stimulation protocol consisted of single whisker stimuli with increasing stimulus intensity (**Figure 3.1A**), single whisker paired-pulse stimulation with varying inter-stimulus intervals (ISI; **Figure 3.1B**), and dual-whisker stimulation where we sequentially deflected the C1 and C2 whiskers with varying ISIs (**Figure 3.1C**). This diverse stimulus set allowed us to study the developmental profile of spatiotemporally distinct sensory-evoked responses in lightly urethane-anesthetized mice.

3.3.2 Layer-specific sensory-evoked response modulation with increasing stimulus intensity

First, we asked whether single whisker deflections with increasing stimulus intensity would result in a consistent increase in sensory-evoked activity across layers in the three defined age groups. We analyzed the multi-unit activity (MUA) across all layers and age groups by subdividing the response into an early (0-50 ms) and late (50-200 ms) window after each single whisker deflection (**Figure 3.3A**). We found that 50µm deflections of a single whisker (1 cm distance from the snout) resulted in barely detectable sensory-evoked responses (<50 spikes/s) across all layers. As expected, an increase in stimulus intensity resulted in an increased spike rate and we could detect layer-specific changes in response profiles for the early and late response across development. For the early time window, responses in L2/3 and L4 increased with stimulus intensity but started to plateau for deflections >250 µm. In L5 and L6 however, responses displayed a linear increase in responsiveness reaching significance when comparing the P10-12

and P17-28 age groups (**Figure 3.3B**). For the late response window, responses in L2/3 and L4 in the P10-12 age group was on average larger than the early response (**Figure 3.3C**). In the P13-16 and P17-28 age groups, these responses were significantly decreased compared to the P10-12 age group. Sensory-evoked responses after single whisker deflections in L5 and L6 did only display a significant decrease for the strongest stimulus when comparing the P10-12 and P17-28 age groups for the late component.

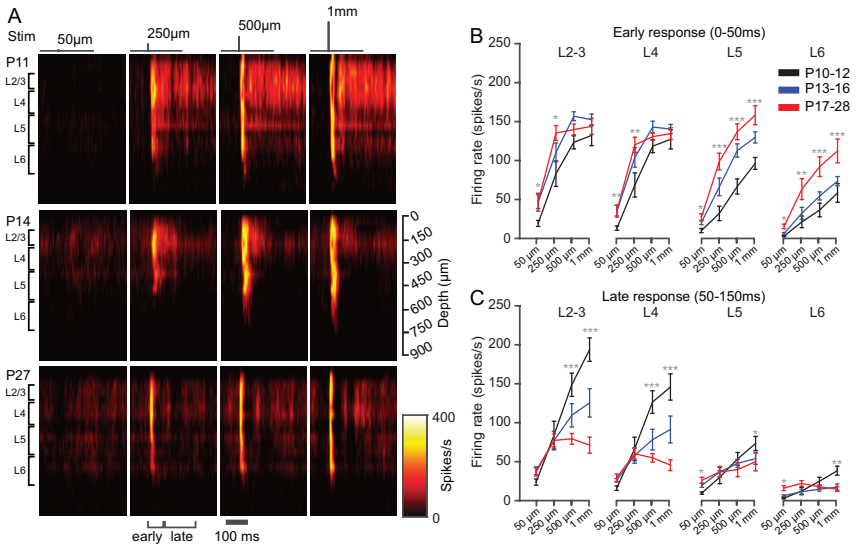

Figure 3.3: Cortical representation of single-whisker deflections with increasing stimulus intensity: (A) Heatmaps showing MUA in the principal column (C1) after single whisker deflections with varying stimulus intensity. Examples from a P11, P14 and P27 mouse. (B): Quantification of the early (0-50 ms after stimulus onset) mean firing rate for all stimulus intensities and layers. (C) Quantification of the late (50-150 ms after stimulus onset) mean firing rate for all stimulus intensities and layers. Data points are mean ± s.e.m. (n=18 mice, 6 mice per age group). Statistics: Kruskal-Wallis test followed by Dunn-Sidak's post hoc correction between the P10-12 and P17-28 age groups ($p<0.05$: *; $p<0.01$: **; $p<0.001$: ***).

Taken together, these findings indicate that responses to stimuli with increasing stimulus intensity are differentially modulated across layers and age groups: whereas responses in L2/3 and L4 showed a plateau-like increase in responsiveness for the early time window, which was similar across age groups, responses in L5 and L6 increased linearly in a intensity-dependent fashion. The increase in firing rates in L5 and L6 was significantly stronger the P17-28 age group compared to the P10-12 age group. For the late component, firing rates in L2/3 and L4 were strongly intensity-dependent in the P10-12 age group, whereas the showed no such effect

for the P17-28 age group. In L5 and L6, however, no such intensity-dependent changes across development could be detected in the late response window.

3.3.3 Cross-columnar spread is increased with stimulus intensity

Next, we addressed how sensory-evoked activity propagates across cortical columns with increasing stimulus intensity. Based on findings presented in Chapter 2, we already reported that during postnatal week 2-4, sensory-evoked responses increasingly propagate to the neighboring barrel column. Here, we analyzed the impact of increasing stimulus intensity on lateral sensory-evoked propagation from the principal to the neighboring barrel column (**Figure 3.4**). We normalized mean MUA for the first 50 ms after stimulus onset for the neighboring barrel column to the response in the principal column. We detected a significant increase in the mean MUA in the neighboring column with increasing stimulus intensity for L2/3, L4 and L5 (**Figure 3.4B**). As mean responses to stimuli $\leqslant$ 50 µm were barely detectable, mean MUA in the neighboring barrel column was nearly identical to the principal barrel column firing rate ($\sim$ 100% of normalized response).

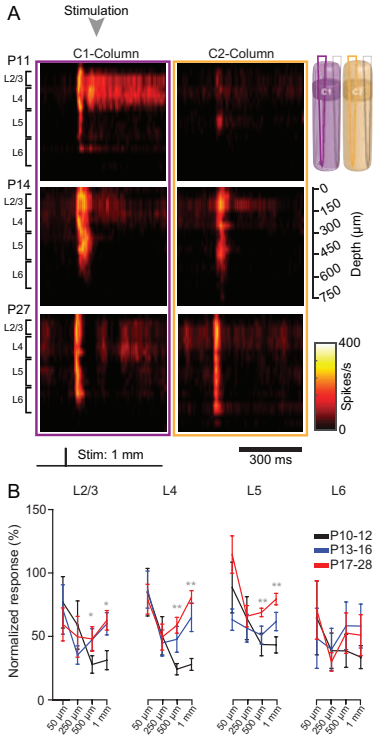

Figure 3.4: Cross-columnar spread of sensory-evoked responses with increasing stimulus intensity: (A) Heatmap showing MUA in the principal (C1) and neighboring (C2) barrel column after 1 mm deflections. Examples from a P11, P14 and P27 mouse. Responses for the first 500 ms are shown. (B) Quantification of the sensory-evoked activity in the neighboring barrel column normalized to the principal column firing rate (0-50 ms after stimulation). Data points are mean $\pm$ s.e.m. (n=18 mice, 6 mice per age group). Statistics: Kruskal-Wallis test followed by Dunn-Sidak's post hoc correction between the P10-12 and P17-28 age groups (p<0.05: *; p<0.01: **; p<0.001: ***).

We conclude that during postnatal development, cross-columnar spread of sensory-evoked activity becomes larger in L2/3, L4 and L5. Stimuli with stimulus intensity >250 µm are required to elicit these cross-columnar activation profiles in the neighboring column.

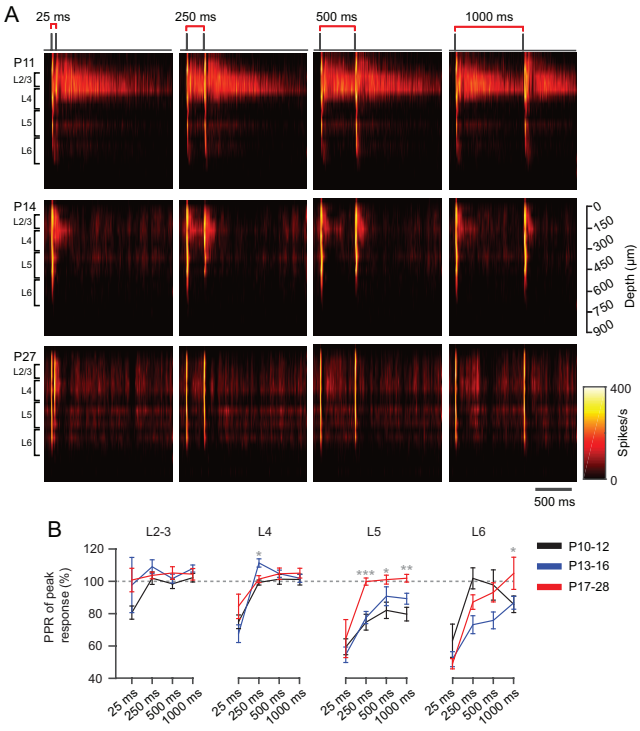

Figure 3.5: MUA response profiles to paired-pulse stimuli: (A) Heatmaps showing MUA in the principal (C1) column after paired-pulse stimulation with varying inter-stimulus intervals (ISIs). Examples from a P11, P14 and P27 mouse. (B) Quantification of the paired-pulse ratio (PPR) of the detected peak response after stimulation. Data points are mean ± s.e.m. (n=18 mice, 6 mice per age group). Statistics: Kruskal-Wallis test followed by Dunn-Sidak's post hoc correction between the P10-12 and P17-28 age groups ($p<0.05$: *; $p<0.01$: **; $p<0.001$: ***).

3.3.4 Layer-specific facilitation of sensory-evoked responses after paired-pulse stimulation

Delivering two well-timed whisker deflections has been reported to facilitate sensory-evoked intracellular depolarization of neurons in mice younger than P13 (Borgdorff et al., 2007). We therefore investigated if and how this facilitation is represented in MUA across cortical layers. We applied paired-pulse stimuli with intervals between 25 ms and 1 s and analyzed the ratio of the second and first response peaks across layers (**Figure 3.5**). Sensory-evoked responses showed an elevated late response component in L2/3 and L4 as already seen in the single pulse data, lasting more than one second (**Figure 3.5A**). Calculating the paired-pulse ratio (PPR) of the peak responses of the first and second stimulus (PPR=R2/R1) showed no facilitation across layers. We could only detect a significantly reduced PPR in the P10-12 age group compared to the P17-28 age group in L5 for ISIs > 25 ms (**Figure 3.5B**).

We further analyzed the response dynamics to paired-pulse stimuli by calculating the PPR of the two pulses for the early and late response windows for stimuli >25 ms (as time windows

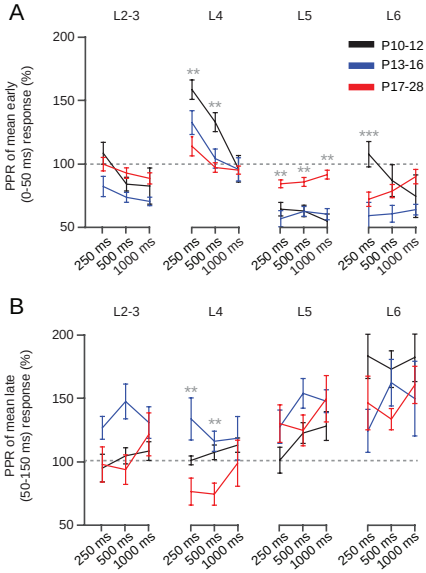

Figure 3.6: Paired-pulse ratios of the early and late response components across cortical layers: (A) PPR of the mean early evoked response for paired-pulses of 250 ms, 500 ms and 1000 ms ISI. Dashed line indicates a PPR of 1 (in %). (B) PPRs for the late evoked response. Data points are mean ± s.e.m. (n=18 mice, 6 mice per age group). Statistics: Kruskal-Wallis test followed by Dunn-Sidak's post hoc correction between the P10-12 and P17-28 age groups ($p<0.05$: *; $p<0.01$: **; $p<0.001$: ***).

would otherwise overlap). For the early response window, PPR was significantly higher in L4 for the P10-12 age group compared to the P17-28 age group for the 250 ms and 500 ms ISIs, respectively. In L5, however, PPR of the early response was significantly higher for all ISIs for older mice. For the late response window, we could only detect a significantly increased facilitation in L4 but not the other layers (**Figure 3.6B**). Although in general, overall facilitation was larger for L5 and L6 compared to L2/3 and L5.

In conclusion, peak response PPR only significantly increased in L5 across development. Further analysis of the responses for the early and late response window revealed that especially for the early window, responses are increasingly facilitated in L4, but strongly depressed in L5 when comparing the P10-12 and P17-28 age groups. Contradictory the reported facilitation of intracellular depolarization levels by Borgdorff et al. (2007), we could not detect a consistent facilitation on the MUA level.

3.3.5 Sequential dual-whisker stimulation elicits distinct barrel-specific activation profiles

To further investigate the increase in sensory-evoked cross-columnar activation profiles, we performed sequential stimulation of the C1 and C2 whiskers with varying inter-stimulus in-

tervals (see **Figure 3.1C**). These activation sequences resulted in differential activation profiles

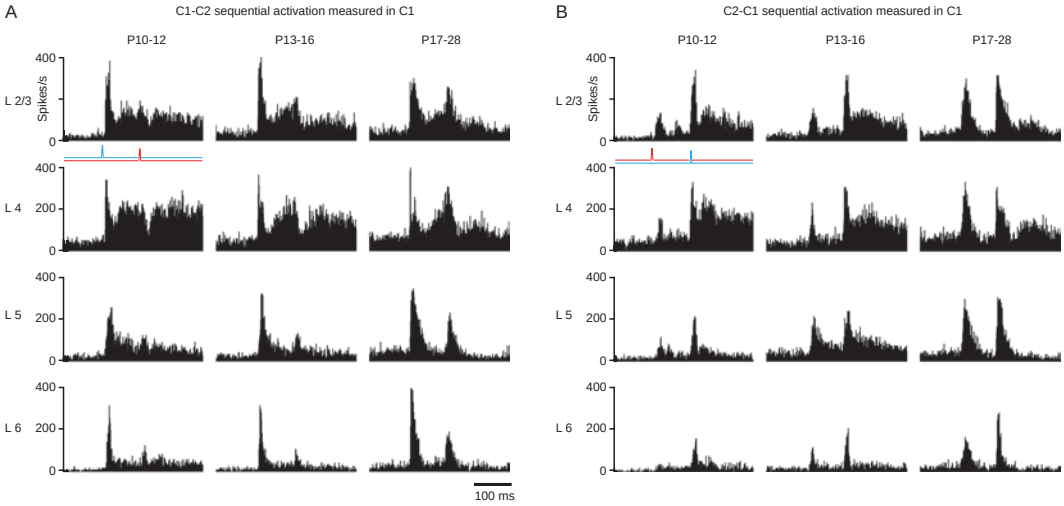

Figure 3.7: Intra-columnar representation of sequentially activated barrels: (A) Pooled average multi-unit activity across cortical layers and age groups for sequential stimulation of the C1 and C2 whisker, measured in the C1 barrel column. For each animal, we selected four representative electrodes corresponding to superficial L2/3 and the centers of L4, L5 and L6. (B) Pooled average multi-unit activity across cortical layers and age groups for sequential stimulation of the C2 and C1 whisker, measured in the C1 barrel column.

across development. Sequential activation of the C1 and C2 whisker showed a strong response in the C1 barrel column for the C1 deflection. The response to the C2 deflection was barely detectable in the P10-12 age group across all layers. Especially in L4, C2 deflections (after the C1 deflection) would result in decreased MUA in the P10-12 and P13-16 age groups (see mean MUA responses in L4 (**Figure 3.7A**). In animals older than P16, a clear response peak from the C2 deflection was visible in the MUA of the C1 barrel-related column for stimulation with ISI $>$ 50 ms (in **Figure 3.7**, only 100 ms ISIs are shown as a representative example). We could therefore detect a clear increase in the C2-evoked MUA reported in the C1 barrel after sequential C1->C2 stimulation across development. The response to the C2 deflection was not visible in the P10-12 age groups in L5 and L6, but showed increased responses in the P17-28 age group.

Sequential C2->C1 stimulation would lead to differential activation profiles compared to C1->C2 stimulation (**Figure 3.7A, B**). Interestingly, if the sequence was reversed, meaning that C2 was stimulated before the principal barrel, sensory-evoked C2 responses were detectable in

the C1 barrel already in the P10-12 age group (as opposed to the other case). Furthermore, the peak responses of the C1 activation would be slightly smaller compared to the opposite C1->C2 activation. For the P17-28 age group, C2->C1 sequential stimulation would result in nearly identical MUA peak responses (**Figure 3.7B**). These differential activation profiles indicate that responses to the neighboring barrel column are suppressed if the principal barrel column is first stimulated in young animals. If the neighboring barrel is first stimulated, responses are reported in the principal barrel and do not lead to suppressive effects across all developmental age groups. We conclude that sequential activation of the principal and neighboring barrel columns lead to differential activation profiles during development, so that sensory-evoked responses are suppressed when the neighboring barrel is stimulated after the principal barrel before the onset of whisking.

3.3.6 Sequential dual-whisker stimulation differentially activates single units during development

Next, we wanted to address how single-unit (SU) response profiles change across development for these sequential stimuli, as the MUA data suggests differential activation profiles across development. We performed multi-channel spike sorting and isolated a total of 737 SUs in 15 animals (n=5 animals per age group; P10-12: 236 SUs, P13-16: 254 SUs, P17-28: 247 SUs; also see Materials and Methods of Chapter 2 for a detailed description). As previously reported, we assigned the isolated SUs to the recording site for which the waveform amplitude was maximal. Furthermore, in the P17-28 age group, we could discriminate between putative excitatory (EXC) and putative inhibitory (INH) SUs based on their waveform asymmetry and spike width, of which 22.7% were identified as putative INH SUs (56 out of 247 units, also see **Figure 2.6A** in Chapter 2). Response profiles of SUs showed a diverse set of response profiles across development (**Figure 3.8**). In animals younger than P13, SUs typically responded only for activation of the principal barrel column (representative example in **Figure 3.8A**), followed by an elevated late response component as reported for the MUA activity profiles. During the critical period,

SU responses shifted and two types of SU spiking profiles could be identified: SUs showing spiking for only their principal barrel column, followed by strong reduction in spike rates, independent of the stimulation sequence (**Figure 3.8B**) or SUs that increasingly responded to both the neighboring and principal whisker, if the neighboring whisker was activated first. In animals older than P16, spike precision and peak responses increased for principal barrel stimulation, independent of the stimulation sequence (**Figure 3.8B**). Putative INH SUs showed the most distinct activation profiles (see example in **Figure 3.8D**). For sequential stimulation of the principal whisker, followed by its neighbor, INH SUs generally responded with high spike precision to the principal whisker but not the neighbor. For the opposite case (neighboring whisker first, followed py principal whisker), INH SUs showed responses to the neighboring whisker, followed by a reduced peak response to the principal whisker stimulation ((**Figure 3.8D**, right). Importantly, most of the INH SUs showed a strong reduction in spike rates for these activation sequences for 20-30 ms, followed by a short increase of firing rate for 50-100 ms.

Based on these preliminary findings, we conclude that sequential activation of principal and neighboring barrels is represented with increased cross-columnar activity resulting in discrete whisker-specific receptive-field response properties. After the critical period, EXC and INH SUs exhibit specific activation profiles, including sequence specific modulation of spiking rates.

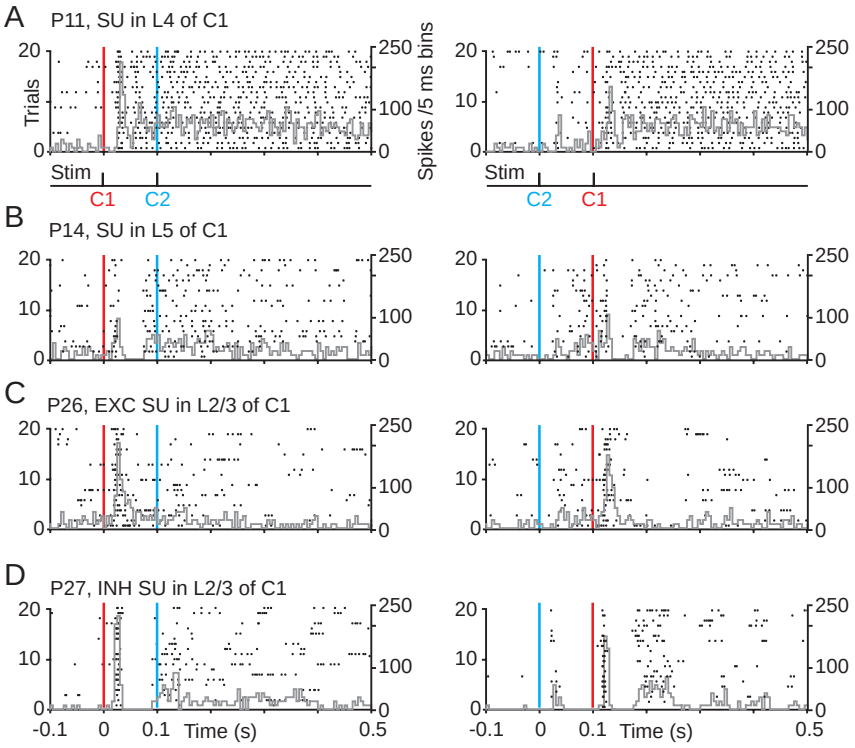

Figure 3.8: Single-unit activation profiles after sequential dual-whisker stimulation: Example PSTHs of single units for sequential stimulation with 100 ms ISI. (A) Example of an isolated single-unit (SU) in L4 of C1 in a P11 mouse. Left: Sequential C1->C2 activation evoked a strong peak for C1 but not C2 deflection. Right: C2->C1 sequential activation of the same SU in C1. Elevated evoked response is detectable for more than 200 ms after stimulation. (B) Example SU in L5 of C1 in a P14 mouse. For both C1->C2 and C2->C1 stimulation, responses to the stimulation of the neighboring whisker are barely detectable. (C) Example of an isolated putative excitatory SU in L2/3 of C1. The SU is highly responsive only for principal whisker stimulation. (D) Example of an isolated putative inhibitory unit in L2/3 of C1. The SU shows responses for both stimuli. For the C2->C1 stimulation, the SU shows strong reduction in firing rate, followed by an elevated late peak around 100 ms after stimulation (right). PSTHs (gray) and spike rasters (black dots) are shown. Data of 20 trials per condition. Whisker stimulation onset indicated in colors (C1: red, C2, cyan)

3.4 Discussion

In summary, we have characterized the changes in response profiles of whisker-specific responses in barrel cortex of mice between P10 and P28. Single whisker deflections with increasing stimulus intensity are differentially modulated across layers and age groups: whereas responses in L2/3 and L4 showed a plateau-like increase in responsiveness for the early time window, which was similar across age groups, responses in L5 and L6 increased linearly in a intensity-dependent fashion. The increase in firing rates in L5 and L6 was significantly stronger

the P17-28 age group compared to the P10-12 age group. For the late component, firing rates in L2/3 and L4 were strongly intensity-dependent in the P10-12 age group, whereas the showed no such effect for the P17-28 age group. In L5 and L6, however, no such intensity-dependent changes across development could be detected in the late response window. Further whisker-specific changes include the reduction in facilitation when delivering two well-timed stimuli in L4 but an increase in the immediate early response in L5. Sequential activation of two neighboring barrels with varying ISIs resulted in distinct activation patterns both on the multi-unit and single-unit level. Sequential activation of the principal and neighboring barrel would result in negligible responses for the neighbor. During the critical period, in parallel to increased cross-columnar activation, deflection of the neighboring whisker after the principal whisker started to evoke responses on the MUA level in the principal barrel column. Isolated single units showed progressively more diverse activation patterns with age, indicating refined processing of these inputs. Putative INH units exhibited sequence-specific activation patterns and showed diverse response profiles warranting further examination. Together these findings provide a first characterization of maturation of intra- and cross-columnar activity at the onset of active whisking behavior.

Neurons in the rodent barrel cortex are known to be extremely sensitive to velocity (Shoykhet et al., 2000) and acceleration (Temereanca and Simons, 2003). It has been previously shown that synaptic responses to stimuli with increasing stimulis intensity are modulated in a layer-specific manner (Wilent and Contreras, 2004). Our results support these recent findings as neurons in superficial L2/3 and L4 show an initial linear increase in spiking rates for stimuli < 500 °/s and then show a plateau like saturation of spiking activity, also observed for awake behaving animals (Stüttgen and Schwarz, 2008). In contrast, spiking activity in L5 and L6 is increased across development, but lacks plateau like saturation as observed in superficial layers, which is in agreement with findings in rat barrel cortex (Glazewski and Barth, 2015). Interestingly, very little is known so far about the processing of stimulus intensity (and deflection velocity) in developing barrel cortex at the onset of whisking behavior. An important finding

of our study reports the pronounced reduction in the late response MUA for L2/3 and L4 with increasing stimulus intensity. We suspect that these changes are caused by maturation of local connectivity, based on changes in synapse density (Chandrasekaran et al., 2015) and local connectivity between L4-to-L2/3 and L2/3-to-L2/3 synapses (Stern et al., 2001; Wen and Barth, 2011). A further likely cause of the reduction in the late response, which is more prominent with increasing stimulus intensity, might be a result of increased activation of the inhibiory network after the critical period (Shoykhet, 2005), but warrant further investigation.

Although the overall responsiveness in L2/3 and L4 is strongly reduced after the critical period, we could detect a significant increase in the cross-columnar whisker-evoked activation of the neighboring column as previously reported (see results Chapter 2). This increase in cross-columnar activity was more notably driving neighboring barrel-column activity with increasing stimulus intensity for L2/3, L4, L5. We therefore argue that whisker-specific receptive field properties are broadened around the critical period. A likely cause of this increase in whisker-specific responses could be the increase in axonal outgrowth to neighboring barrel fields, especially for L2/3, where horizontal connectivity increases during the critical period (Wen and Barth, 2011). The exact mechanisms driving this increase in cross-columnar activation warrants further examination.

Sequential deflections of two neighboring whiskers evoked distinct response profiles during development, depending on the direction and temporal separation of the stimuli. In animals younger than P13, we could not detect responses of the neighboring whisker, if the principal whisker was stimulated first. Only a few days later around P13, we could detect small, and highly reduced spiking rates for the neighboring whisker stimulation, which then later started to increase significantly with age. These findings hint towards increased cross-columnar inhibition for mice younger than P13, which could also explain why cross-columnar spread is not present in animals younger than P13. It is important to note that mice younger than P7 show an imprecise whisker map, where information of neighboring whiskers overlaps, which is only later confined to one barrel around P7 (Mitrukhina et al., 2015). However, later during development

between P7 to P10, these responses seem to be more localized, which then spread further across barrels around P13 (Borgdorff et al., 2007). The question arises, if a transient maturation of connectivity initially leads to confined activation of local neurons that only later during development can activate neighboring barrels. We therefore see two different mechanisms that could drive the observed transient changes. First, the local thalamo-cortical inputs to L4 neurons are established, which in turn localize their dendritic arborizations to their target barrel (Espinosa et al., 2009). During this transient period, thalamocortical afferents could unspecifically innervate neighboring barrel areas during their formation and maturation which might then in turn lead to imprecise responses as reported previously (Mitrukhina et al., 2015). The initial construction of such circuitry would rely on responses to be strongly localized, which could also be driven by undiscovered mechanisms. Second, after further maturation of connectivity between L4 and L2/3 neurons (Lendvai et al., 2000; Stern et al., 2001), local networks would increasingly connect and therefore increase the probability of cross-columnar activation, as seen around P14 in L2/3 (Wen and Barth, 2011). This hypothesis could be supported by our findings that initial stimulation of the neighboring whisker, followed by the principal whisker, is already detectable around P10 indicating the possibility that a weak thalamo-cortical cross-columnar drive is present. The opposite stimulation sequence does not lead to responses for neighboring stimulation hinting towards a lack of horizontal connectivity, as only synaptic drive from local populations of neurons (and thalamo-cortical afferents) would be able to elicit responses. Further likely causes of the differential activation patterns depending on stimulation sequence could originate from putative INH single units sharpening the local receptive fields. These INH units could be a type of highly localized cellls that modulate overall network activity, depending on the sequence and spatial arrangement of multi-whisker stimuli. One such modulatory effect could lead to strong lateral inhibition across barrels (Ego-Stengel and Souza, 2005; Moore et al., 1999) and sharpen overall responses. Increasing evidence also points towards multi-whisker related sensory maps that represent more complex activation patterns (Andermann and Moore, 2006; Ramirez et al., 2014). The developmental increase of cross-columnar cross-talk and in-

creased spatiotemporal specificity of response patterns during the critical period hint towards behavior-related mechanisms that drive these changes. Which specific cell types and subsets of neurons are involved in shaping these complex response properties and what drives its maturation remain open questions for future research.

In conclusion, we have shown that processing of single- and dual-whisker stimuli in barrel cortex changes in a layer-specific fashion at the onset of whisking behavior. These changes include increased temporal precision in responsiveness, cross-talk across barrel columns as well as response specificity to sequential whisker deflections. These findings will aid in understanding the maturation of sensory-evoked activity in developing rodent barrel cortex.

The philosopher is in love with truth, that is, not with the changing world of sensation, which is the object of opinion, but with the unchanging reality which is the object of knowledge.

Plato, *Truth and Reality*

4

General Discussion

The results presented in this thesis characterize the developmental profile of sensory-evoked activity in barrel cortex of mice between P10 and P28, including the short time window around P13 when animals open their eyes and start to actively explore their environment. These findings, as presented in Chapters 2 and 3, provide insights into the functional maturation of barrel cortex, including layer-specific changes in multi-unit activity, changes in response adaptation and increase in response selectivity to axial versus lateral whisker stimuli. Moreover, this thesis also provides insights on the maturation of cross-columnar refinement of sensory-evoked activity and the increase in spatiotemporal precision after single or multi-whisker deflections. In this last chapter, I will reflect on how these results integrate into the current literature and discuss their immediate implications for future research.

4.1 Layer-specific maturation of columnar activity

The findings of layer-specific maturation profiles presented in Chapter 2 are in close agreement with recent literature demonstrating rapid functional changes of barrel cortex activity within a few days in the critical period of L2/3 maturation around P13. These observed changes include the sparsification and decorrelation of spontaneous L2/3 population activity (Golshani et al., 2009), sharpening of evoked temporal spiking profiles (Ikezoe et al., 2012), and changes of signal flow across large portions of the cerebral hemispheres (Quairiaux et al., 2011). In Chapter 2 we showed that sparsification of sensory-evoked activity follows the same developmental profile as spontaneous L2/3 activity (Golshani et al., 2009). This aging-related sparsification can be explained, at least in part, by changes in intrinsic neuronal properties, especially a pronounced progressive decrease in input resistance (Maravall et al., 2004). Further likely causes include changes in synapse density in L2/3 (Chandrasekaran et al., 2015), plasticity-induced changes of L4-to-L2/3 and L2/3-to-L2/3 synaptic connectivity (Stern et al., 2001; Wen and Barth, 2011), maturation and pruning of thalamo-cortical inputs (Yu et al., 2012), and maturation of the inhibitory circuitry (Zhang et al., 2011). These changes in overall responsiveness were also reflected in the changes in response adaptation upon repetitive stimulation. L2/3 and L4 showed an in increase in response adaptation which could be explained by the changes in overall connectivity as mentioned above. Response profiles of multi-unit activity in L5 and L6 increased with age, opposite to the effects observed in superficial layers. More specifically, whereas superficial layers showed facilitation before the critical period, which then turned into slight depression, deep layers showed pronounced adaptation at an early age, which then became less prominent in older animals. This observed layer-specificity could imply that deep layer processing of whisker-evoked activity is different from superficial layers. As introduced in subsection 1.2.3, VPm and POm target specific subsets of neurons in L2/3, L4,L L5 and L6. Furthermore, the local connectivity motifs in adult circuitry display reciprocal output streams from superficial to deeper layers (Petersen, 2007; Avermann et al., 2012). We suspect that local connectivity of L2/3 to L5 pyramidal neurons is strengthened during the critical period, leading

to the observed increased peak responses and reduced adaptation. These response profiles could lead to improved transmission of whisker-evoked activity to other cortical areas. How these observed layer-specific response-profiles are anatomically defined through connectivity motifs and how they change during development, remains unclear.

In agreement with the layer-specific maturation of responsiveness, we could further show in Chapter 3, that these changes include whisker-specific changes during the critical period. Single-whisker evoked stimuli with increasing stimulus intensity modulated MUA in a layer-specific fashion across development. In general, we could detect a plateau like saturation of responsiveness for increasing stimulus intensity for the early response window (0-50 ms) in L2/3 and L4, while responses increased linearly in L5 and L6. On the other hand, response dynamics in the late window (50-150 ms) showed a linear increase in the P10-12 age groups for L2/3 and L4, but a plateau-like saturation for animals older than P16. Interestingly, these dynamics were not observed for L5 and L6, where we found a clear linear intensity-dependent increase in firing rates for all age groups. We suspect that these response dynamics are in part a result of the overall maturation of the circuitry and strengthening of thalamo-cortical inputs. We further suspect an increased modulation of the network through excitation-inhibition balance a likely cause of sharpening of spatiotemporal response profiles (Zhang et al., 2011).

Taken together, we argue that these layer-specific changes during development indicate a possible maturation motif that is different for superficial and deep layers. However, we need to distinguish between activation profiles elicited by repetitive stimuli as presented in Chapter 2 compared to single- or paired-pulse stimuli as presented in Chapter 3. Repetitive stimuli have a higher likelihood to *saturate* network activity by continuously driving depolarization of cells. As a result overall network activity across layers is differentially modulated compared to single pulse responses. These differences could explain why activity in the deeper layers for single pulse deflections shows no age-related maturation compared to the superficial layers. The question remains what physiological properties or entities drive these layer-specific changes.

4.2 Layer-specific maturation of cross-columnar activity

Our silicon-probe measurements allowed us to record sensory-evoked responses from two neighboring barrel columns. An evident change in the overall response profiles was the increased inter-columnar spread of sensory evoked activity, reaching beyond the principal barrel column. Using voltage sensitive dye imaging, a previous study already hinted towards an increase in the cortical spread across development (Borgdorff et al., 2007). As we have shown both in Chapter 2 for repetitive stimuli and further investigated for single stimuli with increasing stimulus intensity in Chapter 3, it is evident that activity spreads further across barrel columns, especially for L2/3 and L4. The most obvious mechanism driving this increase in cross-columnar activity might arise from the maturation of horizontal connectivity and increase in receptive field properties of single neurons (Clancy et al., 2015; Wen and Barth, 2011). We further could show that sequential activation of two neighboring whiskers resulted in increased cross-talk among barrel columns at the onset of whisking behavior. Notably, sequential activation of the neighboring barrel column before the principal column elicited activity in the principal barrel column whereas the opposite activation profile does not lead to responses of the neighbor. These differential activation profiles were also observable in single units and were most profound for putative INH units. These important observations need further investigation as they could potentially aid in explaining the changes in receptive field properties of single neurons that have also been reported in Chapter 3. Until now, very little is known about the development of complex receptive fields as they have been observed for neurons in L2/3 and L5 (Clancy et al., 2015; Ramirez et al., 2014). Our data hints towards the possibility that the development of receptive field properties is linked to the development of whisking behaviors. Whether these mechanisms are driven intrinsically or extrinsically and whether specific cell types and network components are involved are important aspects that could to be further investigated in future research.

4.3 Development of response selectivity to axial or lateral whisker deflections

Our novel stimluation paradigm allowed us to study the development of selectivity for axial or lateral whisker stimuli across all cortical layers. We could demonstrate that response selectivity to these discrete stimuli emerges at the critical period of L2/3 network maturation. We found an increase in the proportion of stimulus-selective neurons in L2/3, L5 and L6 in animals older than P16 compared to animals younger than P13. We could also show that locally intermixed populations of neuron in L2/3 show selectivity for either axial or lateral stimuli. These developmental changes in response selectivity have also been observed for visual cortex where an increase in direction selective cells was observed around eye-opening (Rochefort et al., 2009). However, the development of neuronal selectivity to gratings and bars in the visual cortex most likely undergoes different maturation processes compared to response selectivity to different whisker forces in the barrel cortex (Clemens et al., 2012; Hoy and Niell, 2015). Studies in adult mice have shown that axial and lateral whisker-forces are important features for object localization (Pammer et al., 2013; Quist et al., 2014). It is therefore not surprising that the development of response selectivity to axial versus lateral forces that we found during postnatal week 3 occurs in parallel to the start of active tactile exploration. Response selectivity to these stimuli thus might be an important aspect for the young mouse explorer. Notably, the response selectivity to axial and lateral whisker forces only represents a very limited subset of the possible repertoire of receptive field properties exhibited by neurons in barrel cortex. Recent studies have found that neurons in L2/3 show whisker-specific receptive fields different from their cortical column identity (Clancy et al., 2015) and that the optimal stimulus can even consist of spatiotemporally confined stimuli from multiple whiskers (Ramirez et al., 2014). Future research could dissect the wiring mechanisms leading to functional sensory coding in more detail and also compare these findings to other sensory areas like visual cortex. Their comparison might lead to the description of a common sensory connectivity motif for sensory coding.

4.4 Outlook

In this thesis I described in detail the functional changes of circuit function underlying touch processing in mouse barrel cortex. The exploration of the core mechanisms that lead to observed changes in sensory-evoked activity in barrel cortex might aid greatly in better understanding mechanisms observed in adult circuitry. We focused on a first description of the functional changes in sensory-evoked activity because the basic response properties during early development have not been fully characterized.

Before we can dissect more distinct circuit mechanisms involved in barrel cortex maturation, we first had to investigate the underlying response properties of the undisturbed system. However, the work presented here leads to many questions: what mechanisms drive the changes in neuronal responses that seem to happen only in a few days around the onset of active whisking and are believed to be internally mediated (Golshani et al., 2009)? Are these changes in spontaneous and sensory-evoked activity a result of the maturation of local connectivity? Is the integration of specific interneurons into the local circuitry or the expression of specific neuromodulators driving this change? What are the mechanisms driving the differential maturation of responsiveness in superficial and deep layers? - To answer these questions, many possible experiments could be performed, including the establishment of chronic imaging, pharmacological manipulations and careful analysis of the communication between brain-regions inducing whisking behaviors.

Chronic investigation of cortical circuit maturation

The developing neocortex is a highly dynamic and changing system. Therefore, it is challenging to establish robust techniques to investigate developing neural activity chronically over several days or weeks without disturbing its maturation. One of the main problems arising when trying to chronically implant a window to investigate neurons in developing neocortex concerns the expansion of brain tissue and increased bone growth of the cranium. Until now, only one research group established chronic investigation of dendritic morphology in the desired devel-

opmental time window betwen P10 to P14 (Cruz-Martin and Portera-Cailliau, 2014). The report mentions an extensive list of issues that can arise from the implantation of chronic glass windows in mouse pups. One such issue concerns the acceptance of the treated pups by the litter, as any stressor leads to cannibalization of pups. Cruz-Martin and Portera-Cailliau (2014) reported extensively on this issue and also argued that increasing the acceptance rate relies not only on minimizing the impact of the surgery but also on the usage of surrogate mothers. Taking these issues into consideration we performed pilot experiments to implement a chronic imaging approach by a thinned-skull preparation in mice genetically encoding calcium indicators in L2/3 of barrel cortex (**Figure 4.1**). The thinned skull approach would result in a less severe surgical intervention and led to higher acceptance rates of the pups by the mother. The thinned skull approach would allow to perform wide-field calcium imaging, a technique commonly used to visualize cortical sensory map dynamics with high temporal fidelity (Minderer et al., 2011). The thinned skull approach leaves the cranium intact and has the advantage to greatly reduce inflammatory responses resulting from chronic window implants. Based on these advantages we recently achieved a thinned-skull preparation over a complete brain-hemisphere (**Figure 4.1A, B**). As seen in Figure **Figure 4.1C**, mice could be used for more than 10 days after surgery. One problem arise from the implanted dental cement ring that induced bending of the underlying bone structure and in most cases lead to inflammation of the neural tissue beneath the window, warranting further improvements. A further technical limitation concerns the careful choice of calcium indicators and their expression in developing neural tissue. Recent advances in the field allow to specifically target subsets of neurons through an intersectional triple-transgenic approach (Madisen et al., 2015). This technique allows, for example, to exclusively express a specific calcium indicator in excitatory neurons in L2/3. The intersectional approach relies on the timely activation of indicator expression through pharmacological induction of trimethoprin (TMP) (Madisen et al., 2015). The induction is reported to result in sufficient expression levels of the indicator 7 to 14 days after treatment. Unfortunately, we were not able to detect calcium signals for mice driving calcium indicator expression under the

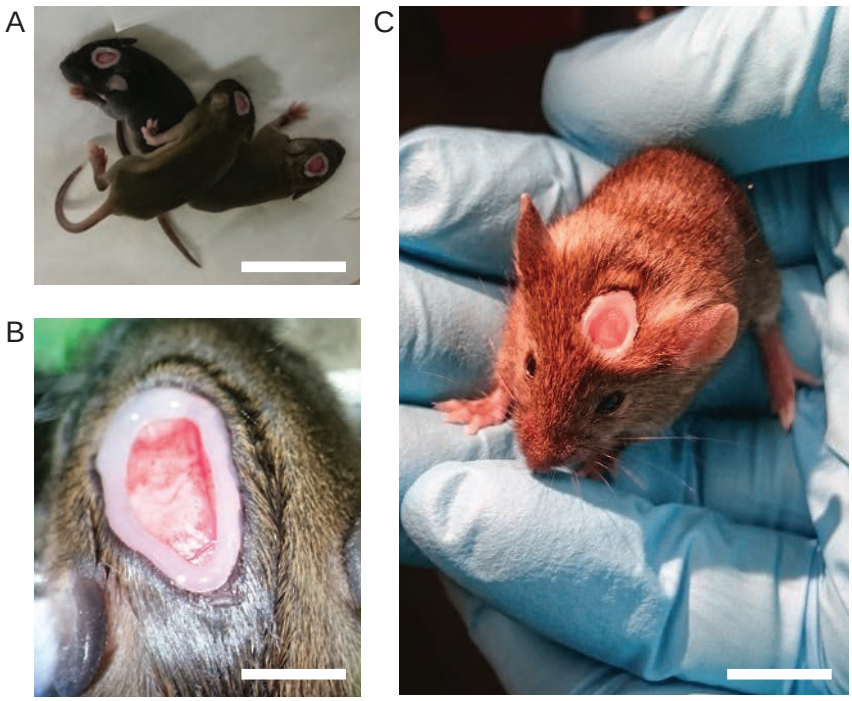

Figure 4.1: Chronic thinned skull preparations in juvenile mice: **A:** Example image of a litter of three mice with a chronically exposed thinned skull preparation at P8. These mice express YCX 2.6 in L2/3 of neocortex (as described in Madisen et al. (2015)). Scalebar: 6 cm. **B:** Close-up of the thinned skull chronic window directly after surgery in a P8 pup. Scalebar: 1cm. **C:** Snapshot of the same mouse as presented in B, 10 days after surgery. The chronic thinned skull preparation was intact and untouched. However, bone regrowth induced inflammation in the center of the chronic window (as seen by two pale white spots). Scalebar: 3cm.

CamK2A-promoter when inducing mouse pups at P2 and checking for expression around P11. Future studies should therefore explore other genetical approaches. The expression of calcium indicators through the emx1-promoter for excitatory neurons (Guo et al., 2000) or the expression of calcium indicators in inhibitory interneurons through the lhx6-promoter (Lavdas et al., 1999) should facilitate successful measurements with the mentioned chronical preparation. Chronic investigation of neural circuit dynamic maturation is surely an important topic that should be investigated. Especially the wide-field approach will be a suitable tool to better understand the maturation of multi-sensory integration of whisker-induced stimuli.

Cortical development of sensory-motor integration in active whisking behaviors

In mice, active exploratory behavior, including uncoordinated movements of the vibrissae, is already observable as early as 10 to 14 days after birth (van der Bourg et al., 2016; Grant et al.,

2012). These uncoordinated movements gradually increase until the animals exhibit rhythmic bilateral whisking with the typical frequency range of 5-10 Hz (Welker, 1964; Landers and Philip Zeigler, 2006). The underlying mechanisms leading to active whisking sensation are not well understood. It is not clear how connectivity between primary somatosensory and motor areas develops, how their connectivity impacts behavior and what functional circuits need to mature for active whisker-evoked somatosensation and behavior. In recent years, an intriguing connectivity motif for a disinhibitory sensory circuit has been described for both visual (Kuhlman et al., 2013) somatosensory cortex (Lee et al., 2013). It might play an important role in sensory perception as it impacts circuit function during whisking behaviors and vision. During active whisking, neurons in S1 are modulated by long-range projecting neurons from primary vibrissal motor cortex (vM1). These neurons strongly recruit VIP-expressing GABAergic interneurons, which in turn preferentially inhibit somatostatin-expressing (SOM) interneurons. SOM-expressing interneurons preferrably target distal dendrites of pyramidal cells (Lee et al., 2013). During whisking, this vM1-mediated disinhibitory circuit leads to disinhibition of SOM cells resulting in a higher probability for pyramidal neurons to be active during somatosensation. This disinhibition could therefore directly influence sensory processing in S1. To bridge the gap between observed changes in exploratory behavior during development and circuit function, future studies should investigate the maturation of this disinibitory circuit as it potentially has great impact on active sensation behaviors. The first goal to untangle this important circuit would be to get a better understanding of when the projections from vM1 neurons to VIP-expressing interneurons are formed. Recent evidence suggest, that during early development limb movements and muscle twitches on the whisker pad are not mediated by motor cortex but spinal circuits (Ackman et al., 2014). Tracing studies, in combination with immunohistochemical labeling of VIP-expressing interneurons during different developmental time-points could shed light on this issue. Another important aspect concerns the impact that this projection has on local cortical computation, including the response properties of VIP-expressing interneurons. A direct applicable approach is to bolus load local populations

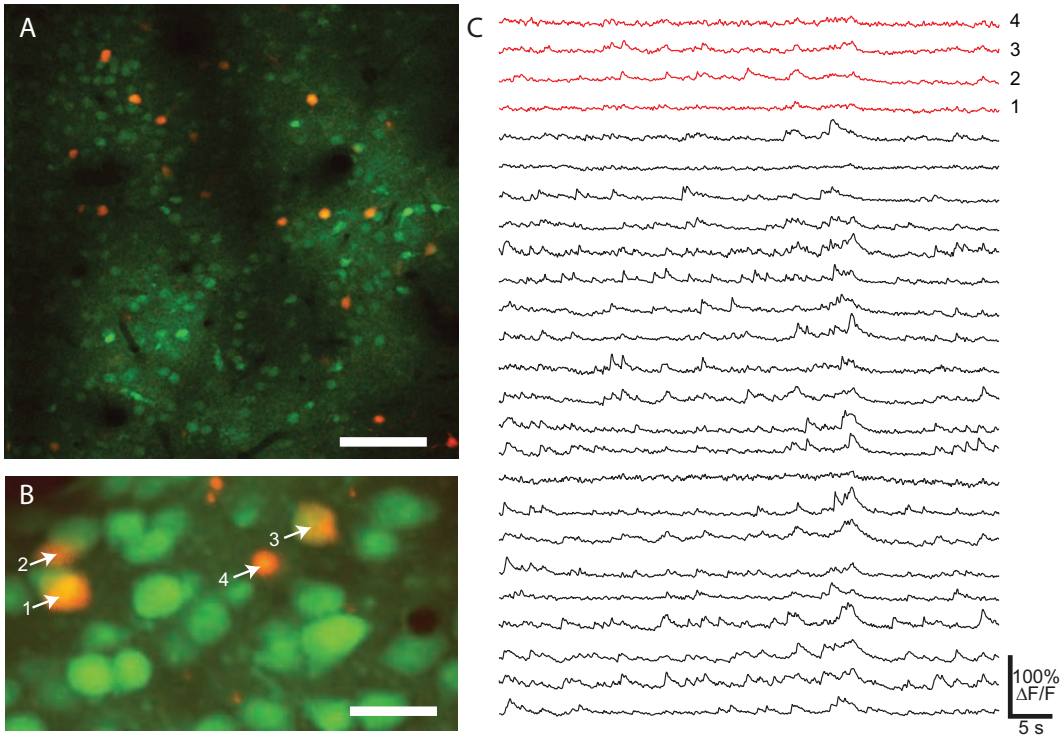

Figure 4.2: Imaging neural responses of VIP- expressing interneurons in local populations of L2/3 of barrel cortex: **A:** Example image of a VIPxtdTomato mouse after bolus loading of OGB-1 AM in L 2/3 of barrel cortex, aged P10 (preliminary, unpublished data). Scalebar: 150 µm **B:** Maximum intensity projection of a small subpopulation of cells labelled with OGB1-AM in green and the fluorescence signal of VIPxtdTomato in red. Scalebar: 20 µm **C:** Spontaneous activity of intermixed populations of VIP- and non-VIP-expressing neurons in developing mouse barrel cortex. Most of the neurons in this example exhibit a localized synchronized spontaneous event. Identified VIP-positive labeled cells do not participate in this spontaneous event. Additionally these neurons exhibit much smaller overall calcium transient peaks compared to the other cells.

of neurons with OGB-1 in L2/3 of mice expressing a fluorescent marker for VIP-expressing interneurons at different developmental stages. Transgenic mice expressing tdTomato in VIP-expressing interneurons are commonly available. We therefore tested these mice and performed pilot experiments in young mouse pups (P8-P10) and could measure spontaneous and sensory-evoked neural responses in these intermixed populations (**Figure 4.2**, only spontaneous data shown). These pilot experiments have been conducted during anesthesia and will probably not capture the response dynamics during active whisking behaviors. Therefore, recording of neural activity and whisking in awake mouse pups would be the ideal experimental condition. Despite the disadvantage of imaging in the anesthetized condition, the preliminary data pre-

sented in **Figure 4.2C** hints towards differential spontaneous activity profiles of VIP-expressing interneurons and other cells. In young animals, spontaneous synchronized activity occurs with high probability (Golshani et al., 2009). Interestingly, the recorded sub-populations of VIP-expressing interneurons did not seem to participate in these synchronized spontaneous events. These differential activity profiles could indicate that these inhibitory neurons are differentially connected and embedded in the local network. Measuring spontaneous and sensory-evoked response profiles in the anesthetized condition could shed light on how these sub-populations are activated. Furthermore, stimulation of the vibrissal motor cortex area, while imaging these interneurons before, during and after the onset of active whisking could aid in identifying functional connectivity motifs.

The study of developing rodent barrel cortex offers the opportunity to bridge the gap between neural circuit computation and associated behaviors. The development of new tools such as the targeted expression of calcium indicators, chronic investigation of neural circuit development or labeling of subsets of the underlying whisker-related circuitry might aid greatly in better understanding how neural computation in a cortical column develops at the onset of active sensation behaviors.

A

Hardware and software implementation of galvanometer-driven whisker stimulation

Following documentation provides an overview of the underlying hardware and software design choices for the implementation of the galvanometer-driven whisker stimulation platform.

A.1 Evaluation of hardware components

The implementation of a robust and reliable whisker-stimulation system requires hardware components capable of employing small movements at high temporal precision. In recent years, piezoelectric benders have been widely used to stimulate single or multiple whiskers (Jacob et al., 2010). Other approaches include the attachment of a metallic coil to a sound speaker,

servo-drives or electro-magnets. Although some techniques can be easily implemented in a cost efficient manner, they usually lack the needed spatial and temporal precision to induce consistent whisker movements. Some of the approaches also lack the mechanical robustness for long-term experiments. When designing the galvanometer-driven whisker stimulator, we re-evaluated all commonly available hardware to overcome general limitations associated with certain hardware and decided to implement the galvo approach. Table A.1 provides an overview of the technical advantages and limitations of possible hardware components.

Criterion	Piezoelectric Bender	Electro Magnet	Sound Speaker	Mechanic Servo	Harddisk	Galvo
Cost	very high	medium	low	medium	low	high
Mechanical robustness	low	medium	medium	high	low	medium
Mechanical complexity	high	low	medium	medium	high	high
Mechanical load	very high	low	medium	very high	very low	high
Spatial dimensions	small	small	large	small	medium	medium
Theoretical frequency range	100-200 Hz	100-200 Hz	100 Hz	10-40 Hz	100-200Hz	200-500 Hz
Spatiotemporal precision	medium	high	low	low	very high	very high

Table A.1: Evaluation of stimulator implementation - Overview of the technical and mechanical limitations of different hardware components usable for whisker stimulation. Relevant analyzed criteria include mechanical robustness in relation to its complexity, possible mechanical load to induce movements and the theoretical frequency range for repetitive stimuli. Out of the presented hardware components, galvo's provide the best overall performance for chosen criteria.

Table A.1 indicates that galvo-units display the best overall characteristics to translate small objects with high spatial and temporal precision. However, galvo-units are designed to move mirrors in laser scanning systems and are therefore lacking the lateral translation component needed for whisker stimulation. Piezoelectric benders can translate objects with high mechanical load (and force compared to the other approaches) and in general incorporate the desired properties for stimulation which is also a reason why many labs have used these benders. Their main disadvantage consists of the problem of continued after-oscillations following each translation pulse (also referred to as *ringing*). These after-oscillations can be compensated for by software and hardware (Jacob et al., 2010). For stimulation in a high frequency range (>100 Hz), modulation of piezoelectric benders becomes challenging. Additionally, their metallic coil

and mechanical components can potentially induce high-pitch sound originating from different sources of electrical disturbance which could perturb experimentation with awake animals. Electro-magnets on the other hand would induce nearly soundless movement but they can only translate at low mechanical load and also suffer from current-induced after-oscillations. Sound speakers are very cost efficient and display medium to high mechanical robustness. A rather obvious disadvantage is their large spatial dimension and the generation of noise for inducing stimulation. They are also susceptible for changes in the surrounding electromagnetic field, inducing unwanted translation of the stimulated object. Mechanic servos, as used for controlling small robotic components to translate objects with high mechanical load are a possible alternative. Because their core components usually consist of gear-wheels, their theoretical movement range is very limited compared to the other approaches, making them undesirable for repetitive whisker stimulation. Hard-disk reader-arms consist of an actuator, an actuator-coil and axis, enabling them to translate along a given range quickly. They would be ideal for translating whiskers in ramp-and-hold stimuli. Their mechanical properties, however, do not allow to easily oscillate at a given target frequency. They are also not ideal for continuous stimulation because of their large dimensions and susceptibility for electromagnetic disturbances. Galvo-units on the other hand show desirable properties for all reviewed criteria: they show medium to high mechanical robustness, are capable of translating objects with high mechanical load and maintain small spatial dimensions. Another core advantage is the large frequency range the galvo-units can cover compared to the other approaches (see Table A.1). Based on the multitude of these advantages we decided to implement the galvanometer approach.

A.2 Hardware implementation

A multitude of galvanometers designed for specific applications are commercially available on the mainstream market. Their usage ranges from high-performance laser-scanning galvo-units to cheap laser-show galvo-pairs. We decided to use laser-show galvo-pairs as they are cheap and shipped with a controller board to adjust driver parameters. To drive these galvo-units with

high temporal and spatial precision, an analog driver board with high sampling rates across multiple channels (> 1 kS/s for four channels) had to be found. We decided to use an National Instruments (NI) data acquisition (DAQ)-card (see table A.2 for model number). The analog signal transmission form the board to the galvo-units is performed through NI connector cables and NI break-out boxes that can are easily accessible for attaching custom cabling.

Hardware Components		
Product	Description	Price ($)
SpaceLas ILDA 30kpps galvanometric system kit	Galvo pair	180
NI PCIE-6323	Data aquisition and driver card; 4 analog outputs, 900 KS/s	1150
2 x Connector Block (SCB-68A)	Breakout boxes for analog IO	430
2x SHC68-68-EPM Cable (2m)	Connector cables for NI Card	180
Polymicro tubes	Outer fiber bundle ID: 251 μm OD:355 μm	500
Optical fibers (Hitachi, uncoated)	Diameter: 200 μm	50
2 x Metal Body	Frame for power supply and stimulator	150

Table A.2: Whisker stimulator hardware components - Total cost is around 2640 $ USD, excluding PC and software license costs.

One of the main technical challenges that had to be overcome was the transformation of the rotational movement of the galvo-unit into a stable translational movement. We found that by using a small light-weight metal pin-connector embedded in a pole-arm on the galvo-unit arm enabled us to attach an object to induce translation. We therefore used a pin-connector and pin-head used in integrated circuit boards. These connectors are light-weight, while showing strong

coupling of the pin and socket with high endurance and re-usability. After multiple revisions of the design, we implemented an approach based on uncoated optical fibers to induce movement (**Figure A.1**). With this pin-connector design, rotational movement from the galvo-unit was

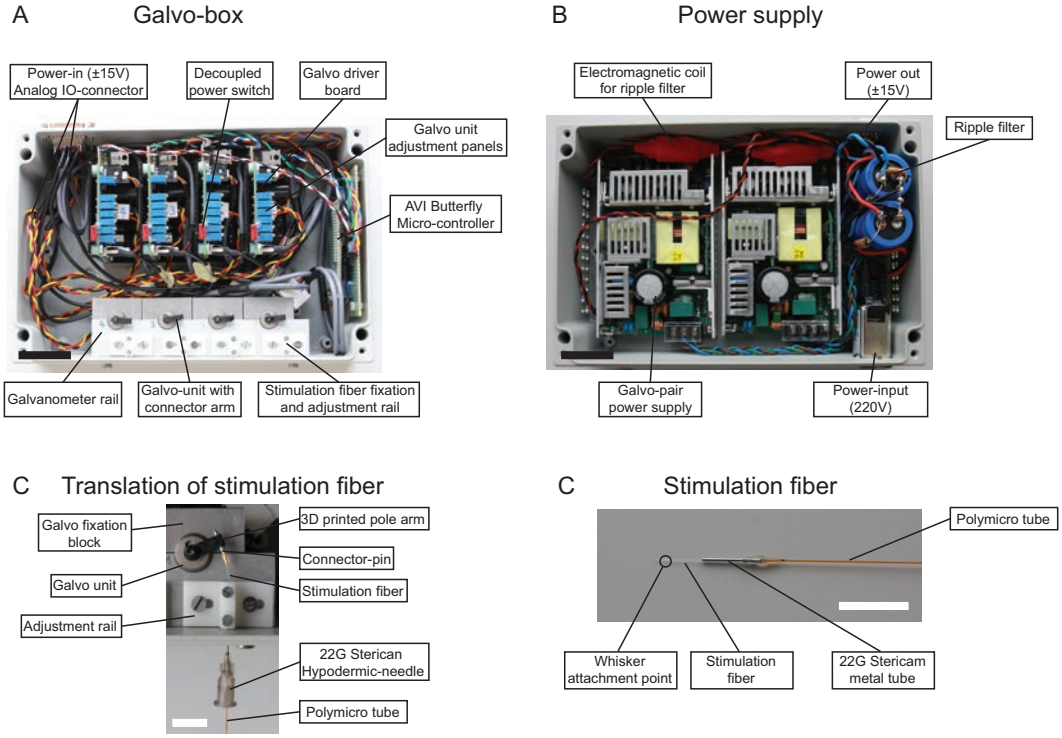

Figure A.1: Hardware implementation of galvanometer-driven whisker stimulation: **A:** Image of the stimulation box containing four galvano-units and their corresponding driver boards. Galvo-unit were secured in a metal rail. The stimulator box and the power supply box were constructed separately to reduce electrical noise transmission during electrophysiology experiments. A micro-controller board induced the start-up sequence, controlled voltage and monitored box temperatures. Scalebar 3cm.**B:** Image of the hardware implementation of the power supply box housing two power-units for the two galvo-unit pairs. A ripple filter was added to remove noise from the power-units. Scalebar 3cm **C:** Implementation of the attachment point of the stimulation fibers to the galvo-unit. 3D printed, custom-built pole-arms were attached to the galvo-unit. The pole-arms are equipped with a lightweight metal pin, which is then attached to a connector socket on the pole arm. The uncoated stimulation fiber itself is embedded in a capillary tube (Polymicro). To reduce friction during translation along the edges and to significantly increase durability of the fibers, a smoothed syringe tip was attached to the end points of the Polymicro tube. Scalebar 1.5cm**D:** Stimulation fiber front-end that is attached to a whisker. As described in C, a smoothed stainless steel syringe tip is glued onto the Polymicro tube to ensure low friction translation of the fiber. Scalebar 1cm

transformed into a translational movement through a stimulation fiber. The stimulation fiber was embedded in a low friction, high heat resistance capillary tube to guide it. Stainless steel caps (extracted from a 22G hypodermic-needle) were glued to the end points of the capillary tube to ensure smooth movement inside the tubing. The implemented fiber approach showed

very robust stimulation and longevity. Up to 30'000 pulses could be applied before the capillary tubing would break [*]. To ensure stable and reproducible stimulation, fibers were attached to a micro-manipulator and embedded in Plasticine.

Galvo-units had to be carefully calibrated with the stimulation fibers attached to ensure stable translation. As seen in **Figure A.1A**, each galvo-unit is controlled by a driver board. Each driver board can be adjusted separately to optimize important parameters such as the size of the servo gain, low and high-frequency damping, electrical offset of the driver (not the galvo) and input sensitivity. We further modified the board to add a security power-switch on top of each driver board (red knobs on boards in **Figure A.1A**).

To secure each galvo, a metal rail was fabricated to maintain flexibility when exchanging defective galvo-units or to reposition them easily. To secure the stimulation fibers, we built a fiber adjustment rail to easily move around the steel cap of the fiber (see **Figure A.1C** for a detailed image). To maintain maximum flexibility and to reduce transmission of electrical noise to the electrophysiology and two-photon imaging systems, we build a separate power-supply box, powering four galvos (**Figure A.1B**). The power supply was equipped with a ripple filter to reduce noise originating from the galvo-power supplies.

The construction, implementation and testing of the final design took roughly 200 man hours. The presented design implements a flexible, cost-efficient and powerful stimulation system while maintaining small spatial dimensions usable in any *in vivo* setup.

A.3 Software implementation

The control software was implemented in *LabView*, a commonly used visual programming language developed by NI. LabView is particularly useful for the implementation of mechanical and digital driver software as NI provides great support for digital and analog I/O interfaces. The implementation of the control software had to satisfy following criteria:

[*] Fibers would last up to 10-15 experiments, each experiment consisting of at least 2500 high velocity stimulation pulses

- Easily configurable settings for driving a specific galvo-unit, independent of instance number, including import and export functionality of configuration files

- Live feedback of the galvo position at any given time during the experiment

- Text logging of applied stimulus configuration used for data analysis

- Master / slave modes that are able to trigger an instance or receive a trigger from another instance

- Implementation of an *Experiment Controller* capable of randomly generating stimulus sequences including per trial triggering

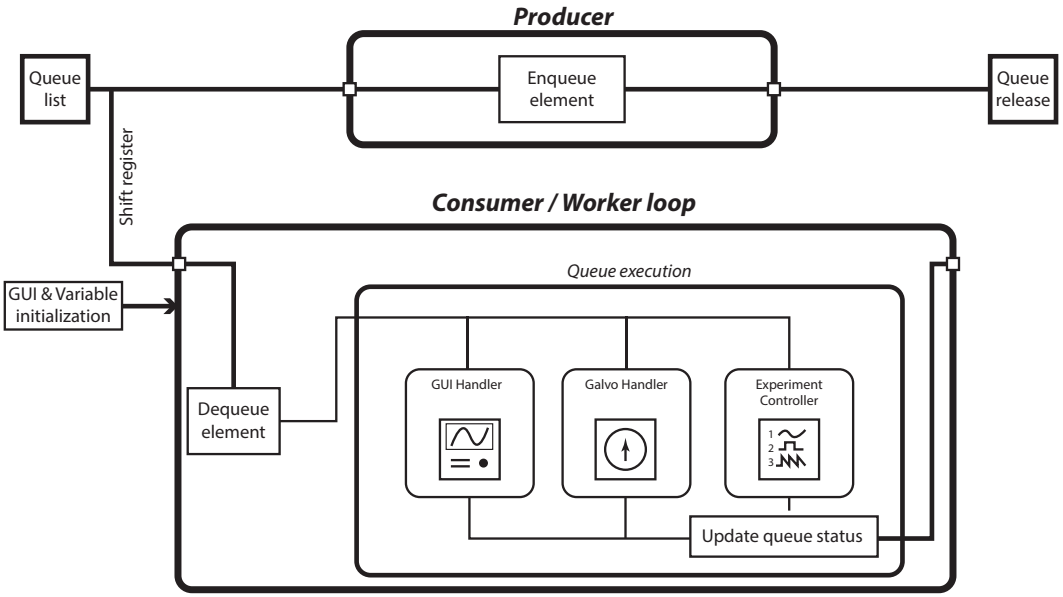

Figure A.2: Architecture of software implementation: Schematic overview of the used design pattern to implement a flexible and modular software environment. The GUI based implementation uses the Consumer-Producer design pattern as a backbone. Changes in the GUI are added to a queue list which is then processed by the worker loop. GUI elements and hardware parameters are handled separately. Squares indicate shift registers[a]. If elements in the enqueue loop change, the dequeue element sends requests to the three handler instances (GUI Handler, Galvo Handler and Experiment Controller). Upon state changes of the GUI, the GUI handler updates all instances accordingly. The galvo handler instantiates, controls and displays any state changes of galvo-units. An unlimited number of galvo instances can be created or deleted for each experiment. The experiment controller contains all necessary parameters for parsing to the Galvo Handler upon state changes.

[a] Shift registers are used in LabView to pass values between loop iterations

Based on above mentioned software requirements, the software was implemented based on the Consumer-Producer design pattern. This design pattern has the advantage that status changes in the configuration are handled globally through an enqueue/dequeue loop. GUI elements were therefore updated through state changes either induced by the user or the global state. The software contains three sub-controllers handling hardware and GUI elements:

GUI Handler: Responsible for updating all GUI elements after user inputs (see **Figure A.3**). Visualization of galvanometer feedback on main GUI. It also handles the experiment execution status and displays information from the *Experiment Controller*

Galvo Handler: Implemented through a *type definition* [†]. The Galvo Handler creates, instantiates and drives a chosen set of galvo-units. Each galvo-unit is instantiated separately. A specific configuration can be saved in *.ini* files (see **Figure A.4**).

Experiment Controller: The experiment controller is responsible for triggering and applying a chosen stimulus set on the galvo-units (see **Figure A.5**). The experimental configuration is set through *Galvo Handler* configuration files which are executed as stimulus sets. In addition the experiment controller updates the queue status and forwards it to the GUI.

Labview implementation of core functionality

Listed below are screenshots for the implementation of the core components, including the GUI Handler, Galvo Handler and parts of the Experiment controller VI's.

[†]Type definitions are used in LabView to instantiate a custom control or indicator. It is similar to definition of a class in other programming languages

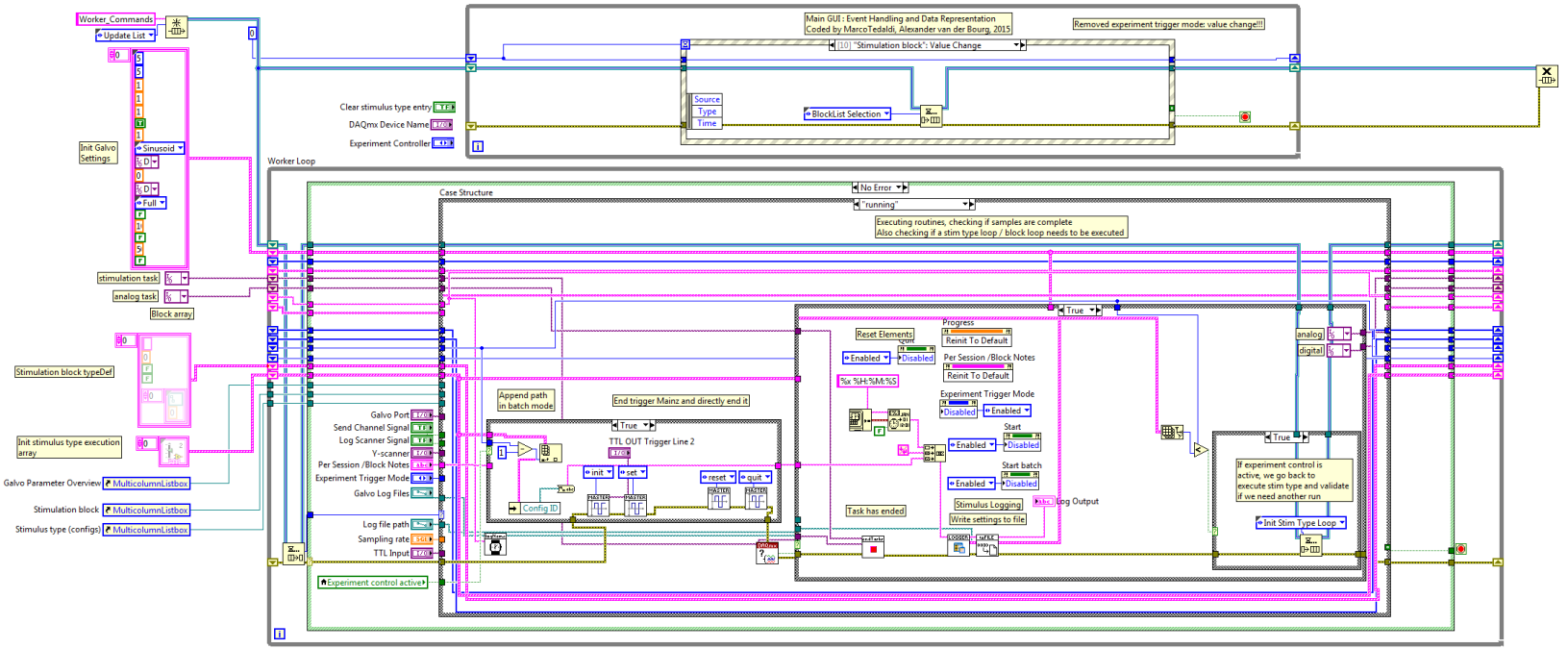

Figure A.3: Implementation of MainGUI.vi - This VI instantiates, creates and handles all necessary parameters and state changes of the software. The state change for the start of an experiment is shown as an example. The VI contains many nested sub-blocks that are not shown.

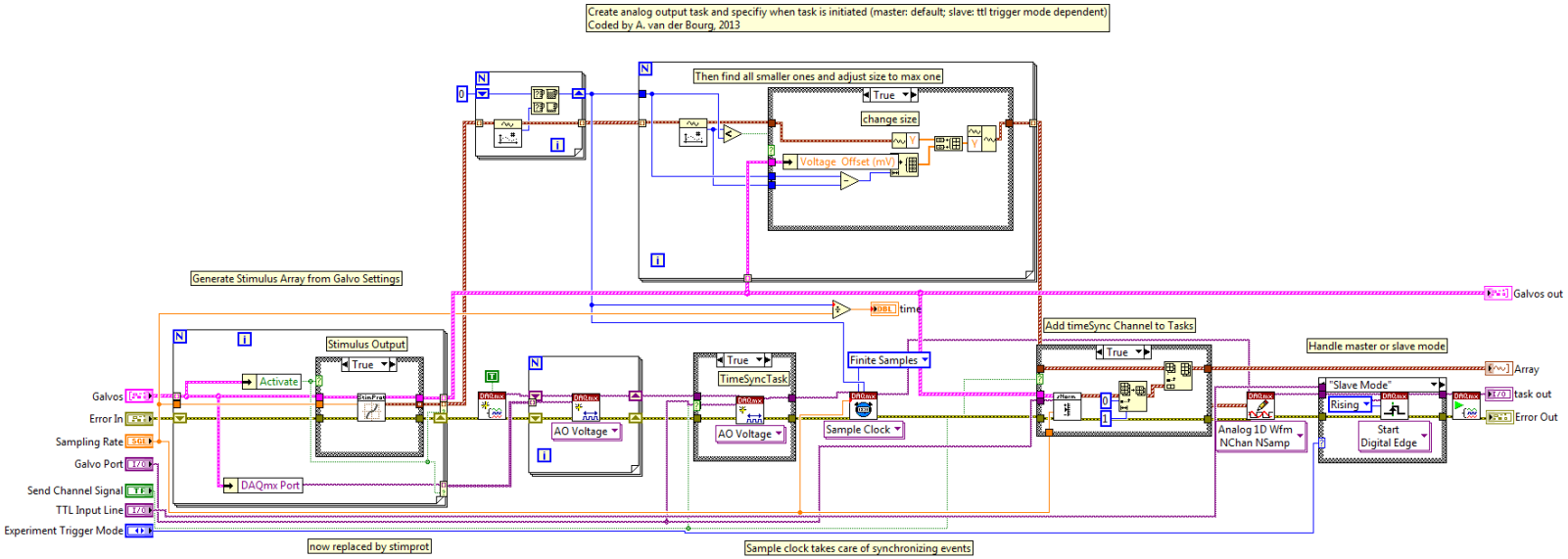

Figure A.4: Implementation of GalvoHandler.vi - This VI creates an analog output signal based on type-definition parameters. First, the analog output signal is created based on input parameters from the Galvo type definition (pink). Second, a DAQmx task is created and the channels for analog output and input signals are created and assigned to the global sample clock. Initiation and execution of the analog task is dependent on the currently active mode (master or slave).

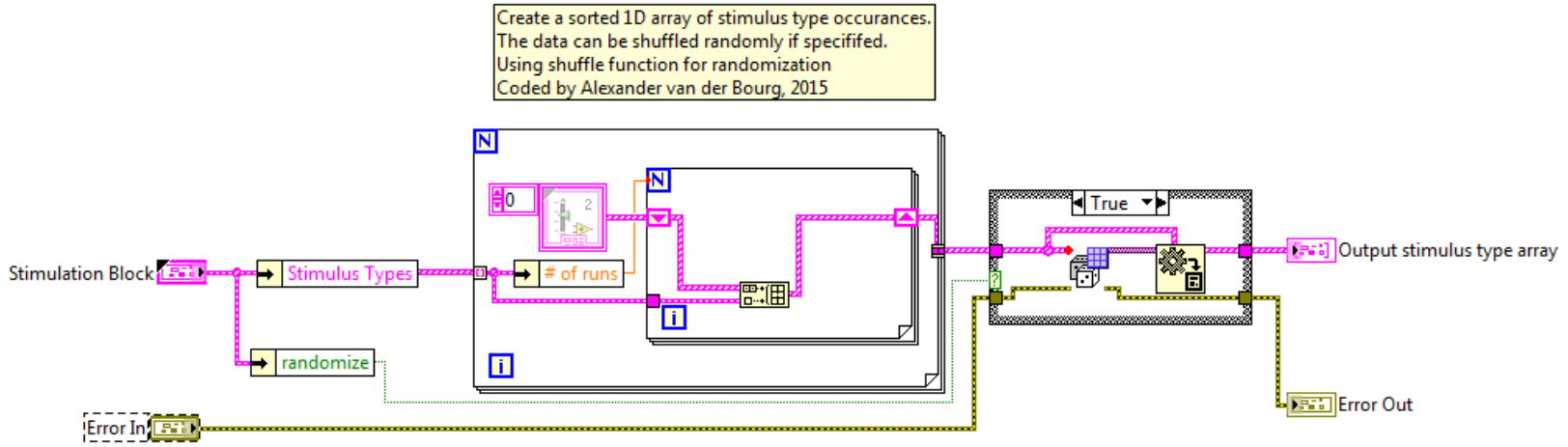

Figure A.5: Implementation of experimentController.vi - This VI creates a randomized stimulus set based on the list provided in the Experiment Controller GUI which is nested in the MainGUI.vi.

Implementation of the GUI

The user interface is separated in four sub-elements. The main user window contains the live feedback window displaying movement trajectories of all active galvo-units. It also contains a log book and displays the overall progress of the chosen experiment set (see **Figure A.6**). The second control unit is the *Stimulus Controller UI* (see **Figure A.7**). The Stimulus Con-

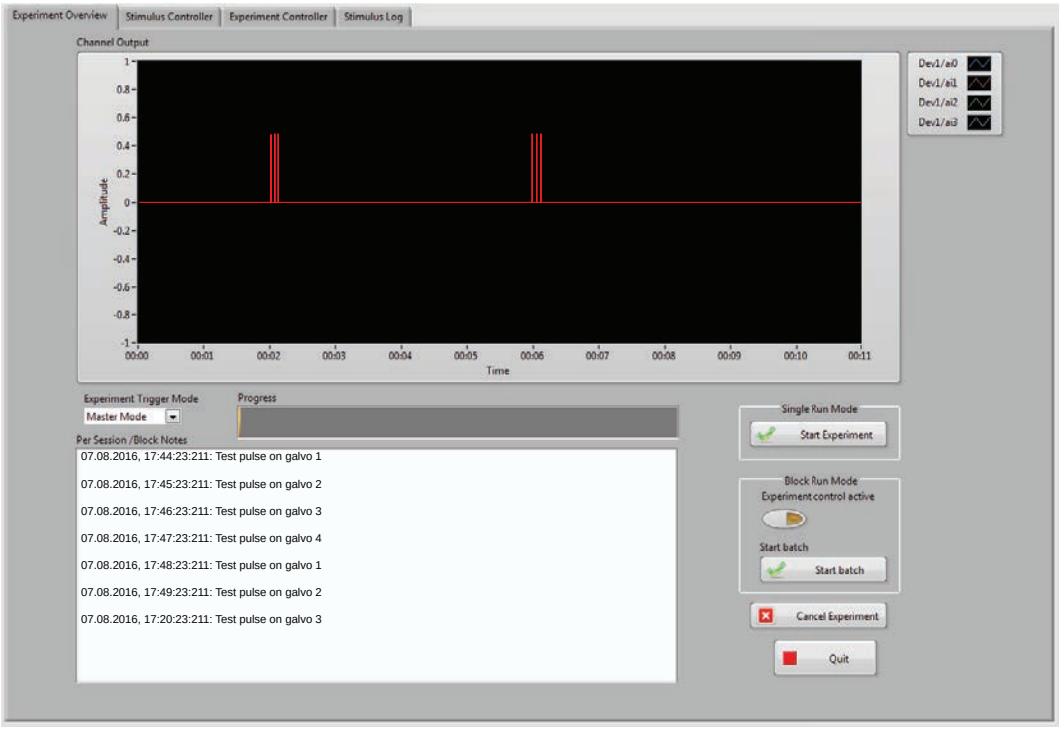

Figure A.6: Main User Interface: Screenshot of the Experiment overview panel. During stimulation, galvo-unit output is displayed in real-time (red trace). Personal notes for each experiment can be added by the user in the text field, including multi-line input. This panel also contains the option to set the stimulator into master or slave mode. In slave mode, the stimulator receives a trigger before executing a chosen set of stimuli. In the master mode, the stimulator is triggering another instance (Ephys-rig or two-photon software). Experiments can be executed in Single Run Mode or in Block Run Mode. Block mode only works if it is configured accordingly, as described in **Figure A.8**.

troller UI contains the modules for instantiation of galvo-units, including a list of all active and inactive galvos. Galvanometer settings can be configured for following stimulus functions: continues sinusoid, triangular, stepping and half-sinusoid waveforms. Each stimulus can be repeated multiple times. Hardware ports and feedback channels are also set in this menu. Chosen configurations from the galvo parameter overview will be displayed in the *Galvo Output*

Preview. Configurations can be saved and loaded through *.ini* files. The *Experiment Controller*

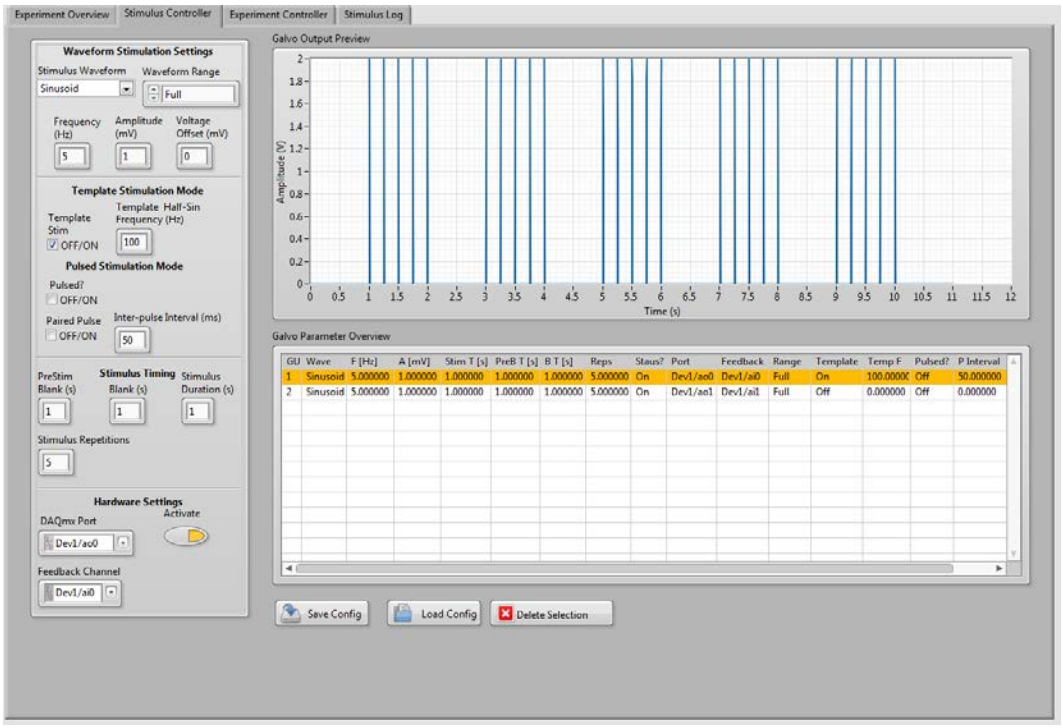

Figure A.7: Stimulus Controller User Interface: Screenshot of the stimulus controller implementation. Each galvo-unit is handled as its own instance. A stimulus preview allows to evaluate settings. Stimulus configurations can be saved and loaded from .ini files. The galvo-unit stimulus settings can be adjusted individually, including stimulus waveforms, number of stimuli per instance, inter-stimulus intervals, frequency, amplitude and voltage offsets. Each galvo-instance is displayed in the Galvo Parameter Overview table for inspection. The status of each galvo-unit settings can be modified individually and set to active or inactive.

handles and executes a set of stimuli based on user input. Single or multiple stimulus types can be loaded and executed in stimulation blocks. The number of trials per stimulus and blocks can be set separately. Stimuli can be applied randomly or in the order provided in the Experiment Controller (see **Figure A.8**). Block experiments can only be executed if they are saved in *.ini*-files set through *Stimulus Controller*. The *Stimulus Log and Hardware Controller* handles stimulus logging and global hardware parameters such as sampling rate and trigger ports (see **Figure A.9**). Trigger port and driver card assignments can be switched dynamically if needed. Additionally, trigger ports can be changed on NI breakout boxes individually.

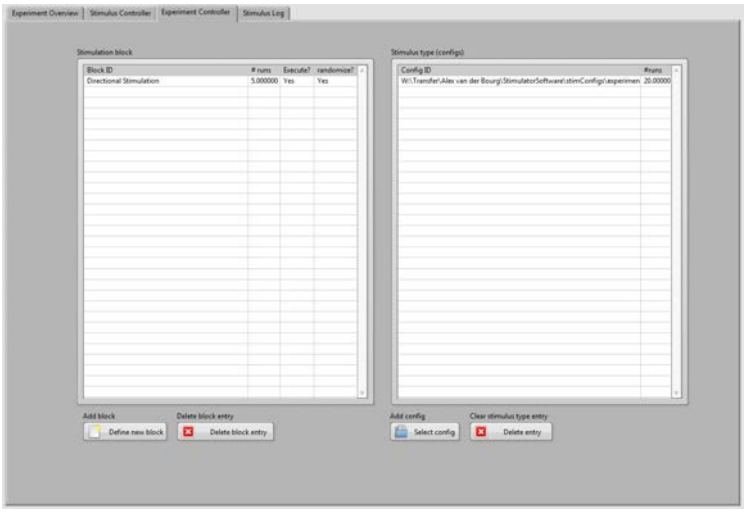

Figure A.8: Experiment Controller User Interface: Screenshot of the Experiment Controller implementation. The experiment controller allows to set up randomized stimulation of multiple stimulus types individually. A new block is created by clicking the Define new block button. Depending on the overall experimental configuration, the experiment controller receives or sends a trigger to execute a given trial or block.

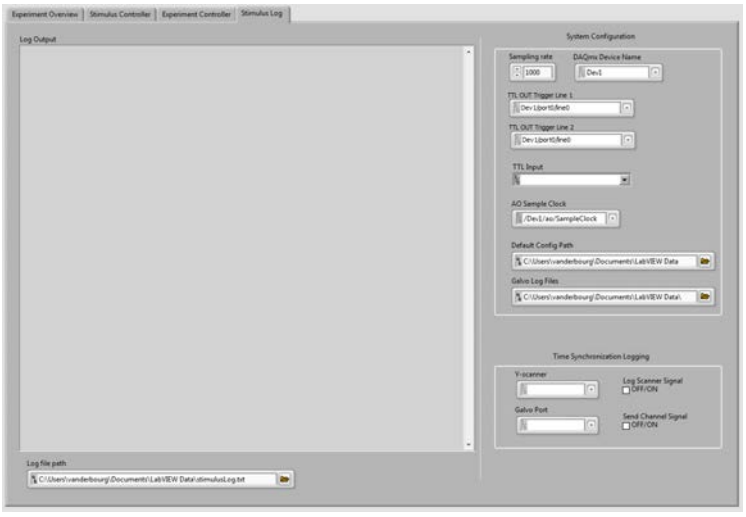

Figure A.9: Stimulus Log and Hardware Controller: Screenshot of the stimulus log and hardware controller implementation. Here, basic settings and a log file are displayed and can be modified. The log file is used to retrieve the presented stimulus list for data analysis. System configuration settings include the setting of the sampling rate that defines how many samples per second are generated for the analog output channels. Further settings include the trigger lines that are used for master and slave modes (according ot break-out box configuration). Default configuration paths for storing log files can also be set in this panel. For two-photon calcium imaging, a sync-logger is available to quantify trigger delay (if for example imaging is performed on a resonance scanner, etc).

B

ImageJ plugin package for calcium imaging data analysis

ImageJ is an open-source Java image processing platform, developed and funded by the National Institute of Health (Schindelin et al., 2015). Since its launch more than 25 years ago, many distributions with ImageJ as a core were developed and published (Schneider et al., 2012). One of the most famous of such distributions is FIJI (Schindelin et al., 2012), which is freely available at `http://fiji.sc/`. ImageJ and FIJI in particular provide a great toolbox for image analysis. However, they were lacking an easy to use solution for analysis of two-photon calcium imaging data. I therefore implemented a small FIJI Plugin package that provides basic functionality for image stabilization, extraction of calcium transients and annotation of regions of interest. Following documentation provides an overview of the software implementation of the *Two-photon Plugin toolbox* used for analysis of calcium imaging data. The source code for this

project is freely available at https://sourceforge.net/p/twophoton/code/ci/master/tree/2P_Tools/src/.

B.1 Implementation of a calcium imaging Plugin package

Imagej and FIJI provide the Plugin design pattern so that developers can extend the core functionality of the software easily. The *Two-photon Plugin toolbox* therefore implements the PlugIn class. All source files are implemented in Java and use most of the image processing functions already available with FIJI. The distribution and installation of the package is provided through a *.jar*-file. Installation of the Plugin package happens with a simple *drag-and-drop* onto FIJI's GUI panel.

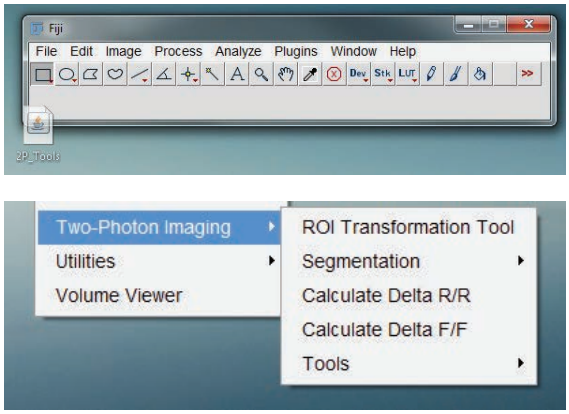

Figure B.1: Installation and Menu Entries of the Plugin package: **A:** Installation of the .jar distribution file: simply drag the file into the FIJI menu. **B:** Menu entries of the Plugin distribution. The plugin supports the extraction of calcium transients from ratiometric and non-ratiometric calcium indicators, stabilization of image stacks, extraction of ROIs and ROI annotation from a large stack to a time series.

B.2 Extraction of calcium transients from raw image stacks

During imaging experiments, it is beneficial and desirable to test if the overall quality of the gathered imaging data is satisfactory. My FIJI plugin provides an easy way to evaluate calcium transient dynamics in such situations. **Figure B.2** gives an overview of such an evaluation of

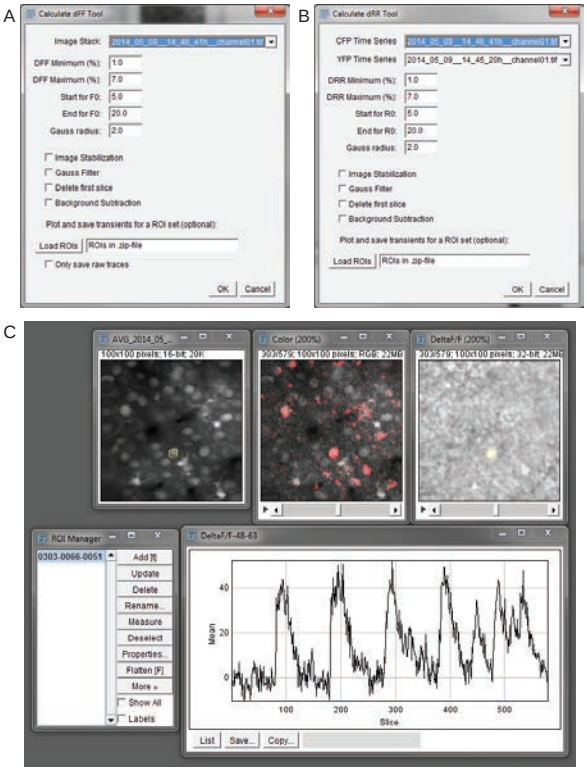

Figure B.2: Plugins to extract calcium transients for ratiometric and non-ratiometric indicators: **A:** User-interface to extract calcium transients from a single image stack, such as GCamP or OGB-1 AM. Start for F0 and End for F0 indicate the indexes of the stack from which F_0 will be calculated. The Gauss radius defines the radius in pixels for a simple Gaussian kernel smoothing filter. Tick-boxes let the user choose which operations will be performed, such as frame-by-frame image stabilization, application of a Gauss filter, deletion of the first slice of the stack and background subtraction. Note that deletion of the first slice is sometimes needed as a shutter artifact from the two-photon setup results in a black-pixel bar in the first frame. **B:** User-interface used to extract transients from ratiometric indicators. The CFP- and YFP-timeseries indicate the two stacks of the classical FRET-interaction (CFP-channel represents the donor and the YFP-channel the acceptor upon binding of a calcium ion). **C:** Representative example of a calcium trace (bottom) from a selected ROI. Top left: Average intensity projection from a single stack; top middle: color-coded activity profile; top-right: calculated $\frac{\Delta F}{F}$ stack.

calcium data in an example of an OGB-1 experiment (see Chapter 1 for details about bolus loading of OGB-1 AM). The plugin contains multiple options to process an image stack. *dFF Minimum* and *dFF Maximum* are used to define the range of color-labeling for an additional image stack that is used to visualize which neurons are active by chosen criteria (see **Figure B.2B** middle stack labeled *Color*). The plugin supports multiple functions which can be applied. One option is the application of a Gaussian smoothing filter which can help in reducing overall noise and intensity fluctuations in the calcium trace. Further options contain image stabilization and background subtraction. Background subtraction is implemented as the bottom 1^{st} percentile of the average intensity projection of the image stack.

Additionally, I also implemented a small tool that cleans up inconsistencies in the ROI-annotation in FIJI. It can happen that ROI-Sets are saved in an unreadable format for export in MATLAB. The small helper plugin as shown in **Figure B.3** cleans up such inconsistencies by creating simple ROI-object masks.

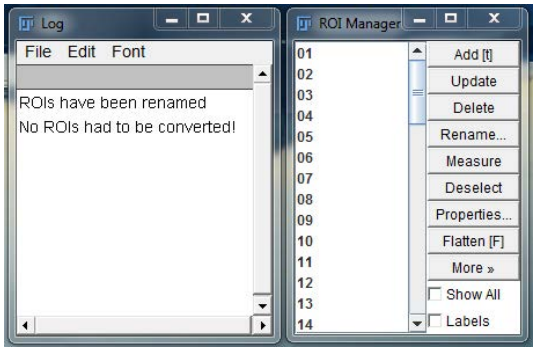

Figure B.3: ROI Parser helper tool: This small tool will evaluate a ROI-Set and remove any intersectional inconsitencies in the pixel annotation which can lead to errors when parsing the ROI-Set to Matlab. In addition the tool renames ROIs consitently and annotates a number based on the index position in the ROI Manager

B.3 Implementation of a segmentation algorithm to extract somatic cell body contours

The automatic segmentation and detection of somatic cell bodies from calcium imaging data is a challenging task for multiple reasons: (1) depending on the expression of a calcium sensor, axonal and dendridic arborizations of multiple neurons overlap and (2) the signal-to-noise ratio is not high enough to reliably segment contours of cells compared to a human annotator. Based on these limitations recent implementations did not rely on the image intensity distribution to find the contour of a cell but rather the pixel-by-pixel correlation of activity in an image series (Freeman et al., 2014). In the presented approach, I used an implementation based on gradient flow tracking (Li et al., 2007, 2008). My FIJI Plugin is creating a shell command instance where the C-routines from Li et al. (2007) are executed and parsed into a folder which is then fetched again by the Plugin to extract segmented regions of interest (ROIs). The used algorithm has the advantage that it can distinguish between touching cell nuclei as the gradient flow field relies on the center of mass for each cell body, creating unique seeds for each image segment (Li et al., 2008). Because the current implementation relies on the execution of *.bat* files and windows-command lines, it is only usable with Windows operating systems. Nevertheless, the provided plugin provides robust results for cells with continuous fluorescence (see **Figure B.4B**

for an example segmentation of OGB-1 AM bolus loaded cells). The segmentation of image stacks from genetically encoded calcium indicators such as YC-Nano 1.6 or GCamP is not possible due to its non uniform expression pattern in the soma, as the nucleus does not express the indicator. Segmentation of doughnut-shaped soma is not possible with the gradient flow approach as it relies on a semi-continuous image intensity distribution to locate cell contours at the edges (it would also fail as it would not find the center of mass of the soma as a seed point to iterate and generate the image intensity vector flow field). In conclusion, the segmentation algorithm works well for continuously filled somas but correlation-analysis approaches might work better to segment doughnut shaped structures.

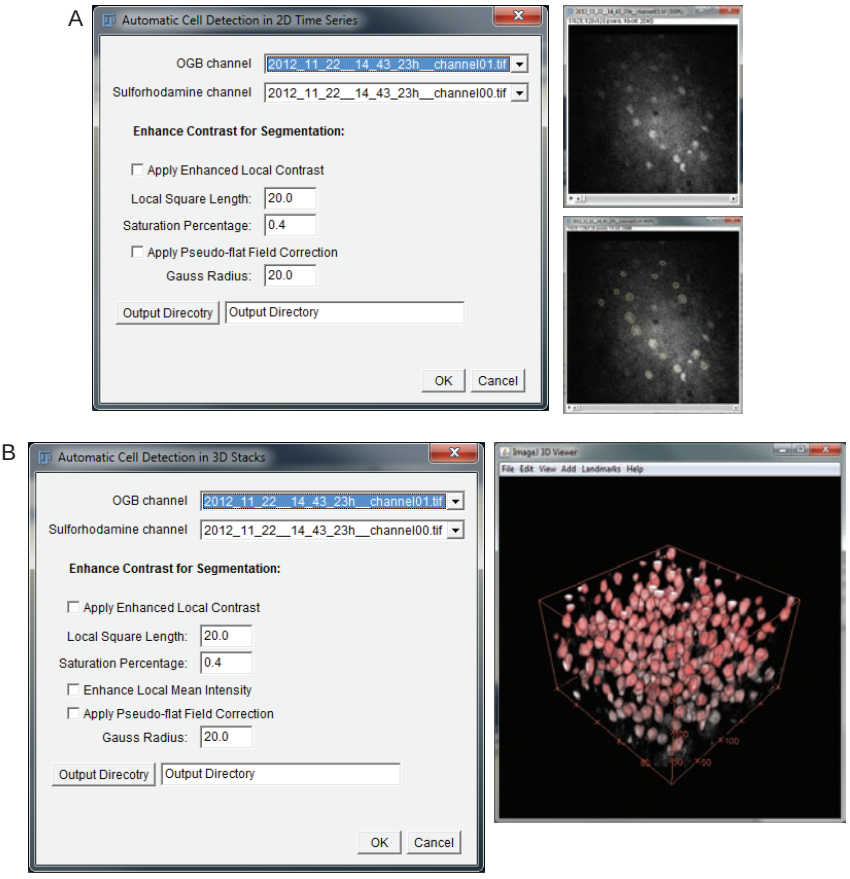

Figure B.4: Plugins to automatically extract 2D and 3D ROIs from calcium imaging data: **A:** The GUI of the 2D annotation tool (for single frame images and time series). Right: Example dataset of cells bolus loaded with OGB-1 AM at 120 μm depth. The low contrast ratio and labeling was used as an example that also in cases with low signal-to-noise of the labeled cells, the segmentation delivers reasonable results. **B:** Screenshot of the GUI for 3D segmentation. Right: Results of a 3D segmented image stack of neurons bolus loaded with OGB-1AM.

Plugin	Macro Command
2D Segmentation	run("2D Segmentation (time series)"," select=PATH_TO_OUTPUT_FOLDER enhance_local local_square_length=VALUE saturation_percentage=VALUE pseudo-flat_field gauss_radius=VALUE ogb=PATH_TO_OGB.tif sulforhodamine=PATH_TO_SR.tif");
3D Segmentation	run("3D Segmentation", " select=PATH_TO_OUTPUT_FOLDER textbackslash enhanced_local_contrast enhance_local_mean local_square_length=VALUE saturation_percentage=VALUE pseudo-flat gauss_radius=20 ogb=PATH_TO_OGB.tif sulforhodamine=PATH_TO_SR.tif");
Calculate dFF	run("Calculate Delta F/F", "dff_minimum=VALUE dff_maximum=VALUE start=VALUE end=VALUE gauss_radius=VALUE image_stabilization gauss_filter delete_first_slice image_stack=PATH_TO_STACK.tif");

Table B.1: Fiji toolbox Macro commands - Overview of the ImageJ Macro commands to call the segmentation and calculatedFF/dRR Plugins.

B.4 Batch-processing of calcium imaging data with ImageJ Macros

Depending on the situation, there arises the need to batch process a set of files with the same overall parameters. ImageJ provides the functionality to call any Plugin through its own Macro language (also given the developer made important parameters easily accesible and public). The segmentation Plugin as well as the Plugin to extract calcium transients have this functionality implemented. Table B.1 provides a list on how to call Plugin functions within ImageJ's Macro language (for example to create batch scripts) The execution of these Plugin routines is not only limited to FIJI or ImageJ. A custom distribution for the exchange of data between MATLAB and

FIJI (http://imagej.net/miji) allows to call any Plugin within a MATLAB instance. The creation of custom MATLAB scripts then potentially allows for processing of calcium imaging data. An early version of routines were implemented to automatically extract calcium transients from an imaging folder if new data was added. Because of issues with overall stability, this project was not made public. Nevertheless, accessing the presented Plugin routines with ImageJ Macro scripts already allows to speed up processing of large data folders (see example below).

An example macro-script to first segment cell contours and then extract calcium transients is given below:

Listing B.1: Example ImageJ Macro script to segment somata and extract calcium transients from a source folder containing multiple subfolders. Each subfolder contains an imaging data set.

```
/* Script using the FIJI Toolbox plugins to run through folders containing subfolders
which have to be segmented. Batch Mode is not supported or results in unwanted errors
for specific submodules (image stabilization), creation of ROISets in the Segmentation
Plugin.
*/

//Path to data to be processed
dataPath = "C:\\Users\\vanderbourg\\Desktop\\batchTestFolder\\";


//Execution order of Plugins
segment(dataPath);
calcDff(dataPath);



//Function to calculate dFF with FIJI Toolbox Plugin
function calcDff(pathToData){
  folderList = getFileList(pathToData);
  for (i=0; i<folderList.length; i++){
    //open images
    imgList = getFileList(pathToData + folderList[i]);
    //Assumption Sulforhodamine is channel_00 -> therefore entry 0
    ogbImg = pathToData + folderList[i] + imgList[1];
    outPutPath = pathToData + folderList[i] +"Segmentation\\";
    open(ogbImg);
    selectWindow(imgList[1]);
    run("Delete Slice");

    //now calculate dFF and save it to dFF_fileName
    subStrings = split(folderList[i], "/");
    outPutPath = dataPath + subStrings[0]+"\\" +"Segmentation\\";
    roiSet = outPutPath+subStrings[0]+"__channel01"+"_RoiSet.zip";
    //we have to save the RoiSet again, because of batch mode!
    //roiManager("Save", roiSet);
    roiManager("Open", roiSet);
    run("Calculate Delta F/F", "open="+roiSet+
    "dff_minimum=2 dff_maximum=8 start=5 end=100 gauss_radius=2 image_stabilization gauss_filter image_stack="
          +imgList[1]);
    //selectWindow("Montage");
    //saveAs("Tiff", pathToData +folderList[i] +"dFF_"+
    //   subStrings[0]+"__channel01"+"\\Montage.tif");

    //Close all windows for next iteration
    run("Close All");
```

```
45      selectWindow(subStrings[0]+"__channel01.log");
46      run("Close");
47      selectWindow("ROI Manager");
48      run("Close");
49      IJ.log("Processed files in "+folderList[i]);
50
51    }
52  }
53
54  function segment(pathToData){
55
56    /*Perform segmentation on folder items and save it
57    to the exeriment folder, then perform dFF analysis
58    */
59    folderList = getFileList(pathToData);
60
61    for (i=0; i<folderList.length; i++){
62      //open images
63      imgList = getFileList(pathToData + folderList[i]);
64      //Assumption Sulforhodamine is channel_00 -> therefore entry 0
65      srImg = pathToData + folderList[i] + imgList[0];
66      ogbImg = pathToData + folderList[i] + imgList[1];
67      outPutPath = pathToData + folderList[i] +"Segmentation\\";
68      open(ogbImg);
69      selectWindow(imgList[1]);
70      run("Delete Slice");
71      open(srImg);
72      selectWindow(imgList[0]);
73      run("Delete Slice");
74      File.makeDirectory(pathToData+folderList[i]+"Segmentation");
75      run("2D Segmentation (time series)","select="+outPutPath+
76        //"enhance_local local_square_length="+getWidth()/5+" saturation_percentage="+0.4+
77        " pseudo-flat_field gauss_radius="+getWidth()/5+
78        " ogb="+imgList[1]+" sulforhodamine="+imgList[0]);
79      //close all open windows to be ready for next iteration
80      roiManager("Reset");
81      run("Close All");
82      selectWindow("ROI Manager");
83      run("Close");
84    }
85  }
```

References

Ackman, J. B., Zeng, H., and Crair, M. C. (2014). Structured dynamics of neural activity across developing neocortex. *bioRxiv*, pages 1–24.

Adrian, B. Y. E. D. and Moruzzi, G. (1939). Impulses in the pyramidal tract. *J. Physiol*, 97(2):153–199.

Andermann, M. L. and Moore, C. I. (2006). A somatotopic map of vibrissa motion direction within a barrel column. *Nature neuroscience*, 9(4):543–551.

Arakawa, H. and Erzurumlu, R. S. (2015). Role of whiskers in sensorimotor development of C57BL/6 mice. *Behavioural Brain Research*, 287:146–155.

Avermann, M., Tomm, C., Mateo, C., Gerstner, W., and Petersen, C. C. H. (2012). Microcircuits of excitatory and inhibitory neurons in layer 2/3 of mouse barrel cortex. *Journal of {...}*.

Berényi, A., Somogyvári, Z., Nagy, A. J., Roux, L., Long, J. D., Fujisawa, S., Stark, E., Leonardo, A., Harris, T. D., and Buzsáki, G. (2014). Large-scale, high-density (up to 512 channels) recording of local circuits in behaving animals. *Journal of neurophysiology*, 111(5):1132–49.

Borgdorff, A. J., Poulet, J. F. a., and Petersen, C. C. H. (2007). Facilitating sensory responses in developing mouse somatosensory barrel cortex. *Journal of neurophysiology*, 97(4):2992–3003.

Brecht, M., Roth, A., and Sakmann, B. (2003). Dynamic Receptive Fields of Reconstructed Pyramidal Cells in Layers 3 and 2 of Rat Somatosensory Barrel Cortex. *The Journal of Physiology*, 553(1):243–265.

Brumberg, J. C. and Simons, J. (1996). Spatial Gradients and Inhibitory Summation in the Rat Whisker Barrel System. *Journal of Neurophysiology*, 76(1).

Buzsáki, G., Stark, E., Berényi, A., Khodagholy, D., Kipke, D. R., Yoon, E., and Wise, K. D. (2015). Tools for probing local circuits: High-density silicon probes combined with optogenetics. *Neuron*, 86(1):92–105.

Cabungcal, J.-H., Steullet, P., Morishita, H., Kraftsik, R., Cuenod, M., Hensch, T. K., and Do, K. Q. (2013). Perineuronal nets protect fast-spiking interneurons against oxidative stress. *Proceedings of the National Academy of Sciences of the United States of America*, 110(22):9130–5.

Cajal, S. R. y. and May, R. M. (1991). *Degeneration and Regeneration of the Nervous System*. Number 185. Oxford University Press, 1 edition.

Carvell, G. E. and Simons, D. J. (1988). Membrane potential changes in rat SmI cortical neurons evoked by controlled stimulation of mystacial vibrissae. *Brain Research*, 448(1):186–191.

Chandrasekaran, S., Navlakha, S., Audette, N. J., McCreary, D. D., Suhan, J., Bar-Joseph, Z., and Barth, a. L. (2015). Unbiased, High-Throughput Electron Microscopy Analysis of Experience-Dependent Synaptic Changes in the Neocortex. *Journal of Neuroscience*, 35(50):16450–16462.

Chen, J. L., Carta, S., Soldado-Magraner, J., Schneider, B. L., and Helmchen, F. (2013). Behaviour-dependent recruitment of long-range projection neurons in somatosensory cortex. *Nature*, 499(7458):336–40.

Chen, J. L., Voigt, F. F., Javadzadeh, M., Krueppel, R., and Helmchen, F. (2016). Long-Range population dynamics of anatomically defined neocortical networks. *eLife*, 5:1–26.

Chiaia, N. L., Zhang, S., King, T. D., and Rhoades, R. W. (1994). Evidence for prenatal competition among the central arbors of trigeminal primary afferent neurons: Single axon analysis. *Journal of Comparative Neurology*, 345(2):303–313.

Clack, N. G., Connor, D. H. O., Huber, D., Petreanu, L., Hires, A., Peron, S., Svoboda, K., and Myers, E. W. (2012). Automated Tracking of Whiskers in Videos of Head Fixed Rodents. *PLoS computational biology*, 8(7).

Clancy, K. B., Schnepel, P., Rao, a. T., and Feldman, D. E. (2015). Structure of a Single Whisker Representation in Layer 2 of Mouse Somatosensory Cortex. *Journal of Neuroscience*, 35(9):3946–3958.

Clem, R. L. and Barth, A. (2006). Pathway-Specific Trafficking of Native AMPARs by In Vivo Experience. *Neuron*, 49(5):663–670.

Clem, R. L., Celikel, T., and Barth, A. L. (2008). Ongoing in vivo experience triggers synaptic metaplasticity in the neocortex. *Science (New York, N.Y.)*, 319(5859):101–104.

Clemens, J. M., Ritter, N. J., Roy, A., Miller, J. M., and Van Hooser, S. D. (2012). The Laminar Development of Direction Selectivity in Ferret Visual Cortex. *Journal of Neuroscience*, 32(50):18177–18185.

Cruz-Martin, A. and Portera-Cailliau, C. (2014). In vivo imaging of axonal and dendritic structures in neonatal mouse cortex. *Cold Spring Harbor protocols*, 2014(1):pdb.prot080150.

Cuevas, J. (2014). Electrophysiological Recording Techniques. *Reference Module in Biomedical Research*, 54:27–41.

De Kock, C. P. J., Bruno, R. M., Spors, H., and Sakmann, B. (2007). Layer- and cell-type-specific suprathreshold stimulus representation in rat primary somatosensory cortex. *The Journal of Physiology*, 581(1):139–154.

Denk, W., Strickler, J. H., and Webb, W. W. (1990). Two-photon laser scanning fluorescence microscopy. *Science (New York, N.Y.)*, 248(4951):73–6.

Diamond, M. E., von Heimendahl, M., Knutsen, P. M., Kleinfeld, D., and Ahissar, E. (2008). 'Where' and 'what' in the whisker sensorimotor system. *Nature reviews. Neuroscience*, 9(8):601–612.

Doischer, D., Aurel Hosp, J., Yanagawa, Y., Obata, K., Jonas, P., Vida, I., and Bartos, M. (2008). Postnatal Differentiation of Basket Cells from Slow to Fast Signaling Devices. *Journal of Neuroscience*, 28(48):12956–12968.

Durham, D. and Woolsey, T. A. (1984). Effects of neonatal whisker lesions on mouse central trigeminal pathways. *The Journal of comparative neurology*, 223(3):424–47.

Ebara, S., Kumamoto, K., Matsuura, T., Mazurkiewicz, J. E., and Rice, F. L. (2002). Similarities and differences in the innervation of mystacial vibrissal follicle-sinus complexes in the rat and cat: A confocal microscopic study. *Journal of Comparative Neurology*, 449(2):103–119.

Ego-Stengel, V. and Souza, T. (2005). Spatiotemporal characteristics of neuronal sensory integration in the barrel cortex of the rat. *Journal of Neurophysiology*, 93:1450–1467.

Einevoll, G. T., Franke, F., Hagen, E., Pouzat, C., and Harris, K. D. (2012). Towards reliable spike-train recordings from thousands of neurons with multielectrodes. *Current opinion in neurobiology*, 22(1):11–7.

Einevoll, G. T., Kayser, C., Logothetis, N. K., and Panzeri, S. (2013). Modelling and analysis of local field potentials for studying the function of cortical circuits. *Nature reviews. Neuroscience*, 14(11):770–85.

Erchova, I. A., Petersen, R. S., and Diamond, M. E. (2003). Effect of developmental sensory and motor deprivation on the functional organization of adult rat somatosensory cortex. *Brain Research Bulletin*, 60(4):373–386.

Erwin Neher and Sakmann, B. (1992). The patch clamp techique. *Scientific American*.

Erzurumlu, R. S. and Gaspar, P. (2012). Development and critical period plasticity of the barrel cortex. *The European journal of neuroscience*, 35(10):1540–53.

Espinosa, J. S., Wheeler, D. G., Tsien, R. W., and Luo, L. (2009). Uncoupling Dendrite Growth and Patterning: Single-Cell Knockout Analysis of NMDA Receptor 2B. *Neuron*, 62(2):205–217.

Feldmeyer, D., Brecht, M., Helmchen, F., Petersen, C. C. H., Poulet, J. F. a., Staiger, J. F., Luhmann, H. J., and Schwarz, C. (2013). Barrel cortex function. *Progress in neurobiology*, 103:3–27.

Fox, K. (2002). Anatomical pathways and molecular mechanisms for plasticity in the barrel cortex. *Neuroscience*, 111(4):799–814.

Fox, K. (2008). *Barrel Cortex*, volume 1. Cambridge.

Freeman, J., Vladimirov, N., Kawashima, T., Mu, Y., Sofroniew, N. J., Bennett, D. V., Rosen, J., Yang, C.-T., Looger, L. L., and Ahrens, M. B. (2014). Mapping brain activity at scale with cluster computing. *Nature methods*, 11(9):941–950.

Ghazanfar, a. a., Stambaugh, C. R., and Nicolelis, M. a. (2000). Encoding of tactile stimulus location by somatosensory thalamocortical ensembles. *The Journal of neuroscience : the official journal of the Society for Neuroscience*, 20(10):3761–3775.

Glazewski, S. and Barth, A. L. (2015). Stimulus intensity determines experience-dependent modifications in neocortical neuron firing rates. *European Journal of Neuroscience*, 41(November 2014):410–419.

Göbel, W. and Helmchen, F. (2007). In vivo calcium imaging of neural network function. *Physiology (Bethesda, Md.)*, 22(51):358–365.

Göbel, W., Kampa, B. M., and Helmchen, F. (2007). Imaging cellular network dynamics in three dimensions using fast 3D laser scanning. *Nature methods*, 4(1):73–79.

Goldreich, D., Peterson, B. E., and Merzenich, M. M. (1998). Optical imaging and electrophysiology of rat barrel cortex. II. Responses to paired-vibrissa deflections. *Cerebral Cortex*, 8(2):184–192.

Golshani, P., Gonçalves, J. T., Khoshkhoo, S., Mostany, R., Smirnakis, S., and Portera-Cailliau, C. (2009). Internally mediated developmental desynchronization of neocortical network activity. *Journal of Neuroscience*, 29(35):10890–10899.

Gopal, V. and Hartmann, M. J. Z. (2007). Using hardware models to quantify sensory data acquisition across the rat vibrissal array. *Bioinspiration & biomimetics*, 2(4):S135–S145.

Göppert-Mayer, M. (1931). Uber Elementarakte mit zwei Quantensprüngen. *Annalen der Physik*, 401(3):273–294.

Grant, R. a., Mitchinson, B., and Prescott, T. J. (2012). The development of whisker control in rats in relation to locomotion. *Developmental Psychobiology*, 54(2):151–168.

Gray, C. M., Maldonado, P. E., Wilson, M., and McNaughton, B. (1995). Tetrodes markedly improve the reliability and yield of multiple single-unit isolation from multi-unit recordings in cat striate cortex. *Journal of Neuroscience Methods*, 63(1-2):43–54.

Grewe, B. F., Langer, D., Kasper, H., Kampa, B. M., and Helmchen, F. (2010). High-speed in vivo calcium imaging reveals neuronal network activity with near-millisecond precision. *Nature methods*, 7(5):399–405.

Grewe, B. F., Voigt, F. F., van 't Hoff, M., and Helmchen, F. (2011). Fast two-layer two-photon imaging of neuronal cell populations using an electrically tunable lens. *Biomedical optics express*, 2(7):2035–2046.

Grienberger, C. and Konnerth, A. (2012). Imaging calcium in neurons. *Neuron*, 73(5):862–885.

Guo, H., Hong, S., Jin, X. L., Chen, R. S., Avasthi, P. P., Tu, Y. T., Ivanco, T. L., and Li, Y. (2000). Specificity and efficiency of Cre-mediated recombination in Emx1-Cre knock-in mice. *Biochemical and biophysical research communications*, 273(2):661–5.

Guo, Z., Li, N., Huber, D., Ophir, E., Gutnisky, D., Ting, J., Feng, G., and Svoboda, K. (2014). Flow of Cortical Activity Underlying a Tactile Decision in Mice. *Neuron*, 81(1):179–194.

Hagihara, K. M., Murakami, T., Yoshida, T., Tagawa, Y., and Ohki, K. (2015). Neuronal activity is not required for the initial formation and maturation of visual selectivity. *Nature Neuroscience*, 18(12):1780–8.

Harris, K. D., Henze, D. A., Csicsvari, J., Hirase, H., and Buzsaki, G. (2000). Accuracy of Tetrode Spike Separation as Determined by Simultaneous Intracellular and Extracellular Measurements. *J Neurophysiol*, 84(1):401–414.

Hazan, L., Zugaro, M., and Buzsáki, G. (2006). Klusters, NeuroScope, NDManager: A free software suite for neurophysiological data processing and visualization. *Journal of Neuroscience Methods*, 155(2):207–216.

Helmchen, F. and Denk, W. (2005). Deep tissue two-photon microscopy. *Nature Methods*, 2(12):932–940.

Hemelt, M. E., Kwegyir-Afful, E. E., Bruno, R. M., Simons, D. J., and Keller, A. (2010). Consistency of Angular Tuning in the Rat Vibrissa System. *Journal of Neurophysiology*, 104(6):3105–3112.

Hensch, T. K. (2005). Critical period plasticity in local cortical circuits. *Nature reviews. Neuroscience*, 6(11):877–88.

Hoy, J. L. and Niell, C. M. (2015). Layer-Specific Refinement of Visual Cortex Function after Eye Opening in the Awake Mouse. *Journal of Neuroscience*, 35(8):3370–3383.

Hubel, D. H. and Wiesel, T. N. (1962). Receptive fields, binocular interaction and functional architecture in the cat's visual cortex. *The Journal of Physiology*.

Hubel, D. H. and Wiesel, T. N. (1963). Receptive Fields of Cells in Striate Cortex of Very Young, Visually Inexperienced Kittens. *Journal of Neurophysiology*, 26:994–1002.

Ikezoe, K., Tamura, H., Kimura, F., and Fujita, I. (2012). Decorrelation of sensory-evoked neuronal responses in rat barrel cortex during postnatal development. *Neuroscience Research*, 73(4):312–320.

Itami, C. and Kimura, F. (2012). Developmental switch in spike timing-dependent plasticity at layers 4-2/3 in the rodent barrel cortex. *The Journal of neuroscience : the official journal of the Society for Neuroscience*, 32(43):15000–11.

Jacob, V., Estebanez, L., Le Cam, J., Tiercelin, J.-Y., Parra, P., Parésys, G., and Shulz, D. E. (2010). The Matrix: A new tool for probing the whisker-to-barrel system with natural stimuli. *Journal of Neuroscience Methods*, 189(1):65–74.

Kaiser, W. and Garrett, C. (1961). Two-Photon Excitation in CaF2:Eu2+. *Physical Review Letters*, 7(6):229–231.

Katz, Y., Heiss, J. E., and Lampl, I. (2006). Cross-whisker adaptation of neurons in the rat barrel cortex. *The Journal of neuroscience : the official journal of the Society for Neuroscience*, 26(51):13363–72.

Khazipov, R. and Luhmann, H. J. (2006). Early patterns of electrical activity in the developing cerebral cortex of humans and rodents. *Trends in neurosciences*, 29(7):414–418.

Kleinfeld, D. and Delaney, K. R. (1996). Distributed representation of vibrissa movement in the upper layers of somatosensory cortex revealed with voltage-sensitive dyes. *Journal of Comparative Neurology*, 375(1):89–108.

Kremer, Y., Léger, J.-F., Goodman, D., Brette, R., and Bourdieu, L. (2011). Late emergence of the vibrissa direction selectivity map in the rat barrel cortex. *Journal of Neuroscience*, 31(29):10689–10700.

Krupa, D. J., Matell, M. S., Brisben, a. J., Oliveira, L. M., and Nicolelis, M. a. (2001). Behavioral properties of the trigeminal somatosensory system in rats performing whisker-dependent tactile discriminations. *The Journal of neuroscience : the official journal of the Society for Neuroscience*, 21(15):5752–5763.

Kuhlman, S. J., Olivas, N. D., Tring, E., Ikrar, T., Xu, X., and Trachtenberg, J. T. (2013). A disinhibitory microcircuit initiates critical-period plasticity in the visual cortex. *Nature*, 501(7468):543–6.

Landers, M. and Philip Zeigler, H. (2006). Development of rodent whisking: trigeminal input and central pattern generation.

Langer, D., van 't Hoff, M., Keller, A. J., Nagaraja, C., Pfäffli, O. A., Göldi, M., Kasper, H., and Helmchen, F. (2013). HelioScan: a software framework for controlling in vivo microscopy setups with high hardware flexibility, functional diversity and extendibility. *Journal of neuroscience methods*, 215(1):38–52.

Lavdas, a. a., Grigoriou, M., Pachnis, V., and Parnavelas, J. G. (1999). The medial ganglionic eminence gives rise to a population of early neurons in the developing cerebral cortex. *The Journal of neuroscience : the official journal of the Society for Neuroscience*, 19(19):7881–7888.

Lee, S., Kruglikov, I., Huang, Z. J., Fishell, G., and Rudy, B. (2013). A disinhibitory circuit mediates motor integration in the somatosensory cortex. *Nature neuroscience*, 16(11):1662–70.

Lehky, S. R., Kiani, R., Esteky, H., and Tanaka, K. (2014). Dimensionality of object representations in monkey inferotemporal cortex. *Neural computation*, 1872(10):1840–1872.

Lendvai, B., Stern, E. A., Chen, B., and Svoboda, K. (2000). Experience-dependent plasticity of dendritic spines in the developing rat barrel cortex in vivo. *Nature*, 404(6780):876–881.

Li, G., Liu, T., Nie, J., Guo, L., Chen, J., Zhu, J., Xia, W., Mara, A., Holley, S., and Wong, S. T. C. (2008). Segmentation of touching cell nuclei using gradient flow tracking. *Journal of Microscopy*, 231(1):47–58.

Li, G., Liu, T., Tarokh, A., Nie, J., Guo, L., Mara, A., Holley, S., and Wong, S. T. C. (2007). 3D cell nuclei segmentation based on gradient flow tracking. *BMC cell biology*, 8:40.

Ma, P. M. (1993). Barrelettes - Architectonic vibrissal representations in the brainstem trigeminal complex of the mouse. II. Normal post-natal development. *Journal of Comparative Neurology*, 327(3):376–397.

Madisen, L., Garner, A. R., Carandini, M., Zeng, H., Madisen, L., Garner, A. R., Shimaoka, D., Chuong, A. S., Klapoetke, N. C., Li, L., van der Bourg, A., Niino, Y., Egolf, L., Monetti,

C., Gu, H., Mills, M., and Cheng, A. (2015). Transgenic Mice for Intersectional Targeting of Neural Sensors and Effectors with High Specificity and Performance NeuroResource Transgenic Mice for Intersectional Targeting of Neural Sensors and Effectors with High Specificity and Performance. *Neuron*, pages 942–958.

Manns, I. D., Sakmann, B., and Brecht, M. (2004). Sub- and suprathreshold receptive field properties of pyramidal neurones in layers 5A and 5B of rat somatosensory barrel cortex. *The Journal of Physiology*, 556(2):601–622.

Maravall, M., Stern, E. A., and Svoboda, K. (2004). Development of intrinsic properties and excitability of layer 2/3 pyramidal neurons during a critical period for sensory maps in rat barrel cortex. *Journal of Neurophysiology*, 92(1):144–156.

McNaughton, B. L., O'Keefe, J., and Barnes, C. A. (1983). The stereotrode: A new technique for simultaneous isolation of several single units in the central nervous system from multiple unit records. *Journal of Neuroscience Methods*, 8(4):391–397.

Minderer, M., Liu, W., Sumanovski, L. T., Kügler, S., Helmchen, F., and Margolis, D. J. (2011). Chronic imaging of cortical sensory map dynamics using a genetically encoded calcium indicator. *The Journal of Physiology*, pages no—-no.

Mirabella, G., Battiston, S., and Diamond, M. E. (2001). Integration of multiple-whisker inputs in rat somatosensory cortex. *Cerebral cortex (New York, N.Y. : 1991)*, 11(2):164–170.

Mitrukhina, O., Suchkov, D., Khazipov, R., and Minlebaev, M. (2015). Imprecise Whisker Map in the Neonatal Rat Barrel Cortex. *Cerebral Cortex*, 25(10):3458–3467.

Mitzdorf, U. (1985). Current source-density method and application in cat cerebral cortex: investigation of evoked potentials and EEG phenomena. *Physiol Rev*, 65(1):37–100.

Moore, C. I., Nelson, S. B., and Sur, M. (1999). Dynamics of neuronal processing in rat somatosensory cortex. *Trends in Neurosciences*, 22(11):513–520.

Mountcastle, V. (1957). Modality and topographic properties of single neurons of cat's somatic sensory cortex. *Journal of neurophysiology*, 20(4):408–34.

Musall, S., von der Behrens, W., Mayrhofer, J. M., Weber, B., Helmchen, F., and Haiss, F. (2014). Tactile frequency discrimination is enhanced by circumventing neocortical adaptation. *Nature neuroscience*, 17(11):1567–73.

Nadarajah, B. and Parnavelas, J. G. (2002). Modes of Neuronal Migration in the Developing Cerebral Cortex. *Nature Reviews Neuroscience*, 3(June):423–432.

Nguyen, Q. T., Callamaras, N., Hsieh, C., and Parker, I. (2001). Construction of a two-photon microscope for video-rate Ca(2+) imaging. *Cell calcium*, 30(6):383–93.

Nicholson, C. and Freeman, J. a. (1975). Theory of current source-density analysis and determination of conductivity tensor for anuran cerebellum. *Journal of neurophysiology*, 38(2):356–368.

Nimmerjahn, A., Kirchhoff, F., Kerr, J. N. D., and Helmchen, F. (2004). Sulforhodamine 101 as a specific marker of astroglia in the neocortex in vivo. *Nature methods*, 1(1):31–7.

Noctor, S. C., Martínez-Cerdeño, V., Ivic, L., and Kriegstein, A. R. (2004). Cortical neurons arise in symmetric and asymmetric division zones and migrate through specific phases. *Nature neuroscience*, 7(2):136–144.

Pammer, L., O'Connor, D. H., Hires, S. A., Clack, N. G., Huber, D., Myers, E. W., and Svoboda, K. (2013). The mechanical variables underlying object localization along the axis of the whisker. *The Journal of neuroscience : the official journal of the Society for Neuroscience*, 33(16):6726–41.

Petersen, C. C. H. (2007). The Functional Organization of the Barrel Cortex. *Neuron*, 56(2):339–355.

Piñon, M. C., Jethwa, A., Jacobs, E., Campagnoni, A., and Molnár, Z. (2009). Dynamic integration of subplate neurons into the cortical barrel field circuitry during postnatal development in the Golli-tau-eGFP (GTE) mouse. *The Journal of physiology*, 587(Pt 9):1903–15.

Quairiaux, C., Megevand, P., Kiss, J. Z., and Michel, C. M. (2011). Functional Development of Large-Scale Sensorimotor Cortical Networks in the Brain. *Journal of Neuroscience*, 31(26):9574–9584.

Quist, B. W., Seghete, V., Huet, L. A., Murphey, T. D., and Hartmann, M. J. Z. (2014). Modeling forces and moments at the base of a rat vibrissa during noncontact whisking and whisking against an object. *The Journal of neuroscience : the official journal of the Society for Neuroscience*, 34(30):9828–44.

Ramirez, A., Pnevmatikakis, E. A., Merel, J., Paninski, L., Miller, K. D., and Bruno, R. M. (2014). Spatiotemporal receptive fields of barrel cortex revealed by reverse correlation of synaptic input. *Nature neuroscience*, advance on.

Reyes-Puerta, V., Kim, S., Sun, J.-J., Imbrosci, B., Kilb, W., and Luhmann, H. J. (2015a). High Stimulus-Related Information in Barrel Cortex Inhibitory Interneurons. *PLOS Computational Biology*, 11(6):e1004121.

Reyes-Puerta, V., Sun, J.-J., Kim, S., Kilb, W., and Luhmann, H. J. (2015b). Laminar and Columnar Structure of Sensory-Evoked Multineuronal Spike Sequences in Adult Rat Barrel Cortex In Vivo. *Cerebral Cortex*, 25(8):2001–2021.

Rochefort, N., Garaschuk, O., Milos, R., Narushima, M., Marandi, N., Pichler, B., Kovalchuk, Y., and Konnerth, a. (2009). Sparsification of neuronal activity in the visual cortex at eye-opening. *Proceedings of the National Academy of Sciences*, 106(35):1–6.

Rochefort, N. L., Narushima, M., Grienberger, C., Marandi, N., Hill, D. N., and Konnerth, A. (2011). Development of direction selectivity in mouse cortical neurons. *Neuron*, 71(3):425–32.

Rossant, C., Kadir, S. N., Goodman, D. F. M., Schulman, J., Belluscio, M., Buzsaki, G., and Harris, K. D. (2015). Spike sorting for large, dense electrode arrays. *bioRxiv*, 19(4):015198.

Sachidhanandam, S., Sermet, B. S., and Petersen, C. C. H. (2016). Parvalbumin-Expressing GABAergic Neurons in Mouse Barrel Cortex Contribute to Gating a Goal-Directed Sensorimotor Transformation. *Cell Reports*, 15(4):700–706.

Sachidhanandam, S., Sreenivasan, V., Kyriakatos, A., Kremer, Y., and Petersen, C. C. H. (2013). Membrane potential correlates of sensory perception in mouse barrel cortex. *Nature neuroscience*, 16(11):1671–7.

Sahara, S., Yanagawa, Y., O'Leary, D. D. M., and Stevens, C. F. (2012). The Fraction of Cortical GABAergic Neurons Is Constant from Near the Start of Cortical Neurogenesis to Adulthood. *Journal of Neuroscience*, 32(14):4755–4761.

Sakata, S. and Harris, K. D. (2009). Laminar Structure of Spontaneous and Sensory-Evoked Population Activity in Auditory Cortex. *Neuron*, 64(3):404–418.

Schindelin, J., Arganda-Carreras, I., Frise, E., Kaynig, V., Longair, M., Pietzsch, T., Preibisch, S., Rueden, C., Saalfeld, S., Schmid, B., Tinevez, J.-Y., White, D. J., Hartenstein, V., Eliceiri, K., Tomancak, P., and Cardona, A. (2012). Fiji: an open-source platform for biological-image analysis. *Nature Methods*, 9(7):676–682.

Schindelin, J., Rueden, C. T., Hiner, M. C., and Eliceiri, K. W. (2015). The ImageJ ecosystem: An open platform for biomedical image analysis. *Molecular Reproduction and Development*, in press:DOI: 10.1002/mrd.22489.

Schneider, C. a., Rasband, W. S., and Eliceiri, K. W. (2012). NIH Image to ImageJ: 25 years of image analysis. *Nature Methods*, 9(7):671–675.

Shimegi, S., Ichikawa, T., Akasaki, T., and Sato, H. (1999). Temporal characteristics of response integration evoked by multiple whisker stimulations in the barrel cortex of rats. *The Journal of neuroscience : the official journal of the Society for Neuroscience*, 19(22):10164–75.

Shoykhet, M. (2005). Whisker Trimming Begun at Birth or on Postnatal Day 12 Affects Excitatory and Inhibitory Receptive Fields of Layer IV Barrel Neurons. *Journal of Neurophysiology*, 94(6):3987–3995.

Shoykhet, M., Doherty, D., and Simons, D. J. (2000). Coding of deflection velocity and amplitude by whisker primary afferent neurons: implications for higher level processing. *Somatosensory & motor research*, 17(2):171–80.

Simons, D. J. (1983). Multi-whisker stimulation and its effects on vibrissa units in rat SmI barrel cortex. *Brain research*, 276(1):178–82.

Skibinska, A., Glazewski, S., Fox, K., and Kossut, M. (2000). Age-dependent response of the mouse barrel cortex to sensory deprivation: a 2-deoxyglucose study. *Experimental brain research*, 132(1):134–8.

Sofroniew, N. J., Vlasov, Y. A., Andrew Hires, S., Freeman, J., and Svoboda, K. (2015). Neural coding in barrel cortex during whisker-guided locomotion. *eLife*, 4:1–36.

Stern, E. A., Maravall, M., and Svoboda, K. (2001). Rapid Development and Plasticity of Layer 2/3 Maps in Rat Barrel Cortex In Vivo. *Neuron*, 31(2):305–315.

Stosiek, C., Garaschuk, O., Holthoff, K., and Konnerth, A. (2003). In vivo two-photon calcium imaging of neuronal networks. *Proceedings of the National Academy of Sciences of the United States of America*, 100(12):7319–7324.

Stüttgen, M. C., Kullmann, S., and Schwarz, C. (2008). Responses of rat trigeminal ganglion neurons to longitudinal whisker stimulation. *Journal of Neurophysiology*, 100(4):1879–1884.

Stüttgen, M. C. and Schwarz, C. (2008). Psychophysical and neurometric detection performance under stimulus uncertainty. *Nature neuroscience*, 11(9):1091–1099.

Svoboda, K., Denk, W., Kleinfeld, D., and Tank, D. W. (1997). In vivo dendritic calcium dynamics in neocortical pyramidal neurons.

Svoboda, K. and Yasuda, R. (2006). Principles of two-photon excitation microscopy and its applications to neuroscience. *Neuron*, 50(6):823–839.

Tamamaki, N., Yanagawa, Y., Tomioka, R., Miyazaki, J.-I., Obata, K., and Kaneko, T. (2003). Green fluorescent protein expression and colocalization with calretinin, parvalbumin, and

somatostatin in the GAD67-GFP knock-in mouse. *The Journal of Comparative Neurology*, 467(1):60–79.

Temereanca, S. and Simons, D. J. (2003). Local field potentials and the encoding of whisker deflections by population firing synchrony in thalamic barreloids. *Journal of neurophysiology*, 89(4):2137–2145.

Thévenaz, P., Ruttimann, U. E., and Unser, M. (1998). A pyramid approach to subpixel registration based on intensity. *IEEE transactions on image processing : a publication of the IEEE Signal Processing Society*, 7(1):27–41.

Thomas, D., Tovey, S. C., Collins, T. J., Bootman, M. D., Berridge, M. J., and Lipp, P. (2000). A comparison of fluorescent Ca2+ indicator properties and their use in measuring elementary and global Ca2+ signals. *Cell calcium*, 28(4):213–23.

Tsien, R. Y. (1980). New calcium indicators and buffers with high selectivity against magnesium and protons: design, synthesis, and properties of prototype structures. *Biochemistry*, 19(11):2396–404.

van der Bourg, A., Yang, J.-W., Reyes-Puerta, V., Laurenczy, B., Wieckhorst, M., Stüttgen, M. C., Luhmann, H. J., and Helmchen, F. (2016). Layer-Specific Refinement of Sensory Coding in Developing Mouse Barrel Cortex. *Cerebral Cortex*.

Van Der Loos, H. (1976). Barreloids in mouse somatosensory thalamus. *Neuroscience Letters*, 2(1):1–6.

Van der Loos, H. and Woolsey, T. a. (1973). Somatosensory cortex: structural alterations following early injury to sense organs. *Science (New York, N.Y.)*, 179(2):395–398.

Waite, P. M. E., Ho, S. M., and Henderson, T. A. (2000). Afferent ingrowth and onset of activity in the rat trigeminal nucleus. *European Journal of Neuroscience*, 12(8):2781–2792.

Welker, W. (1964). Analysis of Sniffing of the Albino Rat. *Behaviour*, 22(3):223–244.

Wen, J. A. and Barth, A. L. (2011). Input-specific critical periods for experience-dependent plasticity in layer 2/3 pyramidal neurons. *Journal of Neuroscience*, 31(12):4456–4465.

Wilent, W. B. and Contreras, D. (2004). Synaptic responses to whisker deflections in rat barrel cortex as a function of cortical layer and stimulus intensity. *J Neurosci*, 24(16):3985–3998.

Wilson, M. A. and McNaughton, B. L. (1993). Dynamics of the hippocampal ensemble code for space. *Science*, 261(5124):1055–1058.

Wilson, T. and Sheppard, C. (1984). *Theory and practice of scanning optical microscopy*. Academic Press INC.

Wise, K. D., Angell, J. B., and Starr, A. (1970). An Integrated-Circuit Approach to Extracellular Microelectrodes. *IEEE Transactions on Biomedical Engineering*, BME-17(3):238–247.

Yang, J.-W., Hanganu-Opatz, I. L., Sun, J.-J., and Luhmann, H. J. (2009). Three Patterns of Oscillatory Activity Differentially Synchronize Developing Neocortical Networks In Vivo. *Journal of Neuroscience*, 29(28):9011–9025.

Yu, X., Chung, S., Chen, D.-Y., Wang, S., Dodd, S., Walters, J., Isaac, J., and Koretsky, A. (2012). Thalamocortical Inputs Show Post-Critical-Period Plasticity. *Neuron*, 74(4):731–742.

Zhang, Z., Jiao, Y. Y., and Sun, Q. Q. (2011). Developmental maturation of excitation and inhibition balance in principal neurons across four layers of somatosensory cortex. *Neuroscience*, 174:10–25.

Acknowledgments

First and foremost I want to express my sincere gratitude to **Professor Fritjof Helmchen** for giving me the opportunity to pursue the path of science in such an outstanding laboratory and scientific envirnoment. Throughout the years Professor Helmchen showed incredible determination in helping me advance in my projects and always had an open mind for new ideas and solutions to difficult problems.

I also want to especially thank **Professor Heiko Luhmann** who allowed me to conduct a very fruitful collaboration project in his laboratory in Mainz which led to many important findings presented in this thesis. Additionally, I also want to thank **Professor Maik Stüttgen** who was an essential part in designing and conceptualizing the electrophysiology experiments presented in Chapters 2 and 3.

My great gratitude also goes to my fellow collaborators **Dr. Jenq-Wei Yang** and **Dr. Vicente Reyes-Puerta**. Dr. Yang is an extremely talented neurophysiologist and was essential in conducting electrophysiology experiments presented in the thesis. Dr. Reyes-Puerta also contributed greatly to the isolation of single units and general electrophysiology data analysis presented in chapter 2.

The essential core project of my thesis - the galvanometer-driven whisker stimulator - would not have been possible without the outstanding technical support by **Marco Tedaldi**, **Martin Wieckhorst** and **Stefan Giger**. Martin Wieckhorst in particular showed unchallenged enthusiasm while designing and building the stimulation system. Marco Tedaldi was also a great support concerning the software implementation of the stimulation system.

I also want to thank **Fabian Voigt** who introduced me into the more technical and theoretical aspects of two-photon calcium imaging. His instructive way of explaining complex physical phenomena in simple words is very inspirational.

Also many thanks go to the many **members of the Helmchen lab** who made the scientific endeavor of my PhD fun and exciting. I want to especially mention **Balazs Laurenzcy** with whom I had wonderful discussions about science and beyond. Our weekly Ping-Pong sessions were true highlights filled with joy, sweat and laughter.

Lastly, I want to thank my **parents** for their love and support. They always reminded me that there is more to life than significant statistics.

Alexander Berthold van der Bourg

Date of Birth	15.12.1985	
Contact Information	Friedackerstrasse 35 8050 Zürich	*Cell:* +41 795983286 *E-mail:* vanderbourg@gmail.com
Research Interests	Neural networks, microcircuits, network models, population coding, neural plasticity, neural basis of somatosensation	

Education

2012-2016: University of Zürich, Brain Research Institute, Switzerland: PhD in Neuroscience

2010-2012: ETH Zürich, Switzerland: Master of Science ETH, Neuroscience

2007-2010: ETH Zürich: Bachelor of Science ETH, Biology

2006-2007: ETH Zürich: Basic studies in Physics

2004-2006: Swiss Military, Officer's School and military pilot selection program participant

---

Research and Professional Experience

2012-2016: University of Zürich, Brain Research Institute, Zürich, Switzerland, PhD in Neuroscience

2012-2014: Course assistant for medical students

2013: EMBO course assistant

2011-2012: Janelia Farm Research Campus, Virginia USA, Visiting Scientist (supervised by Dr. Albert Cardona)

2010-2011: Visiting scientist and student in the lab of Albert Cardona

---

Other training & Professions

2015-present: Paragliding license

2013-present: Freelance moderator and video producer on YouTube

2007-2012: Securitas Security Officer in Zürich

2010-present: Swiss Military: Commanding officer of NBC defense units

---

Publications

Theses

1. Master Thesis: From Morphology to Behavior: Neural Basis of Nociceptive Somatosensation in *Drosophila* Larvae, ETH Zürich and Janelia Farm Research Campus. Supervisor: Prof. Kevan Martin, Dr. Albert Cardona, Dr. Daniel Kiper

Articles

1. **Alexander van der Bourg**, Jenq-Wei Yang, Vicente Reyes-Puerta, Balazs Laurenczy, Martin Wieckhorst, Maik C. Stüttgen, Heiko L. Luhmann and Fritjof Helmchen, 2016, *Layer-specific refinement of sensory coding in developing mouse barrel cortex* - **Cerebral Cortex, in press**

2. **Alexander van der Bourg**, Jenq-Wei Yang, Vicente Reyes-Puerta, Maik C. Stüttgen, Fritjof Helmchen and Heiko L. Luhmann, *Spatiotemporal processing of sensory-evoked activity in developing mouse barrel cortex* - **in preparation**

3. Linda Madisen, Aleena R. Garner, Daisuke Shimaoka, Amy S. Chuong, Nathan C. Klapoetke, Lu Li, **Alexander van der Bourg**, Yusuke Niino, Ladan Egolf, Claudio Monetti, Hong Gu, Maya Mills, Adrian Cheng, Bosiljka Tasic, Thuc Nghi Nguyen, Susan M. Sunkin, Andrea Benucci, Andras Nagy, Atsushi Miyawaki, Fritjof Helmchen, Ruth M. Empson, Thamas Knopfel, Edward S. Boyden, R. Clay Reid, Matteo Carandini and Hongkui Zeng, 2015, *Transgenic Mice for Intersectional Targeting of Neural Sensors and Effectors with High Specificity and Performance* - **Neuron**

4. Anna Guzik-Kornacka, **Alexander van der Bourg**, Flora Vajda, Sandrine Joly, Franziska Christ, Martin E. Schwab and Vincent Pernet, 2014, *Nogo-A deletion increases the plasticity of the optokinetic response and changes retinal projection organization in the adult mouse visual system* - **Brain Structure and Function**

Conference abstracts and proceedings

1. **Scientifica 2015**, public outreach, *"Dem Gehirn beim denken zuschauen "*
2. **SSN Meeting**, Fribourg, 2015
   Alexander van der Bourg & Fritjof Helmchen, 2015, *" Postnatal development of sensory-evoked activity in developing mouse barrel cortex "*
3. **45th SFN Annual Meeting**, Washington D.C., 2014
   Alexander van der Bourg & Fritjof Helmchen, 2015, *" Postnatal development of sensory-evoked activity in developing mouse barrel cortex "*

Talks

1. **Barrels Meeting**, Amsterdam 2016, *" Processing of sensory-evoked activity in developing mouse barrel cortex "*
2. **Barrels Meeting**, Baltimore, 2014
   " Postnatal development of sensory-evoked activity in developing mouse barrel cortex "
3. **Barrels Meeting**, Göttingen., 2014
   Alexander van der Bourg & Fritjof Helmchen, 2014, *" Postnatal development of sensory-evoked activity in developing mouse barrel cortex "*
